Durham E-Theses

Compact High-Data-Rate Implantable Antennas for Leadless Cardiac Pacemakers

ABDULWAHAB ALGHAMDI

How to cite:

ALGHAMDI, ABDULWAHAB (2025) Compact High-Data-Rate Implantable Antennas for Leadless Cardiac Pacemakers. Doctoral thesis, Durham University.

Use policy

The full-text may be used and/or reproduced, and given to third parties in any format or medium, without prior permission or charge, for personal research or study, educational, or not-for-profit purposes provided that:

- a full bibliographic reference is made to the original source
- a https://etheses.durham.ac.uk/id/eprint/16142/ is made to the metadata record in Durham E-Theses
- the full-text is not changed in any way

The full-text must not be sold in any format or medium without the formal permission of the copyright holders.

Please consult the full Durham E-Theses policy for further details.

Academic Support Office, The Palatine Centre, Durham University, Stockton Road, Durham, DH1 3LE
e-mail: e-theses.admin@durham.ac.uk Tel: +44 0191 334 6107
https://etheses.durham.ac.uk

Compact High-Data-Rate Implantable Antennas for Leadless Cardiac Pacemakers

By

Abdulwahab Hezam Alghamdi

A Thesis presented for the degree of
Doctor of Philosophy

Department of Engineering
Durham University
United Kingdom
May 2025

Abstract

In recent years, biomedical telemetry has revolutionised healthcare by enabling real-time remote monitoring of physiological parameters, reducing the need for frequent hospital visits and in-person check-ups. At the heart of this advancement are Implantable Medical Devices (IMDs), which facilitate wireless monitoring for a range of critical applications, including endoscopy, blood pressure tracking, cardiac defibrillators, pacemakers, and blood glucose monitoring. Among these innovations, leadless pacemakers have gained significant attention due to their minimally invasive design and improved patient comfort. However, their effectiveness depends largely on a well-optimised implantable antenna, which is essential for ensuring reliable wireless communication.

This thesis focuses on addressing key challenges including miniaturisation, resonant frequency detuning, and multipath fading within the human body's lossy electromagnetic environment.

Three novel implantable antenna designs are presented in this work. **The first contribution** presents an implantable antenna with a rectangular patch design, incorporating a U-shaped slot, an inductive shorting pin, and multiple edge slots. It achieves a volume of 9.44 mm^3, offering a 3.39 GHz bandwidth and a fractional bandwidth of 138%. The antenna supports a broad frequency range from 0.76

to 4.15 GHz, covering key medical bands, including the Industrial, Scientific, and Medical (ISM) bands at 0.869, 0.915, and 2.45 GHz; the Wireless Medical Telemetry Service (WMTS) band at 1.4 GHz; and the midfield communication band around 1.6 GHz. Simulation results within a homogeneous phantom (HP) of heart tissue indicate gain values of -32.4 dBi at 0.915 GHz, -27.94 dBi at 1.4 GHz, and -19.8 dBi at 2.45 GHz. **The second contribution** presents an ultra-compact implantable antenna featuring a central C-shaped slot. It has a volume of 8.33 $\text{mm}^{\mathbf{3}}$, a fractional bandwidth of 152.7%, and operates within a frequency range of 0.67 to 5 GHz, covering essential medical bands. These include the ISM bands at 0.915 GHz and 2.45 GHz, the WMTS band at 1.4 GHz, and the midfield band at 1.6 GHz. Simulation results indicate gain values of -31.3 dBi at 0.915 GHz, -25.8 dBi at 1.4 GHz, and -21.9 dBi at 2.45 GHz. **The third contribution** introduces a 2×1 ultra-wideband multiple-input, multiple-output (UWB-MIMO) antenna designed with two loop radiators and a shared slotted ground plane. The antenna achieves a compact volume of 16.4 $\text{mm}^{\mathbf{3}}$, a wide fractional bandwidth of 165.12%, and operates from 710 MHz to 7438 MHz with a high isolation level of -21 dB. The individual MIMO antenna elements exhibit peak gain values of -34.7 dBi at 0.915 GHz, -28.4 dBi at 1.4 GHz, -23.3 dBi at 2.45 GHz, and -20.1 dBi at 5.8 GHz. Furthermore, at a signal-to-noise ratio (SNR) of 20 dB, the antenna achieves a channel capacity of 15.04 bps/Hz, highlighting its suitability for high-data-rate telemetry in next-generation leadless pacemakers. Specific Absorption Rate (SAR) analysis confirms that all three implantable antennas comply with regulatory safety standards, ensuring patient safety.

List of Publications

1. A. Alghamdi, A. Alshammari, L. Chang, A. Iqbal, and I. B. Mabrouk, "Miniaturized Implantable Antenna with Ultra-Wide Bandwidth Characteristics for Leadless Pacemakers," in Proc. 2024 18th European Conf. Antennas Propagation (EuCAP), 2024, pp. 1–5.

2. A. Alghamdi, A. Basir, A. Iqbal, R. B. V. B. Simorangkir, and I. ben Mabrouk, "Compact Implantable Antenna with Ultra-Wide Bandwidth for Leadless Pacemaker," in Proc. 2024 IEEE Int. Symp. Antennas Propagation and INC/USNC-URSI Radio Sci. Meeting (AP-S/INC-USNC-URSI), 2024, pp. 369–370.

3. A. Alghamdi, A. Basir, A. Iqbal, R. B. V. B. Simorangkir, M. Al-Hasan and I. B. Mabrouk, "Compact Antenna With Broadband Wireless Biotelemetry for Future Leadless Pacemakers," in IEEE Transactions on Antennas and Propagation, doi: 10.1109/TAP.2024.3503919.

4. A. Alghamdi, A. Basir, A. Iqbal, R. B. V. B. Simorangkir, and I. B. Mabrouk, “A low-profile implantable antenna for heart implants,” IEEE Transactions on Antennas and Propagation, 2025.

Declaration

The research presented in this thesis was conducted at the Department of Engineering, Durham University, United Kingdom. The results discussed in Chapters 3, 4, and 5 have been published by the author in conferences and journals over the past two years. However, this thesis as a whole has not been submitted elsewhere for any other degree or qualification. All work is my own unless explicitly referenced otherwise in the text.

Copyright © 2025 By

Abdulwahab Hezam Alghamdi.

"The copyright of this thesis rests with the author. No quotations from it should be published without the author's prior written consent, and information derived from it should be acknowledged."

Acknowledgements

First and foremost, I would like to express my deepest gratitude to Almighty God for granting me the strength, perseverance, and wisdom to successfully complete my doctoral studies and this thesis.

I am profoundly grateful to my primary supervisor, Dr. Ismail Ben Mabrouk, for his invaluable guidance, advice, and support throughout my PhD journey. His expertise and encouragement have played a pivotal role in shaping my research and academic growth. I would also like to express my sincere appreciation to my second supervisor, Dr. Aissa Iklaf, for his generous assistance and mentorship. Their dedication and commitment to excellence have been a constant source of motivation and inspiration for me.

I am also deeply thankful to my family, whose love and encouragement have been my greatest source of strength. Additionally, I would like to express my appreciation to my friends and colleagues in the engineering department for their valuable discussions and continuous support.

Finally, I extend my gratitude to Durham University for providing an excellent research environment and resources that made this work possible.

To everyone who has contributed to my academic and personal growth in any way—thank you!

List of Symbols

- **3D** - Three Dimensions
- $\boldsymbol{\sigma}$ - Conductivity
- $\boldsymbol{\rho}$ - Mass density
- $\boldsymbol{\mu}$ (prefix) - Micro (SI prefix)
- $\boldsymbol{\mu}$**W** - Microwatt
- $\boldsymbol{\Omega}$ - Ohm
- $\boldsymbol{\lambda}$, $\boldsymbol{\lambda}_0$ - Wavelength
- $\boldsymbol{\epsilon}$ - Permittivity
- $\boldsymbol{\Gamma}$ - Reflection coefficient
- **ANSI** - American National Standards Institute
- $\boldsymbol{c}$ - Speed of light
- **CVDs** - Cardiovascular diseases
- **dB** - Decibels

- **ERC** - European Radiocommunications Committee
- $\boldsymbol{e_p}$ - Polarization mismatch factor
- **EM** - Electromagnetic
- **FCC** - Federal Communications Commission
- $\boldsymbol{g}$ - Gram
- **GHz** - Gigahertz
- **IMDs** - Implantable Medical Devices
- **ISM band** - Industrial, Scientific, and Medical band
- **ITU-R** - International Telecommunication Union Radiocommunication Recommendations
- **kg** - Kilogram
- $\boldsymbol{m}$ - Metre
- **MHz** - Megahertz
- **MedRadio** - Medical Radio Communication Band for medical telemetry applications
- **MICS** - Medical Implant Communication Service
- **PCB** - Printed Circuit Board
- $\boldsymbol{P_f}$ - Free-space path loss
- **PIFA** - Planar Inverted-F Antenna
- **RF** - Radio Frequency
- **SAR** - Specific Absorption Rate

- **SNR** - Signal-to-Noise Ratio
- **VNA** - Vector Network Analyzer
- **TX** - Transmitter
- **RX** - Receiver
- **MIMO** - Multiple-Input Multiple-Output
- **ICNIRP** - International Commission on Non-Ionizing Radiation Protection
- **FDTD** - Finite Difference Time Domain
- **HFSS** - High Frequency Structure Simulator
- **FEM** - Finite Element Method
- $\boldsymbol{P_t}$ - Transmitted power
- $\boldsymbol{f}$ - Frequency
- $\boldsymbol{G_t}$ - Transmit antenna gain
- $\boldsymbol{L_f}$ - Path loss
- $\boldsymbol{G_r}$ - Receiver antenna gain
- $\boldsymbol{N_o}$ - Noise power density
- $\boldsymbol{T}$ - Temperature
- $\boldsymbol{K}$ - Boltzmann constant
- $\boldsymbol{B_r}$ - Bit rate
- $\boldsymbol{E_b/N_o}$ - Energy per bit to noise power spectral density ratio
- $\boldsymbol{G_c}$ - Coding gain

- $\boldsymbol{G_d}$ - Gain degradation
- **FBM** - Full Body Model
- **HP** - Homogeneous Phantom
- **LCPs** - Leadless Cardiac Pacemakers
- **FBW** - Fractional Bandwidth
- **TPs** - Traditional Pacemakers
- $\mathbf{tan}\,\boldsymbol{\delta}$ - Loss tangent
- **MAP** - Maximum Allowable Power
- **LM** - Link Margin

Contents

List of Figures

List of Tables

Dedication

I would like to dedicate this thesis to the memory of my parents, whose guidance and values inspire me. I also dedicate this work to my beloved wife, Sarah, whose unwavering support and encouragement have been my pillar of strength, and to my dear children, Fares, Bushra, Omar, and Talal, who are my constant source of joy and motivation. In addition, I would like to dedicate this work to my nephew Mohammed, who supported me.

CHAPTER 1

Introduction

1.1 Research Background

In recent years, there has been a growing interest in the development of implantable biomedical devices, particularly for cancer treatment and health monitoring [16,17]. In the case of health monitoring devices, they track vital health indicators such as temperature, blood pressure, heart rate, and oxygen saturation, transmitting these data from inside the body to external monitoring systems. They enable both short- and long-range communication, allowing real-time health tracking and proactive medical interventions. Additionally, their bidirectional communication capabilities allow doctors to provide personalised, timely treatments by remotely adjusting therapeutic parameters [18].

One of the most widely used long-term implantable medical devices is the cardiac pacemaker, designed to regulate abnormal heart rhythms, particularly in patients with bradycardia (slow heart rate) [19]. Traditional pacemakers typically consist mainly of a pulse generator, battery, leads, and electrodes that deliver electrical signals to stimulate the heart and restore its normal rhythm [20]. However, the use of leads can lead to complications such as infections or a change in their intended position [21].

To overcome the challenges of traditional pacemakers, leadless cardiac pacemakers (LCPs) represent a breakthrough in cardiac pace technology [22]. Unlike traditional pacemakers, LCPs eliminate the need for leads by integrating all essential components into a compact unit that is approximately 90% smaller than standard pacemakers—comparable in size to a AAA battery [23, 24]. These devices are implanted directly into the right ventricle using a minimally invasive catheter-based procedure through the femoral vein [25], as shown in Figure 1.1. This technique eliminates the need for a surgical chest incision or a subcutaneous pocket, reducing risks such as infection, haematoma, and lead-related complications, while improving patient comfort and cosmetic outcomes [26]. The simplified implantation process, enhanced safety, and long-term reliability make LCPs a transformative advancement in cardiac care [27].

Despite their advantages, LCPs face challenges related to wireless communication, as they rely on implantable antennas for real-time data transmission. A built-in antenna enables LCPs to wirelessly transmit and receive information, allowing doctors to remotely monitor patient conditions and adjust therapy as needed [28]. However, implanting an antenna within the human body, a lossy and dispersive medium, poses significant challenges. Biological tissues absorb and scatter electromagnetic waves, reducing the efficiency, signal strength, and overall performance of the antenna compared to free-space operation [29]. These challenges necessitate the design of optimised implantable antennas that maximise signal penetration, minimise power loss, and ensure reliable communication within the constraints of the human body.

Furthermore, implantable antennas must comply with strict safety regulations, particularly those related to Specific Absorption Rate (SAR), which limits the amount of electromagnetic energy absorbed by biological tissues [30]. Regulatory bodies enforce stringent SAR thresholds to ensure patient safety, necessitating careful design considerations for antenna efficiency and power output.

In addition, implantable medical devices must operate within designated frequency bands to prevent interference with nearby devices and ensure stable commu-

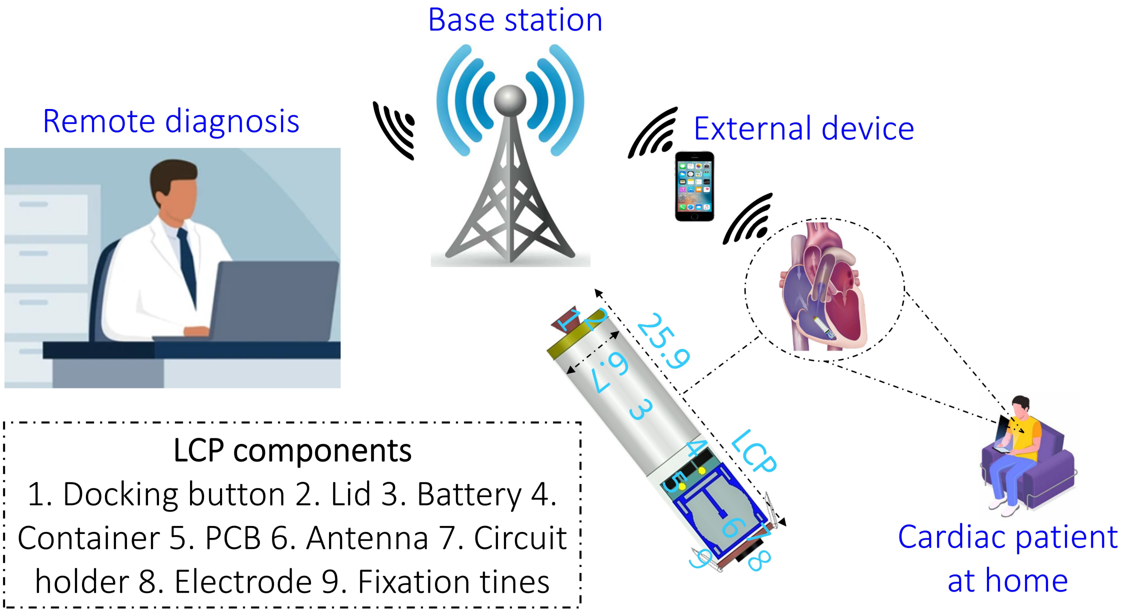

Figure 1.1: The structure and components of the leadless cardiac pacemaker (LCP).

nication. The International Telecommunication Union (ITU) has allocated specific frequency bands for medical applications, including the Medical Implant Communication Service (MICS) band (402–405 MHz), the Industrial, Scientific, and Medical (ISM) bands (433 MHz, 868–868.6 MHz, 902–928 MHz, 2.4–2.48 GHz, and 5.725–5.875 GHz), the Wireless Medical Telemetry Service (WMTS) bands (608–614 MHz, 1395–1400 MHz, and 1427–1432 MHz), and the midfield communication bands (1450–1600 MHz and 1824–1980 MHz). These frequency allocations are carefully selected to balance signal penetration depth and data transmission efficiency, making them suitable for implantable applications. However, higher frequencies, such as those in the 2.4 GHz ISM band, are more susceptible to interference from common wireless technologies like Bluetooth and Wi-Fi, which operate within the same spectrum. Fortunately, implantable medical devices typically function at very low power levels, around 25 μW, significantly reducing the risk of interference and ensuring reliable operation within the human body [31].

1.2 Research Motivation

By 2030, the global population is projected to reach 8.5 billion, with one in six individuals aged 60 or older—an increase in the elderly population from 1 billion in 2020 to 1.4 billion. With bradycardia affecting approximately one in every 600 people over the age of 65, the growing ageing population is driving demand for advanced cardiac solutions such as leadless pacemakers (LCPs). These innovative devices offer enhanced patient comfort and improved long-term health outcomes, making them a crucial advancement in cardiac care.

One key motivation for developing advanced implantable antennas for LCPs is the need for robust real-time remote monitoring capabilities. Recent advancements in wireless communication technologies have enabled continuous monitoring of vital patient data without physical intervention. Reliable wireless connectivity facilitates immediate detection of abnormalities, allowing prompt medical response and significantly improving patient outcomes and safety.

Another key motivation is compactness. More compact antennas help reduce the overall size of pacemakers, simplify surgical implantation, minimise patient discomfort, and enhance device stability. However, designing compact antennas without compromising performance presents significant challenges. As the antenna size decreases, maintaining resonance stability and impedance matching becomes increasingly difficult due to higher dielectric losses and altered electromagnetic properties within the human body. Overcoming these obstacles is crucial to achieving efficient miniaturised designs.

A third key motivation is energy efficiency through wireless charging and energy harvesting. Traditional battery-powered LCPs require periodic replacements, necessitating invasive surgical procedures that pose risks to patients and increase healthcare costs. Integrating wireless charging and energy harvesting technologies into antenna designs has the potential to revolutionise implantable devices by significantly extending battery life or even eliminating the need for replacements. By harvesting ambient energy, these advancements could eliminate frequent battery replacements, reduce surgical interventions, enhance patient comfort, and improve the sustainability of long-term cardiac care.

1.3 Problem Statement

Leadless cardiac pacemakers (LCPs) have revolutionised cardiac care by providing minimally invasive, continuous cardiac rhythm sensing and life-saving pacing therapy for patients with bradyarrhythmias. However, the miniaturisation and optimisation of implantable antennas for LCPs remain a formidable engineering challenge due to stringent size constraints, strict RF exposure regulations, and the complex electromagnetic environment within the human body.

A critical challenge in implantable antenna design is achieving extreme miniaturisation while maintaining optimal performance, including stable resonance, impedance matching, radiation efficiency, and reliable wireless communication. The highly lossy nature of biological tissues causes significant signal attenuation, leading to deviations between simulated and real-world antenna performance, complicating design validation and optimisation.

While miniaturisation is essential, it introduces a fundamental trade-off between antenna size and operating frequency. Higher frequencies experience severe propagation losses in biological tissues, while lower frequencies require larger antennas, conflicting with stringent size constraints. Efforts to reduce antenna size at lower frequencies often lead to undesired resonance shifts, further complicating performance optimisation.

Despite extensive research, existing solutions struggle to balance miniaturisation, efficiency, and robustness in dynamic biological environments. Current designs often suffer from:

1.3.1 Space Constraints

The extreme miniaturisation required for LCP antennas compromises key performance metrics, including radiation efficiency and signal strength.

1.3.2 Detuning (Resonant Frequency Shift)

Detuning in implantable antennas occurs when resonance frequency shifts, compromising efficiency and disrupting wireless communication. In biomedical applications, this is critical as physiological changes and patient movements alter the antenna's electromagnetic environment, leading to unstable signals. These fluctuations pose significant challenges for real-time monitoring and data transmission in leadless cardiac pacemakers.

1.3.3 Multipath Fading

Reflections of transmitted signals within biological tissues lead to multipath propagation, causing signal fading due to interference between paths and resulting in degraded signal reliability.

To overcome these challenges, this thesis proposes novel implantable antenna designs that directly tackle space constraints, detuning, and multipath fading, ensuring superior wireless performance in LCPs. By leveraging advanced materials, innovative resonance tuning techniques, and optimised antenna geometries, these solutions aim to enhance device reliability, improve patient outcomes, and establish new performance standards in biomedical telemetry.

1.4 Objectives

The primary objective of this thesis is to design and develop efficient, compact, and high-performance implantable antenna systems for leadless cardiac pacemakers (LCPs) while addressing the critical challenges outlined in the Problem Statement. Specifically, this research aims to:

1.4.1 Miniaturisation

Design and optimise ultra-compact implantable antennas that seamlessly integrate into LCPs without compromising performance. Miniaturisation is crucial for reducing device size, enhancing patient comfort, and simplifying surgical implantation. Achieving this objective requires innovative miniaturisation techniques to ensure efficient space utilisation while maintaining key performance metrics, including impedance matching, resonance stability, and radiation efficiency.

1.4.2 Ultra-Wideband Operation

Develop implantable antennas with enhanced bandwidth characteristics to support stable and reliable wireless communication under varying physiological conditions. Wideband designs are essential for mitigating detuning effects, maintaining consistent resonance, and ensuring robust data transmission despite tissue property variations.

1.4.3 MIMO Architecture

Investigate and implement ultra-wideband (UWB) multiple-input multiple-output (MIMO) antenna architectures to mitigate multipath fading and enhance communication reliability in dynamic biological environments.

1.5 Novelty and Contribution

This thesis introduces three innovative implantable antenna designs for leadless cardiac pacemakers (LCPs), each specifically engineered to address critical wireless communication challenges, including miniaturisation, detuning, and multipath fading. The key contributions of this research are summarized as follows:

- **First Contribution:** A wideband implantable antenna employing a rectangular patch with a U-shaped slot, inductive shorting pin, and edge slots. Expanded slots in the ground plane enhance bandwidth. The antenna achieves a compact volume of **9.44 mm^{3}** and a bandwidth of **3.39 GHz**, effectively addressing detuning issues.
- **Second Contribution:** An ultra-compact implantable antenna with ultra-wideband (UWB) characteristics, featuring a rectangular patch with a central C-shaped slot and corner via. Optimized ground plane slots and asymmetric circular structures further enhance performance. This antenna achieves a minimal volume of **8.33 mm^{3}** and an ultra-wide bandwidth of **4.33 GHz**, simultaneously addressing miniaturisation and detuning concerns.

- **Third Contribution:** A UWB-MIMO antenna design comprising two rectangular loop radiators, open-ended and multi-U-shaped slots, and an inductive shorting pin. With a total volume of $\mathbf{16.4\ mm^3}$ and a fractional bandwidth of **6.72 GHz**, this antenna significantly reduces multipath fading, improves data transmission reliability, and supports high-data-rate telemetry in implantable cardiac applications.

Collectively, these novel designs represent substantial advancements toward efficient, compact, and reliable implantable antennas, enhancing the performance and clinical effectiveness of next-generation leadless cardiac pacemakers.

1.6 Thesis Structure

This thesis is structured into six chapters as follows:

1.6.1 Chapter 1: Introduction

This chapter introduces the research by presenting the problem statement, highlighting critical challenges associated with implantable antenna design for leadless cardiac pacemakers (LCPs). It identifies the research gaps in existing literature, formulates the research questions, and clearly outlines the motivation, objectives, novelty, and significant contributions of this study.

1.6.2 Chapter 2: Background and Literature Review

This chapter provides a comprehensive review of implantable antenna technology, covering its historical development and fundamental principles. It discusses critical design considerations such as miniaturisation, biocompatibility, bandwidth, patient safety, and wireless communication reliability. Existing solutions and their limitations are analyzed to establish the foundation for the novel designs proposed in this research.

1.6.3 Chapter 3: Compact Antenna With Broadband Wireless Biotelemetry for Future Leadless Pacemakers

This chapter presents a novel design that employs various techniques to mitigate detuning effects in implantable antennas. Detailed simulations and analyses are conducted to validate the effectiveness of these techniques in ensuring stable performance within the human body.

1.6.4 Chapter 4: A Low-Profile Implantable Antenna for Heart Implants

This chapter addresses two major challenges: antenna miniaturisation and detuning effects. It introduces novel antenna designs that achieve significant size reduction while maintaining optimal resonance, impedance matching, and radiation performance. Detailed simulations and analyses validate their effectiveness in overcoming size constraints and mitigating detuning within the human body.

1.6.5 Chapter 5: A Compact Ultra-Wideband MIMO Antenna for Next-Generation Leadless Pacemakers

This chapter addresses the third major challenge—multipath fading—by proposing an ultra-wideband multiple-input multiple-output (UWB-MIMO) antenna. The design is analyzed thoroughly, showing how it improves signal diversity, reduces multipath interference, and enhances data rates and spectral efficiency. Performance metrics such as isolation, SAR values, channel capacity, and correlation coefficient are evaluated to confirm the effectiveness of the proposed design.

1.6.6 Chapter 6: Conclusion and Future Work

This final chapter summarizes the key conclusions, highlighting the significant contributions and outcomes of the research. It provides a concise overview of the main findings and their implications for implantable medical antenna technology. The chapter concludes by suggesting directions for future research to encourage ongoing advancements in the field.

Overall, this thesis structure ensures a clear progression from identifying existing limitations to presenting innovative antenna designs that effectively overcome critical challenges in implantable cardiac healthcare applications.

CHAPTER 2

Background and Literature Review

2.1 Introduction

The performance of implantable antennas is heavily influenced by the heterogeneous nature of human tissue, which contrasts sharply with free space. Unlike free space, where electromagnetic waves propagate with minimal loss, human tissues exhibit high dielectric permittivity and conductivity, leading to increased signal attenuation, scattering, and power loss [32, 33]. Deeper implants experience greater attenuation as signals pass through multiple tissue layers, each causing absorption and reflection.

Designing antennas for biomedical implants presents several challenges. One key concern is ensuring patient safety by complying with Specific Absorption Rate (SAR) limits, which regulate the maximum energy absorption permitted in human tissue [34]. Antenna design must carefully balance power efficiency while mitigating interference with other devices operating in adjacent frequency bands [35].

Furthermore, the heterogeneous dielectric properties of human tissues introduce significant variability in energy absorption and signal propagation, complicating antenna optimisation. Addressing these challenges requires accurate electromagnetic modelling of tissue properties and simulations that account for anatomical variability, enabling more precise performance predictions under real-world conditions [36].

2.2 Definition of Key Terms

In the context of this thesis, several key terms are defined as follows:

Ultra-Wideband (UWB): According to the Federal Communications Commission (FCC), a system is classified as ultra-wideband if it occupies either a fractional bandwidth greater than 20% or an absolute bandwidth of at least 500 MHz [37]. In implantable applications, UWB offers high temporal resolution, low power operation, and resistance to multipath fading, making it ideal for short-range biomedical telemetry.

Compact Antenna: A compact antenna is one whose largest dimension is significantly smaller than the wavelength at its operating frequency—typically less than $\lambda/10$. Compactness is especially critical for implantable devices, where space is severely limited [38].

High Data Rate: In this thesis, a high data rate refers to wireless transmission speeds exceeding 1 Mbps. Such rates are necessary to support applications like high-resolution physiological monitoring or wireless endoscopic imaging. UWB systems can theoretically support data rates in the range of several Mbps to hundreds of Mbps, depending on modulation and system configuration [39].

2.3 Requirements and Standards

There are several requirements and standards that implantable antenna designs must comply with to ensure optimal performance within the human body. Unlike free-space antennas, implantable antennas must account for the lossy nature of human tissues, which significantly affects their operation. Although the design requirements can vary depending on the application, there are common factors that apply to most implantable antenna designs. These key points are discussed in this section.

2.4 Requirements and Standards

There are several requirements and standards that implantable antenna designs must comply with to ensure optimal performance within the human body. Unlike free-space antennas, implantable antennas must account for the lossy nature of human tissues, which significantly affects their operation. Although the design requirements can vary depending on the application, there are common factors that apply to most implantable antenna designs. These key points are discussed in this section.

2.4.1 Patient Safety Requirements

Human body safety is the most important factor when designing implantable antennas for medical devices. Therefore, careful consideration must be taken to prevent any potential damage to body tissues from exposure to electromagnetic radiation. Electromagnetic fields can cause harmful effects, such as tissue heating and nerve stimulation. To mitigate these risks, strict standards and regulations limit the amount of electromagnetic energy that can be safely absorbed by the body. These guidelines ensure that implantable devices operate within safe power levels and frequencies. The design process must also consider the type of tissue, the placement of the device, and its proximity to vital organs, as these factors influence how electromagnetic fields interact with the body. By addressing these issues, manufacturers can ensure that implantable medical devices are safe and effective.

2.4.1.1 Specific Absorption Rate (SAR)

The SAR measures the amount of radiofrequency (RF) energy absorbed per unit mass of tissue when exposed to electromagnetic fields (EMF). It is expressed in units of power per kilogram (W/kg) and can be calculated at a specific location within the tissue or averaged over the mass of tissue or the entire human body. SAR serves as a critical parameter to ensure the safety of biological tissues during electromagnetic exposure. Two internationally recognised standards establish the permissible SAR levels:

- According to the IEEE C95.1-1999 standard, the SAR must be less than 1.6

W/kg, averaged over a 1 g cubic volume of tissue [40].

- The IEEE C95.1-2005 standard specifies that the SAR should not exceed 2 W/kg, averaged over a 10 g cubic volume of tissue [41].

The Federal Communications Commission (FCC) [42] uses a 1 g averaging method, while the International Commission on Non-Ionizing Radiation Protection (ICNIRP) recommends a 10 g averaging method [43]. In order to meet standard SAR limits, implantable devices must operate at low transmit power levels. The basic formula for calculating the SAR is as follows:

$$SAR = \frac{\sigma E^2}{\rho} \tag{2.1}$$

Where:

- SAR = Specific Absorption Rate (W/kg)
- σ = Conductivity of the tissue (S/m)
- E = Electric field strength (V/m)
- ρ = Density of the tissue (kg/m^3)

This formula calculates the SAR based on tissue conductivity, electric field strength, and tissue density. The temperature increase in tissue resulting from RF energy absorption can be estimated using the following formula:

$$\Delta T = \frac{SA}{m \cdot C} \tag{2.2}$$

Where:

- ΔT = Temperature increase (°C)
- SA = Specific Absorption (Joules)
- m = Mass of the tissue (kg)
- C = Specific heat capacity of the tissue (J/kg·°C)

This equation estimates the temperature increase in tissue based on the absorbed energy, the mass of the tissue, and the tissue's specific heat capacity. It is crucial to ensure that the temperature of the human tissue surrounding the implanted device does not increase by more than 1°C, as this could potentially lead to adverse effects on the tissue [44].

2.4.1.2 Effective Isotropic Radiated Power (EIRP)

EIRP represents the total power radiated by an antenna in a specific direction, assuming the antenna is an ideal isotropic radiator, as shown in the formula below:

$$EIRP = P_{tx} + G_{tx} - L_{tx} \tag{2.3}$$

where:

- P_{tx} = Transmitted power (dBm or watts)
- G_{tx} = Antenna gain (dBi)
- L_{tx} = Losses in the transmission path (dB)

The EIRP of an implantable antenna is a critical parameter to ensure the safety of both the human body and nearby electronic devices. Excessive EIRP levels can pose risks to surrounding biological tissues and may interfere with other radio frequency devices in proximity. To address these concerns, standardised EIRP limits have been established for implantable antennas that operate within specific frequency bands.

For medical implant communication, MedRadio band regulations allow up to $25\,\mu W$ $(-16\,dBm)$, optimizing signal reliability. However, ISM bands impose stricter power limits $0.01\,\mu W$ or $(-20\,dBm)$ to minimize interference in shared frequency environments. Adhering to these power limits minimises the potential for harmful electromagnetic exposure and ensures that the device functions safely and effectively.

2.4.2 Biocompatibility

Biocompatibility is a vital aspect in the design of implantable antennas, which ensures their safe and effective operation within the human body. It refers to the

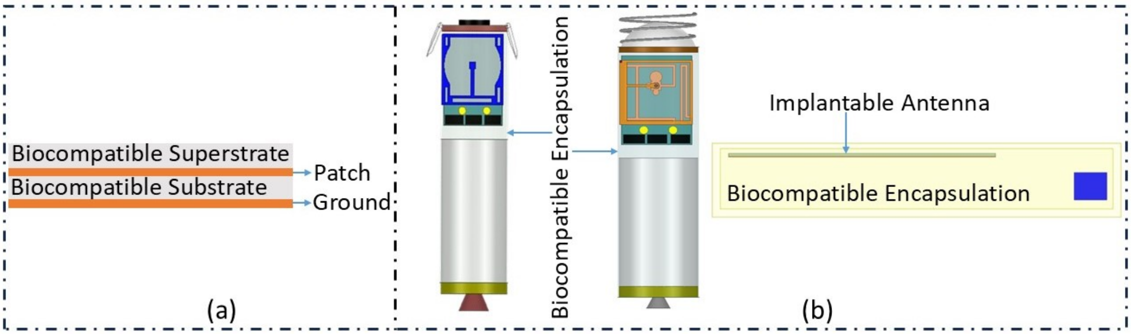

Figure 2.1: Approaches to achieve antenna biocompatibility: (a) Using a biocompatible substrate/superstrate, (b) Encapsulating with biocompatible materials.

ability of materials or devices to function as intended without provoking adverse biological responses, such as inflammation, tissue damage, or immune rejection [45]. Ensuring biocompatibility minimizes the risk of harmful interactions, such as electrical short circuits with body tissues, while preserving the device's reliability and performance.

2.4.2.1 Biocompatible Methods

Typically, two primary methods are employed to achieve biocompatibility:

- **Biocompatible Substrate/Superstrate:** The antenna can be fabricated using inherently biocompatible materials for both the substrate and the superstrate [46], as illustrated in Figure 2.1(a).

- **Biocompatible Encapsulation:** The implantable antenna is enclosed within a biocompatible housing, often referred to as a biocompatible layer. This layer ensures compatibility with biological tissues by serving as a protective barrier, preventing adverse reactions such as inflammation or immune rejection, while allowing the safe integration of the device within the body [46], as illustrated in Figure 2.1(b).

2.4.2.2 Biocompatible Materials

Materials used for encapsulation and substrate construction are selected based on their electromagnetic properties, biocompatibility, and ease of fabrication. These materials must ensure both safe integration within biological environments and efficient antenna operation. These include:

- **Zirconia:** This material has high permittivity ($\epsilon_r = 29$) and extremely low energy loss ($\tan\delta \approx 0$), making it ideal for bioencapsulation. Its properties help focus electromagnetic fields and reduce power loss [47].

- **Silastic MDX-4210 Elastomer:** With a permittivity of $\epsilon_r = 3.3$ and negligible loss ($\tan\delta \approx 0$), this material is widely used for safe and flexible biomedical applications [48].

- **Titanium (Ti):** Known for excellent biocompatibility, corrosion resistance, and strength, titanium ($\epsilon_r \approx 8.5$, $\tan\delta \approx 0.001$) is used for implants and encapsulation [49].

- **Gold (Au):** Gold ($\epsilon_r \approx 11.7$, $\tan\delta \approx 0.01$) is biocompatible and resistant to corrosion, often used in antennas for its stability and reliability in biological environments [50].

- **Ceramic Materials:** Alumina ($\epsilon_r = 9.4$, $\tan\delta = 0.006$) and zirconia ($\epsilon_r = 29$, $\tan\delta \approx 0$) offer high permittivity and low losses, making them excellent choices for substrates and encapsulation [51].

- **Teflon (PTFE):** Chemically inert and biocompatible, Teflon ($\epsilon_r = 2.1$, $\tan\delta = 0.001$) provides excellent insulation and low energy loss, commonly used in antenna substrates [52].

- **PEEK:** This thermoplastic ($\epsilon_r = 3.2$, $\tan\delta = 0.01$) is strong, stable, and biocompatible, ideal for encapsulating antennas and other medical devices [53].

- **Polyurethane:** Flexible and biocompatible, polyurethane ($\epsilon_r \approx 2.5$, $\tan\delta \approx 0.01$) is used for soft encapsulation and as a substrate in implantable antennas [54].

By employing biocompatible materials and encapsulation techniques, implantable antennas can achieve reliable performance while minimizing the risks to human health.

2.5 Design Techniques for Implantable Antennas

Designing implantable antennas for biomedical applications demands strict adherence to size, efficiency, and functionality requirements. This is achieved by combining techniques such as miniaturisation to reduce size, and bandwidth expansion to ensure reliable performance. These methods work together to create antennas that meet the challenges of their demanding environments. The following sections discuss these key techniques in detail.

2.5.1 Miniaturisation Techniques

The implantable antenna is a crucial component of an implantable device, and its miniaturisation presents a significant design challenge. Since implantable devices are typically compact, reducing the antenna's size is essential for seamless integration without compromising performance. These antennas operate within specific frequency ranges, such as the MICS, MedRadio, and ISM bands, and achieving miniaturisation requires careful design strategies.

Reducing the antenna's size directly impacts its bandwidth and efficiency [55, 56]. Smaller antennas generally exhibit a higher radiation quality factor (Q factor), which limits the achievable bandwidth. This trade-off necessitates a careful balance between size reduction and performance optimisation.

Recent studies have focused on minimising the antenna's size by modifying its electrical and physical properties while ensuring good impedance matching and bandwidth retention. The following sections discuss some of the widely used techniques for antenna miniaturisation.

2.5.1.1 Frequency Selection Considerations

While not a miniaturisation technique in itself, frequency selection is a fundamental design parameter that strongly influences antenna size. Due to the inverse relationship between wavelength and frequency, operating at higher frequencies allows antennas to occupy a smaller physical volume. As frequency increases, the effective guided wavelength shortens, thereby enabling more compact structures. This design approach is commonly leveraged in miniaturised biomedical systems.

However, operating at higher frequencies introduces significant trade-offs—most notably, increased propagation losses in biological tissues. These losses can reduce radiation efficiency, limit penetration depth, and elevate the specific absorption rate (SAR), especially in deep-tissue implant scenarios [57]. Therefore, frequency selection must be carefully balanced against performance requirements, particularly in lossy environments.

Implantable antennas typically operate in regulated medical frequency bands, including the Medical Implant Communication Service (MICS), MedRadio, and Industrial, Scientific, and Medical (ISM) bands. Among these, the MICS band is often preferred due to its favourable balance between tissue penetration and acceptable antenna size [58]. While the ISM band allows for greater miniaturisation due to its higher frequency, it is generally less suitable for deep implants due to severe tissue absorption and signal degradation [59].

Advantages:

- Enables physically smaller antenna structures due to shorter wavelength.
- Simplifies integration into miniaturised or capsule-based biomedical devices.

Drawbacks:

- Leads to increased propagation losses in biological tissues.
- Reduces radiation efficiency and depth of signal penetration.
- May require stricter compliance with SAR and regulatory limits.

2.5.1.2 Shorting Pin

The shorting pin is a widely adopted miniaturisation technique, particularly effective in compact and implantable antenna designs. It involves placing a conductive via—commonly made of copper—that connects the radiating element directly to the ground plane through the dielectric substrate. This structural modification transforms the antenna from a half-wavelength ($\lambda/2$) to a quarter-wavelength ($\lambda/4$) resonator, effectively reducing the physical length required to achieve resonance [60].

In addition to reducing size, the shorting pin introduces an inductive effect that alters the antenna's equivalent circuit characteristics. This inductance can aid in achieving better impedance matching, making the technique especially beneficial in designs such as the Planar Inverted-F Antenna (PIFA). When carefully optimized, the shorting pin contributes to both size reduction and stable resonance. However, improper placement or design may lead to reduced radiation efficiency and performance degradation.

Advantages:

- Allows substantial reduction in antenna height or length.
- Enhances impedance matching via inductive loading.

Drawbacks:

- Potential reduction in radiation efficiency if not optimally implemented.
- Adds fabrication complexity, particularly in multilayer or conformal structures.

2.5.1.3 Meander Line

The meander line technique is a widely used approach for antenna miniaturisation, especially in applications with strict space constraints. Originally introduced in [61], this method involves folding the radiating element into a compact, serpentine (meandered) pattern, thereby increasing the effective electrical length while reducing the antenna's overall physical dimensions.

By extending the current path without enlarging the footprint, the meander line design enables resonance at the desired frequency within a limited volume. This technique is particularly effective in wearable, implantable, and conformal antennas where size and profile are critical. However, due to the increased current path length and added bends, it can introduce additional losses and affect impedance characteristics.

Advantages:

- Enables compact antenna design by extending electrical length.

- Well-suited for low-profile and conformal biomedical applications.

Drawbacks:

- May introduce additional ohmic and radiation losses.
- Increased sensitivity to manufacturing tolerances and misalignments.
- Can complicate impedance matching and reduce overall gain.

2.5.1.4 Engineering the Ground Plane

Engineering the ground plane is a powerful miniaturisation technique that enables a physically small antenna to appear electrically larger. This is typically achieved by manipulating the wave propagation characteristics within the antenna structure to reduce the effective wavelength. The ground plane—the conductive layer beneath the radiating element—plays a pivotal role in determining radiation pattern, impedance characteristics, and bandwidth performance [62].

A commonly used method involves introducing Defected Ground Structures (DGS), such as notches, slots, or patterned etchings, into the ground plane. These alterations modify the return current path and create additional inductive and capacitive effects, effectively slowing down electromagnetic wave propagation. As a result, the antenna can resonate at a lower frequency without increasing its physical size. This technique is particularly valuable in compact implantable designs, where space is limited, but performance must be preserved.

Advantages:

- Enhances impedance matching and bandwidth without increasing footprint.
- Enables electrically larger behavior from physically compact structures.

Drawbacks:

- May increase back-lobe radiation, which is undesirable in implantable contexts.
- Introduces fabrication complexity and sensitivity to etching precision.
- Requires extensive simulation and optimization to ensure consistent performance.

2.5.1.5 High Permittivity Dielectric Substrates

Employing substrates with high relative permittivity (ε_r) is a widely adopted strategy for antenna miniaturisation, particularly in microstrip and implantable designs. A higher dielectric constant reduces the wavelength of electromagnetic waves within the substrate, which in turn decreases the physical size required for the antenna to achieve resonance at a given frequency. This enables the design of compact antennas suitable for integration into space-constrained biomedical devices [63–65].

However, this miniaturisation advantage comes with trade-offs. High-permittivity substrates tend to support stronger surface wave propagation and exhibit greater dielectric losses, both of which can degrade radiation efficiency and overall antenna performance [66]. Additionally, such substrates often lead to narrower bandwidths and pose challenges for impedance matching due to the reduced effective aperture and increased reactive loading [67].

Despite these limitations, high-ε_r materials are especially useful in biomedical contexts, where matching the electrical properties of surrounding tissues is important. For example, Rogers 3210 ($\varepsilon_r = 10.2$) is frequently employed in implantable antenna designs for this purpose [38].

Advantages:

- Enables significant antenna size reduction.
- Enhances compatibility with high-permittivity biological tissues.

Drawbacks:

- Increases dielectric and surface wave losses.
- Degrades radiation efficiency and limits bandwidth.
- Complicates impedance matching and design optimization.

2.5.1.6 Inductive/Capacitive Loading

Loading techniques are widely utilised in antenna design to achieve impedance matching at specific operating frequencies, which is essential to optimise performance and minimise antenna size. These methods involve integrating reactive elements, either inductive or capacitive, into the antenna structure. Impedance is a complex quantity consisting of real (resistive) and imaginary (reactive) components. Effective matching of the antenna's impedance to the transmission line or connected circuitry is vital to maximise power transfer and reduce signal reflection. However, miniaturisation of the antenna often increases the reactive component of the impedance, making matching more challenging.

- Inductive loading is a useful technique for balancing impedance in small antennas, particularly when their natural resonance is higher than the desired operating frequency. This method involves adding inductive elements, such as shorting pins ((discussed previously), to the antenna design. For example, [68] demonstrates how inductive loading helps reduce the size of the antenna while maintaining functionality.

- Capacitive loading is a well-established technique in antenna design and electromagnetic theory. It involves adding capacitive elements or making structural modifications, such as incorporating slots, to introduce capacitance into the antenna. This method is particularly useful for antennas that exhibit excessive inductive behavior. Studies such as [69] demonstrate how capacitive loading enhances miniaturisation while achieving adequate impedance matching.

- Combined Use of Loading Techniques: In some cases, a combination of inductive and capacitive loading is employed to achieve a balance between size reduction and impedance matching. Research in [38] illustrates how these methods can be tailored to achieve optimal performance in compact antenna designs, particularly for biomedical applications where size constraints are stringent.

2.5.2 Bandwidth Enhancement Techniques

These methods are designed to improve the operational bandwidth of the antenna:

2.5.2.1 Lower Permittivity Substrate

Utilising substrates with low dielectric constants (ε_r) is an effective approach to enhance antenna bandwidth and radiation efficiency. A lower permittivity reduces electromagnetic energy confinement within the substrate, which in turn minimises surface wave propagation and dielectric losses. This enables more efficient radiation into the surrounding medium and contributes to a broader impedance bandwidth.

Such substrates also improve overall antenna performance by reducing energy storage in the material, allowing a faster wave velocity and wider frequency response. These characteristics are particularly beneficial in applications where wideband operation and high efficiency are required. For instance, [70] demonstrated the use of a substrate with $\varepsilon_r = 3$ to achieve ultra-wideband performance in a compact implantable antenna design.

However, the use of low-permittivity materials typically requires a physically larger structure to maintain resonance at the same frequency, which can be a limitation in space-constrained biomedical applications.

Advantages:

- Improves radiation efficiency by reducing dielectric and surface wave losses.
- Enhances impedance bandwidth and overall antenna performance.
- Facilitates better far-field radiation characteristics.

Drawbacks:

- Requires larger physical dimensions, which may conflict with miniaturisation goals.
- Less suitable for extremely compact or deep-implant scenarios.

2.5.2.2 Defected Ground Structures (DGS)

DGS are widely used to enhance antenna performance by modifying the ground plane geometry. These structures involve etching intentional defects—such as slots, notches, or other patterns—into the ground plane of a microstrip antenna. By altering the return current distribution, DGS introduces additional inductance (L) and modifies the capacitance (C) within the antenna's equivalent circuit, thereby impacting the resonant behavior [71, 72].

This modification can lead to improved impedance matching and bandwidth enhancement by expanding the effective frequency range over which the antenna operates efficiently. In addition, DGS can be employed to suppress surface waves, reduce mutual coupling in MIMO systems, or shape the radiation pattern, depending on the design.

However, the inclusion of DGS adds complexity to both the design and fabrication processes. The altered current paths may also introduce parasitic radiation or undesired coupling effects if not properly optimised.

Advantages:

- Enhances impedance matching and broadens operational bandwidth.
- Allows control over current distribution and radiation pattern.
- Can be used for mutual coupling reduction in multi-element systems.

Drawbacks:

- Requires precise electromagnetic simulation and optimization.
- May introduce unwanted radiation or cross-coupling if misconfigured.
- Adds complexity to fabrication, especially in multilayer or compact designs.

2.6 Tissue Effects

Implanting an antenna within biological tissue affects key parameters such as impedance, bandwidth, and radiation efficiency. Understanding these effects is essential for designing antennas that function reliably and communicate effectively within the human body.

2.6.1 Tissue Effects on Radio Propagation

The human body's frequency-dependent electrical properties, coupled with its complex and lossy environment, create significant challenges in the design of implantable antennas. This stands in contrast to free space, where electromagnetic waves encounter minimal resistance due to near-zero conductivity ($\sigma = 0$) and relative permittivity ($\varepsilon_r = 1$).

2.6.1.1 Frequency-Dependent Tissue Properties

The dielectric properties of biological tissues vary with frequency, complicating the performance and optimisation of implantable antennas [32]. Notable examples include:

- **403 MHz**: Used for MICS-band implants. Muscle and skin have conductivities of 0.79 S/m and 0.69 S/m, and relative permittivities of 57.1 and 46.7, respectively. Internal organs like the stomach, colon, and small intestine exhibit even higher conductivities (up to 1.9 S/m).
- **915 MHz**: Conductivity of muscle increases to 0.948 S/m, while permittivity slightly drops to 55.0, resulting in moderate attenuation.
- **2.45 GHz**: Widely used for medical telemetry. Conductivity of muscle rises to 1.74 S/m; permittivity decreases to 52.7, leading to stronger signal loss.
- **5.8 GHz**: High-speed data bands suffer the most attenuation, with muscle conductivity reaching 4.96 S/m and permittivity dropping to 48.5.

2.6.1.2 Attenuation Losses in Tissue

As frequency increases, signal attenuation becomes more pronounced due to higher conductivity and lower permittivity. The attenuation loss L in dB for a wave traveling through a tissue medium is expressed as [73]:

$$L = 20 \log \left(e^{-\alpha m} \right)$$

Where:

- m: Distance through tissue (m)
- α: Attenuation constant (Np/m), calculated as:

$$\alpha = \frac{1}{2}\sqrt{\frac{\omega\mu\sigma}{\epsilon}\left(\sqrt{1+\left(\frac{\sigma}{\omega\epsilon}\right)^2}-1\right)}$$

with:

- ω: Angular frequency (rad/s)
- μ: Tissue permeability (H/m), typically μ_0 for non-magnetic tissue
- $\epsilon = \epsilon_r\epsilon_0$: Absolute permittivity
- σ: Tissue conductivity (S/m)

2.6.1.3 Reflection Losses at Tissue Interfaces

Reflection losses occur at boundaries between tissues with differing electromagnetic properties. The reflection loss L_r (in dB) is determined by:

$$L_r = -20\log_{10}(|\Gamma|) \quad \text{where} \quad \Gamma = \frac{\eta_2 - \eta_1}{\eta_2 + \eta_1}$$

The intrinsic impedance η of a lossy tissue is calculated by:

$$\eta = \frac{j\omega\mu}{j\omega\epsilon + \sigma}$$

Where:

- η_1, η_2: Intrinsic impedances of adjacent tissues
- Γ: Voltage reflection coefficient at the interface

As frequency increases, the difference in impedance between tissues becomes more pronounced due to rising conductivity and falling permittivity, resulting in larger $|\Gamma|$ values and hence greater reflection losses.

2.6.1.4 Tissue Effects on Link Budget Performance

To ensure reliable communication—particularly in systems such as implantable medical devices—accurate calculation of the received power is essential due to signal degradation caused by tissue attenuation, reflection losses, and other propagation effects. The link budget equation (2.9) [74] provides a framework for estimating the received power by incorporating key parameters such as transmit power, antenna gains, path loss, polarization mismatch, impedance mismatch, and mismatch losses at both the transmitter and receiver. This calculation enables appropriate adjustment of the transmission power to ensure adequate signal strength at the receiver, thereby maintaining data integrity, energy efficiency, and compliance with biological safety standards.

$$P_{\mathrm{R}} = P_{\mathrm{T}} + G_{\mathrm{T}} + G_{\mathrm{R}} - L_P - P_e - ML_{\mathrm{T}} - ML_{\mathrm{R}} \tag{2.4}$$

Where, P_{R} represents the received power and P_{T} represents the transmitted power, both expressed in dBm. The gain of the transmitter antenna G_{T} is measured in dB and is typically negative for implantable antennas due to signal attenuation and reflection losses within the body. Similarly, the gain of the receiver antenna G_{R} is also expressed in dB. The polarization mismatch factor P_e is expressed in dB and accounts for any misalignment between the transmission and reception polarizations of the antennas. The impedance loss of the transmitter ML_{T} and the impedance loss of the receiver ML_{R} are measured in dB, reflecting power losses due to impedance mismatches between the transmitter and antenna, as well as between the receiver and antenna, respectively.

To assess the robustness of the communication link, the link margin (LM) is introduced, defined as the difference between the received power and the minimum receiver sensitivity $P_{\min}$:

$$LM = P_{\mathrm{R}} - P_{\min} \tag{2.5}$$

A positive link margin ensures that the received signal remains above the minimum required threshold, even in the presence of fading, interference, or slight misalignment between system components.

The path loss, L_P, in dB can be obtained using Equation (2.10) [75]:

$$L_P = 10n \log_{10}\left(\frac{d}{d_0}\right) + S + 10\log_{10}\left(\frac{4\pi d_0}{\lambda_0}\right)^2 \tag{2.6}$$

The path loss component n plays a crucial role in determining signal attenuation, and its value varies depending on the propagation environment. In line-of-sight (LOS) indoor conditions, the value of n is typically set to 1.5, as the signal experiences minimal obstruction and attenuation. In contrast, in indoor propagation without line-of-sight (NLOS), where obstacles such as walls and furniture hinder the signal, n is typically higher, usually set to 3, reflecting a more significant signal degradation. In free-space, n is conventionally set to 2. The reference distance d_0 is commonly assumed to be 1 meter, providing a standardized basis for calculations. Furthermore, the wavelength λ_0 is inversely proportional to the frequency, which means that higher frequencies correspond to shorter wavelengths. The parameter S accounts for random scattering, representing the variability of signal strength due to environmental factors such as reflections, diffraction, and interference. For free-space propagation, the equation simplifies to the following expression (2.11) [76]:

$$L_f = 20\log_{10}\left(\frac{20\pi d}{\lambda_0}\right) \tag{2.7}$$

Where the term L_f (dB) represents the free-space path loss.

Receiver Sensitivity. The minimum signal level that can be successfully detected by a receiver is defined as the receiver sensitivity $P_{\min}$. It is computed using:

$$P_{\min} = \left(\frac{E_b}{N_o}\right) + 10\log_{10}(B_r) - G_c + G_d \tag{2.8}$$

Where:

- $\frac{E_b}{N_o}$: Energy per bit to noise power spectral density ratio (dB), typically 9.6 dB for BPSK with a BER of 10^{-5}
- B_r: Bit rate in bits per second (bps)
- G_c: Coding gain (dB), depending on the error-correcting code used

- G_d: Implementation margin or degradation factor (dB), typically 2–3 dB

Noise Power Density. To evaluate thermal noise, the noise power spectral density N_o (in dBm/Hz) is calculated by:

$$N_o = 10 \log_{10}(kT) \tag{2.9}$$

Where $k = 1.38 \times 10^{-23}\,\mathrm{J/K}$ is Boltzmann's constant, and $T = 290\,\mathrm{K}$ is the standard room temperature. This gives a typical value of:

$$N_o \approx -174\,\mathrm{dBm/Hz}$$

This value serves as a baseline for computing receiver sensitivity and signal-to-noise ratio (SNR) in implantable communication systems.

In free space, the near field is reactive and does not significantly affect the radiated or absorbed power. However, in implantable antennas, the near-field strongly couples with surrounding materials, such as biological tissue, leading to increased power loss [17]. This interaction results in lower radiation efficiency because some energy is absorbed by the tissue rather than being radiated outward. This phenomenon is a significant challenge in the design of implantable antennas, as it reduces their overall efficiency and must be factored into both antenna design and link budget evaluations.

2.6.2 Tissue Effects on Antenna Bandwidth

Although implantable antennas are generally compact and tend to have narrow bandwidths, their interaction with surrounding tissues can lead to an increase in the effective bandwidth. This is because the dielectric properties of the tissues influence the antenna's resonance, altering its impedance and radiation efficiency. A significant portion of the radiated power is absorbed by the tissues, leading to increased losses, while only a small fraction is reflected back to the source [17]. Chapter 3 of this thesis focuses on the design of implantable antennas with broader bandwidths, employing various techniques to mitigate detuning caused by changes in tissue properties, aging, and implantation site variability.

2.6.3 Tissue Effects on Antenna Radiation Pattern

The radiation pattern of an antenna represents the distribution of radiated energy as a function of angle at a fixed distance from the antenna [77]. This pattern is essential for understanding how the antenna radiates energy in space. In the case of implantable antennas, the radiation pattern behaves differently compared to conventional antennas in free space. This difference arises because the surrounding medium, such as human tissue, is lossy, meaning that a significant portion of the radiated power is absorbed by the tissue. This absorption causes the radiation pattern to broaden, in contrast to the narrower pattern typically observed in free space. Furthermore, the position of the implantable antenna within the body significantly influences its radiation pattern. Even when placed in the same tissue type, the antenna's position or mounting scenario can cause variations in the radiation characteristics. These variations result from the complex interactions between the antenna and the surrounding tissues, which can differ based on factors like tissue thickness and the antenna's exact placement within the body. As a result, accurate predictions of the antenna's performance in practical applications require a detailed understanding of the antenna's position within the body and the specific characteristics of the surrounding tissue.

2.7 Methodology for Designing Implantable Antennas

To simplify the design process and facilitate tracking easier, the authors in [78] created a clear Methodology for developing implantable antennas, as shown in Figure 2.2. This Methodology helps ensure a smooth and accurate development process, beginning with the identification of the target application. The Methodology consists of three main steps:

- **Step 1**

  The first step involves selecting an appropriate frequency band, such as MICS, ISM, or MedRadio, based on application needs like data rate, power efficiency, and regulatory compliance. Next, key design parameters, including radiation pattern, size, and specifications, are defined to ensure compatibility with the implantable device's environment. A homogeneous phantom is then created, with its type and size tailored to the application and implantation depth, providing a realistic test model. The antenna is inserted into the phantom, and simulations are conducted using software such as ANSYS HFSS (High Frequency Structure Simulator), which is based on the Finite Element Method (FEM), or CST Studio Suite (Computer Simulation Technology), which uses the Finite Difference Time Domain (FDTD) technique. If the simulated return loss (S_{11}) exceeds $-15\,\text{dB}$, the design proceeds to the next step. Otherwise, the design parameters must be manually adjusted and re-simulated to meet the desired performance criteria.

- **Step 2**

  Safety is a critical consideration for implantable antennas due to their proximity to the human body. Regulatory organizations, such as the International Commission on Non-Ionizing Radiation Protection (ICNIRP) and IEEE, have established Specific Absorption Rate (SAR) limits to prevent tissue heating caused by electromagnetic radiation. To ensure compliance with these SAR limits, the Effective Isotropic Radiated Power (EIRP) of Implantable Wireless Medical Devices (IWMDs) must be carefully controlled to minimize radiation exposure and avoid interference with nearby radio systems. For example, antennas operating in the ISM and MedRadio bands must adhere to EIRP standards of $-20\,\text{dB}$ and $-16\,\text{dB}$, respectively.

  In this step, the implantable antenna is integrated into a heterogeneous phantom, representing a human body model. Two key metrics are evaluated: first, the return loss (S_{11}) must be below $-15\,\text{dB}$, and second, the SAR values must remain below the specified safety thresholds. If these conditions are met, the design progresses to the final step. Otherwise, the design parameters must be adjusted, and the antenna resimulated to meet performance and safety standards.

- **Step 3**

  Once optimised through simulations in both homogeneous and heterogeneous human models, the antenna is ready for fabrication and measurements. The fabrication of small vias is achieved through precision micro-drilling techniques, utilising laser technology. This method, known as Plated Through Hole (PTH), involves drilling holes through the entire PCB to connect the top and bottom copper layers. A key advantage of PTH is its enhanced reliability and durability, ensuring stable electrical connections. Copper plating inside the vias forms a strong, conductive link between layers, reducing the risk of open circuits or intermittent failures. Ensuring accurate hole tolerance is essential for proper component placement. Typically, the hole diameter should be 0.16 mm larger than the lead diameter to accommodate tolerances, drill wear, drill misalignment, and variations in plating.

  Before measuring the S-parameter S_{11} of an antenna using a vector network analyzer (VNA), calibration is essential to ensure accurate results and eliminate errors such as cable losses and impedance mismatches. This process typically involves using a calibration kit with known standards (open, short, and load) or, in more advanced setups, a thru-reflect-line (TRL) method. Calibration compensates for imperfections in the measurement setup, ensuring that only the antenna's intrinsic performance is evaluated. Once the calibration is complete, a 50-ohm coaxial cable is used to connect the antenna to the VNA, which then measures the S-parameter S_{11} to assess the antenna's impedance matching. The next phase involves assessing the antenna's gain within a SATIMO chamber.

  In this thesis, in vitro testing was used, referring to experiments conducted outside a living organism using models that simulate biological conditions. These tests commonly involve materials like saline solution or minced pork. Since direct implantation into the human body poses risks, antennas are first tested in these body-like phantoms to ensure safety and effectiveness before clinical use. Saline solution and minced pork offer distinct advantages for testing. Saline solution is homogeneous and easy to prepare, making it a con-

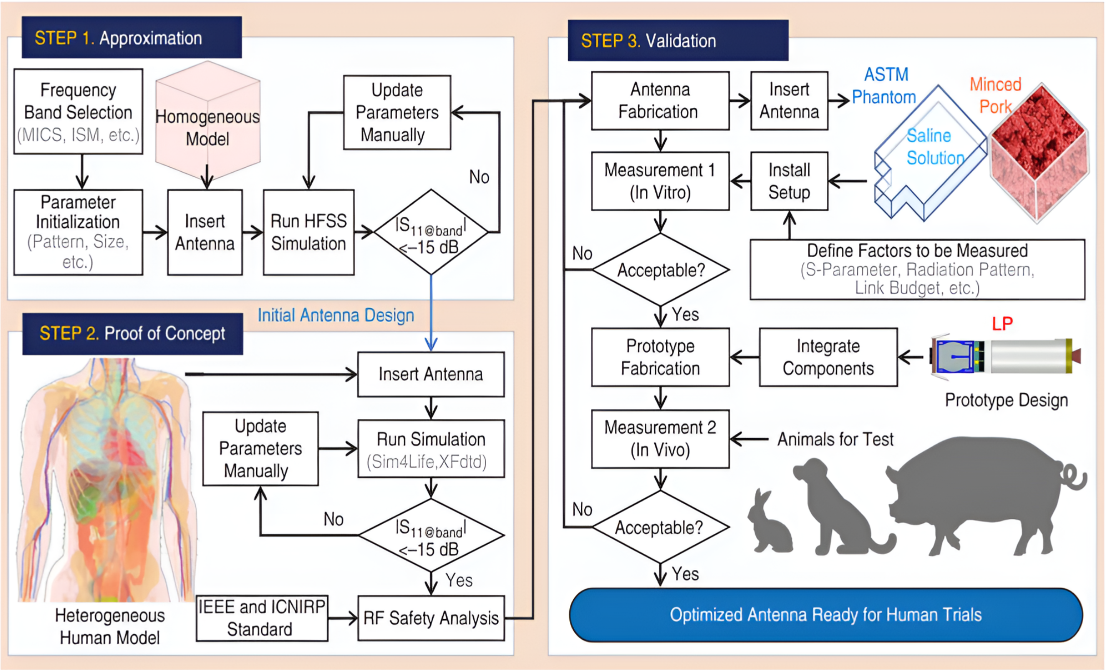

Figure 2.2: A structured protocol for designing and implementing implantable antennas.

venient choice. In contrast, minced pork is heterogeneous, with an asymmetric tissue distribution, providing a more realistic approximation of human body conditions.

2.8 Literature Review on Antenna Designs

Many studies have focused on different shapes, designs, and types of implantable antennas to overcome the challenges of operating within the human body. These designs aim to improve size, impedance matching, radiation efficiency, and bandwidth for reliable operation in complex biological environments. This review highlights recent developments in implantable antennas, focusing on various designs, materials, and techniques that enhance their performance and adaptability to medical applications. The primary categories of existing implantable antennas are as follows.

2.8.1 Planar Antenna

Planar antennas are flat or nearly flat structures fabricated on planar substrates, making them a popular choice for various applications due to their compact design and ease of integration into devices. Their low-profile construction is particularly advantageous for implantable systems as it allows seamless placement against tissue surfaces or within medical devices. Planar antennas can be further classified into rigid and flexible designs as follows:

2.8.1.1 Rigid Planar Design

These antennas maintain a rigid, flat structure and are commonly used when the implantation site offers a flat or slightly curved surface. Although they are less adaptable to irregular geometries found within the human body, rigid planar antennas provide high structural stability and are easier to fabricate with precise dimensional control. Numerous designs in this category have been developed to achieve a wide bandwidth while maintaining a compact size [1–10]. In [1], a coupled loop antenna was developed to achieve a wide bandwidth of 74.1% when embedded in muscle tissue, addressing the detuning issues common in such environments, as shown in Figure 2.3. The design incorporates inner and outer loops with printed capacitive elements, which enhance its performance. The planar antenna measures $30 \times 16 \times 0.5$ mm (240 mm^3) and is constructed using Rogers RO4350B, a substrate with a thickness of 0.5 mm and a dielectric constant of 3.48. To minimize energy loss, a ceramic superstrate layer is added, which features a height of 0.5 mm, a high dielectric constant of 9.9, and a low loss tangent of 0.0001. This antenna design achieves a gain of -23.19 dBi, attributed to reduced power dissipation in surrounding tissues. The Specific Absorption Rate (SAR) is measured at 177 W/kg with 1 W input power, allowing a maximum safe transmission power of 9.03 mW, in compliance with IEEE safety standards.

The square antenna design presented in [2] is shown in Figure 2.4. By incorporating slots in the patch plane and employing a shorting technique, the overall antenna size, including the superstrate, was reduced to $9.8 \times 9.8 \times 1.27$ mm (121.97 mm^3), while maintaining efficient operation at 2.4 GHz. The use of a slotless ground

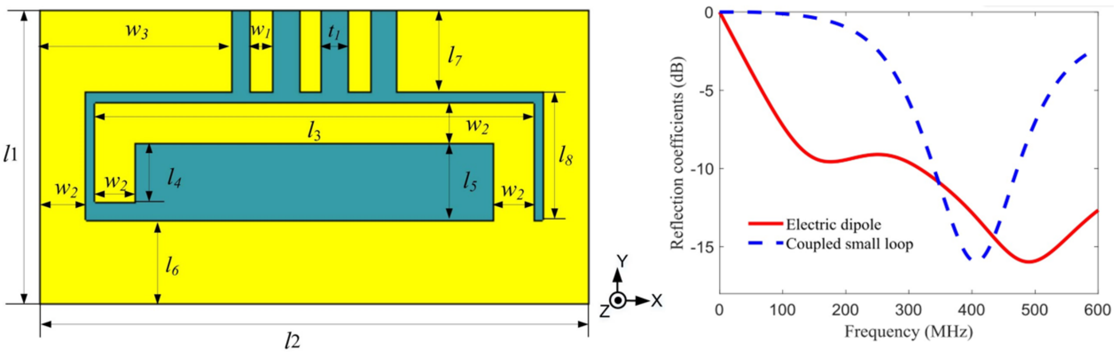

(a) (b)

Symbol	t_1	w_1	w_2	w_3	l_1	l_2	l_3	l_4	l_5	l_6	l_7	l_8
Value (mm)	0.5	0.5	2.2	13	16	30	24	3.2	4.2	4.5	4.5	7

Figure 2.3: (a) Top view of the coupled loop antenna; (b) Reflection coefficient of the coupled small loop [1].

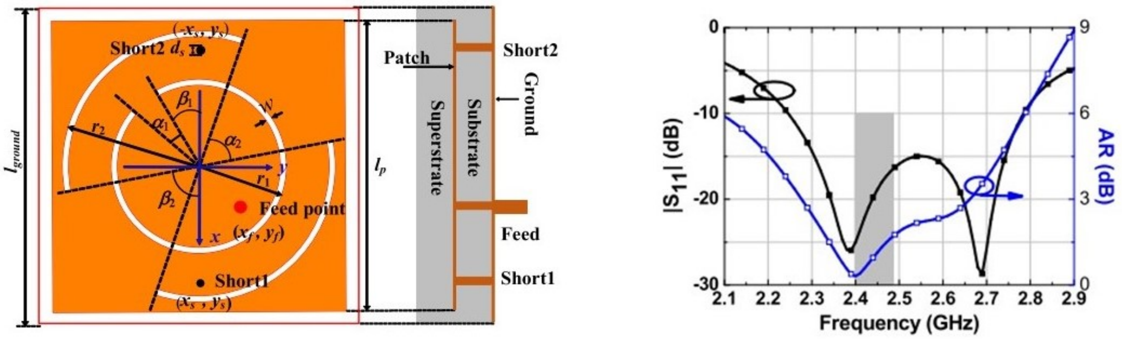

(a) (b)

Parameters	Value	Parameters	Value
α_1	20°	β_1	30°
α_2	60°	β_2	79°
w	0.2 mm	r_1	2.7 mm
r_2	4.2 mm	x_s	3.6 mm
y_s	0	x_f	1.3 mm
y_f	1.3 mm	l_p	9 mm
l_{ground}	9.8 mm	d_s	0.5 mm

Figure 2.4: (a) Antenna structure; (b) Antenna response: $|S_{11}|$ and AR [2].

contributed to improved impedance bandwidth and axial ratio (AR) bandwidth. Simulations revealed an impedance bandwidth of 21.5% (for a 10 dB return loss) and an AR bandwidth of 15.8% (within the 3 dB criterion). This antenna design achieves a gain of −33 dBi.

In [3], a capacitance-loaded wideband implantable antenna is presented. The design achieves a volume of 99.7 mm^3 and offers an impedance bandwidth of 20.5%,

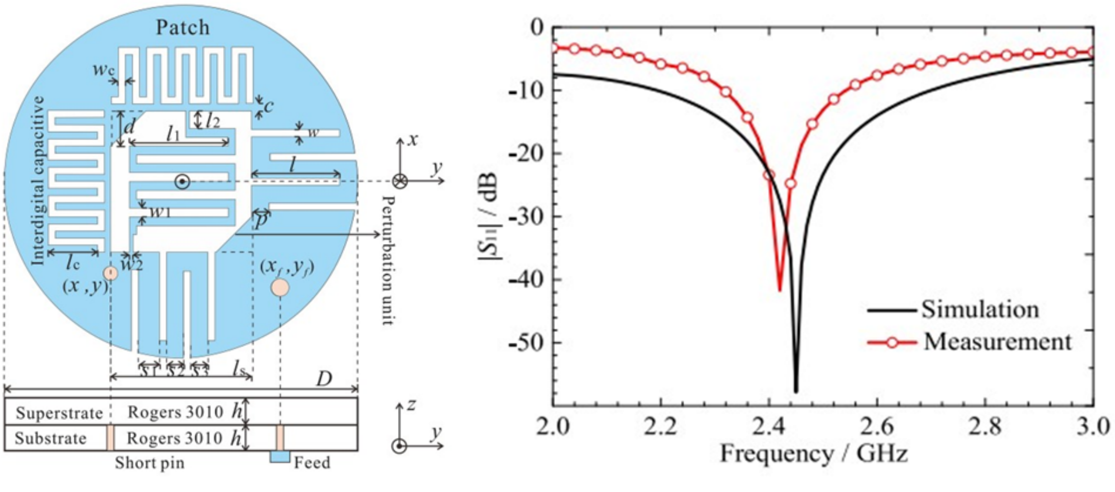

Symbol	D	h	l	lc	lg	ls	$l1$	$l2$	p
Value	10	0.635	2.5	1.4	6	4	2.8	0.5	0.5
Symbol	d	$s1$	w	wc	wg	$s2$	$w1$	$w2$	c
Value	1	0.7	0.2	0.2	4	0.5	0.25	0.1	0.2

Figure 2.5: (a) Geometry of the antenna; (b) Simulated and measured $|S_{11}|$ results [3].

ranging from 2.17 GHz to 2.69 GHz. As shown in Figure 2.5, the antenna's geometry features a circular patch radiator with a square patch removed from its center, where the side length denoted as l_s. Meander line elements are incorporated at the center of the radiator, and two groups of slots are placed along the right and bottom edges to minimize the antenna's overall size. The design uses a Rogers 3010 substrate with a dielectric constant (ε_r) of 10.2. The antenna achieves a gain of -26.4 dBi.

In [4], a wideband coplanar waveguide-fed antenna is introduced for body-implantable applications, as shown in Figure 2.6. The antenna has dimensions of $16 \times 16 \times 0.275$ mm (70.4 mm^3) and operates at a resonant frequency of 2.4 GHz. It achieves a broad fractional bandwidth of 88.6% (1.35–3.5 GHz) while maintaining a low-profile structure. The wideband performance is attributed to the use of an asymmetric complementary split-ring resonator, which enables multiple mode excitations. Further miniaturisation and enhanced impedance matching are accomplished through the integration of asymmetrical arc-shaped annular ring slots within the primary radiator. This antenna design achieves a high gain of -16.5 dBi.

In [5], an implantable antenna designed for the 2.4 GHz ISM band is presented. The antenna has a circular radiator with four L-shaped slots and a shortening pin,

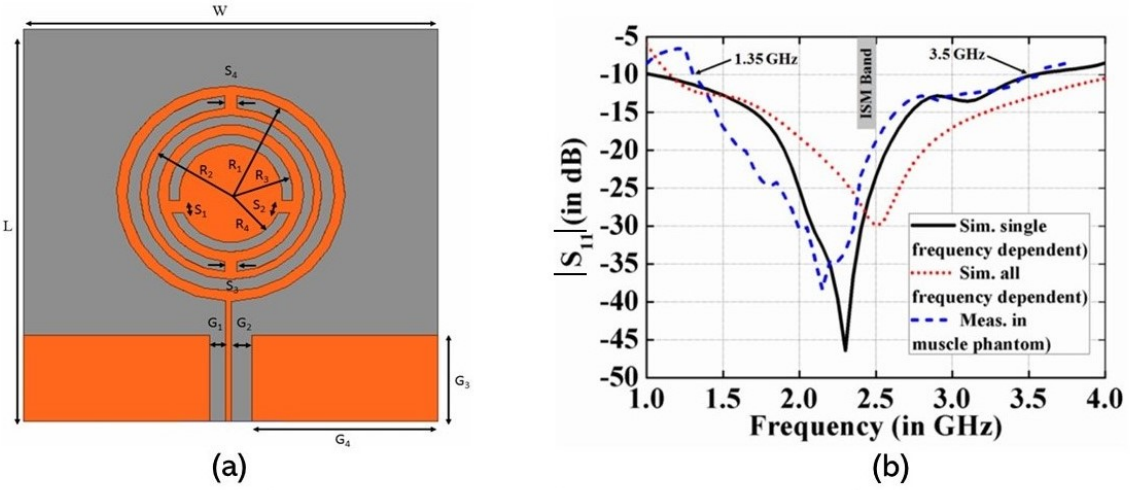

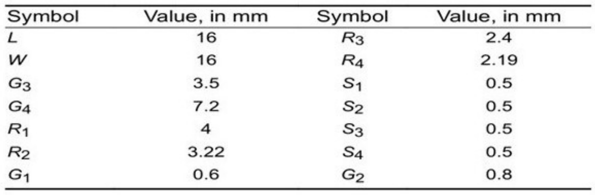

Symbol	Value, in mm	Symbol	Value, in mm
L	16	R_3	2.4
W	16	R_4	2.19
G_3	3.5	S_1	0.5
G_4	7.2	S_2	0.5
R_1	4	S_3	0.5
R_2	3.22	S_4	0.5
G_1	0.6	G_2	0.8

Figure 2.6: (a) Geometry structure of the antenna; (b) Simulation and measurement of the $|S_{11}|$ [4].

which allows for circular polarization, as shown in Figure 2.7. To enhance performance, rectangular cross-cut slots are etched into the ground plane, improving both the impedance and the axial ratio (AR) bandwidths. The test results demonstrate an impedance bandwidth of 2.25–2.78 GHz and an AR bandwidth of 2.32–2.63 GHz. The antenna occupies a total volume of 63.8 mm^3. Miniaturisation is achieved using Rogers 3010 material ($\varepsilon_r = 10.2$, $\tan\delta = 0.001$), applied as both substrate and superstrate, each with a thickness of 0.635 mm.

In [6], the design of a dual-band spiral antenna is presented, as illustrated in Figure 2.8. This antenna operates in the MICS band at 403 MHz and the ISM band 2.45 GHz, with a total volume of 59.5 mm^3. To validate its performance, measurements were conducted in a saline solution formulated to replicate the dielectric properties of human muscle tissue. The antenna achieves peak gains of −33 dBi at 403 MHz and −16 dBi at 2.45 GHz. Additionally, the fractional bandwidths are 18.4% for the 403 MHz band and 40.8% for the 2.45 GHz band. The design utilizes a Rogers RT/duroid 6010 substrate with a dielectric constant (ε_r) of 10.2 which reduces the physical size of the antenna by shortening the wavelength within the structure.

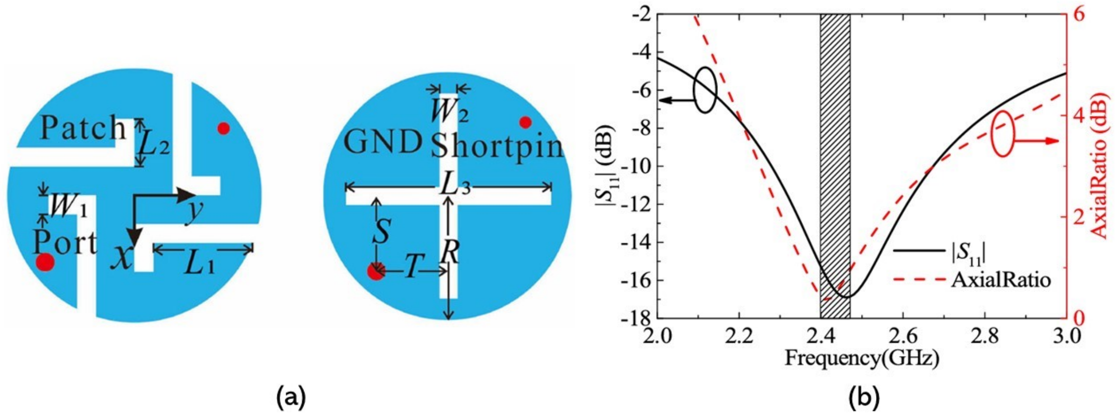

Demension	R	L_1	L_2	L_3	W_1	W_2	S	T
Size (mm)	4	3.2	1.2	6	0.6	0.42	2.8	2.1

Figure 2.7: (a) Geometry structure of the antenna; (b) Simulated results: $|S_{11}|$ and AR [5].

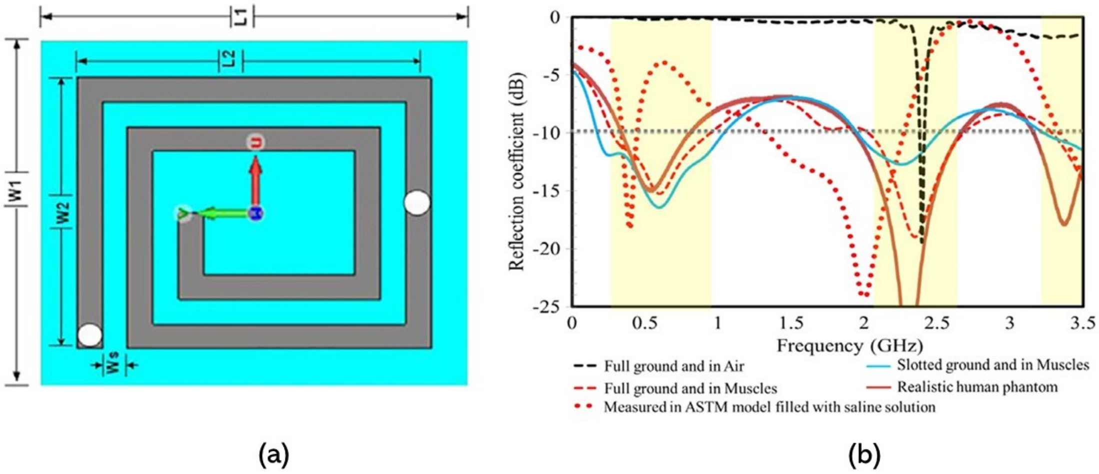

Parameters	Values (mm)	Parameters	Values (mm)
L_1	17	W_2	13
L_2	16	Ws	0.5
W_1	14	h	0.25

Figure 2.8: (a) Geometry structure of the antenna; (b) Simulation and measurement of the $|S_{11}|$ [6].

In [7], the antenna has a circular shape with a volume of 39.3 mm^3, as shown in Figure 2.9. Two rectangular slots were introduced into the patch to increase the electrical length of the antenna, which aids in miniaturisation by lowering the resonant frequency. The antenna geometry was optimized to resonate at 2.4 GHz. The design was fabricated using Taconic RF-35, a low-loss, biocompatible PCB

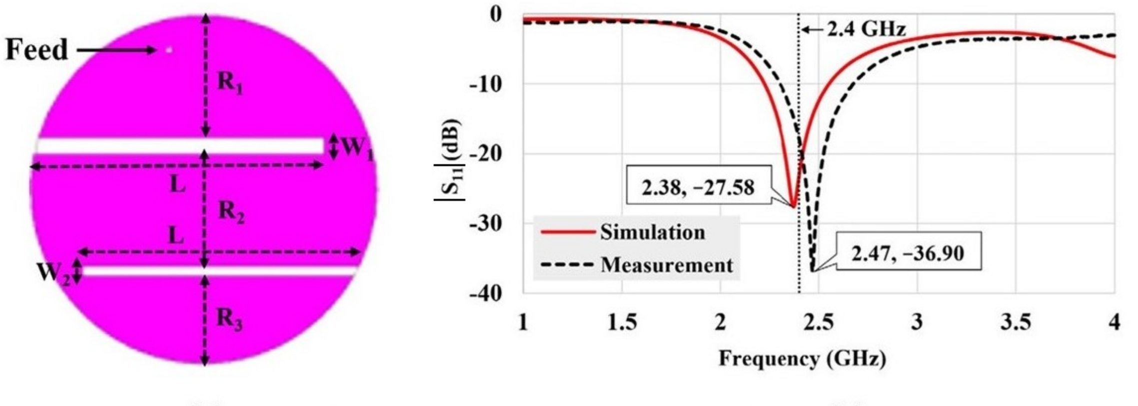

(a)

(b)

Parameter	Value (unit: mm)
R_1	3.5
R_2	3.2
R_3	2.5
W_1	0.5
W_2	0.3
L	8.5

Figure 2.9: (a) Geometry structure of the antenna; (b) Simulation and measurement of the S_{11} [7].

material with a dielectric constant (ε_r) of 3.5 and a loss tangent ($\tan\delta$) of 0.0018. Both simulation and measurement results demonstrated similar 10-dB impedance bandwidths of 13.8% and 14.9%, respectively. The antenna also achieved a peak realized gain of −20.75 dBi and a radiation efficiency of 0.24%.

In [8], the antenna design incorporates a two-section spiral-shaped radiating patch combined with a slotted ground plane, as shown in Figure 2.10. This configuration achieves an ultra-wideband performance of $\geq$ 84% and a volume of 28.85 mm^3. The design is optimized to address detuning issues caused by variations in implantation scenarios or interactions with nearby device components such as batteries and circuits. The antenna employs a Rogers RO6010 laminate for both the substrate and the superstrate, materials known for their high relative permittivity ($\varepsilon_r = 10.2$) and low loss tangent ($\tan\delta = 0.003$). These layers have standard thicknesses of 0.635 mm and 0.127 mm, respectively, aiding in miniaturisation while maintaining high performance.

The designs proposed in [9] demonstrate dual-band functionality, operating at 915 and 2450 MHz. A characteristic of the antenna is its compact size, with a volume

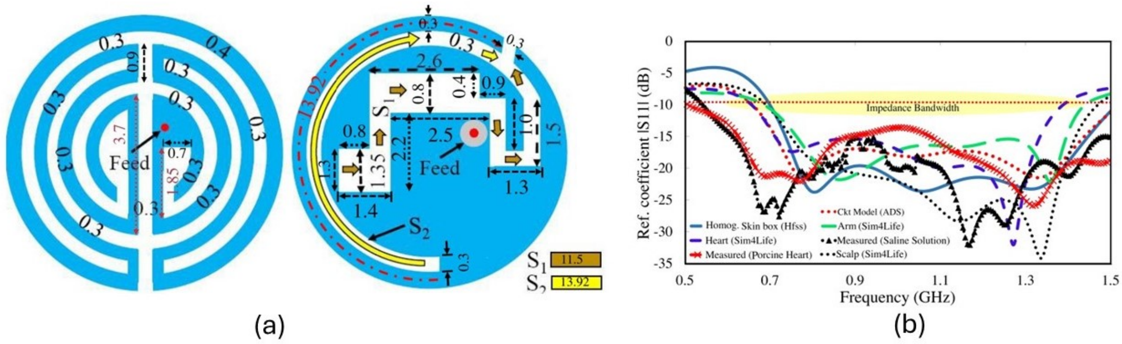

Figure 2.10: (a) Geometry structure of the antenna; (b) Simulation and measurement of the $|S_{11}|$ [8].

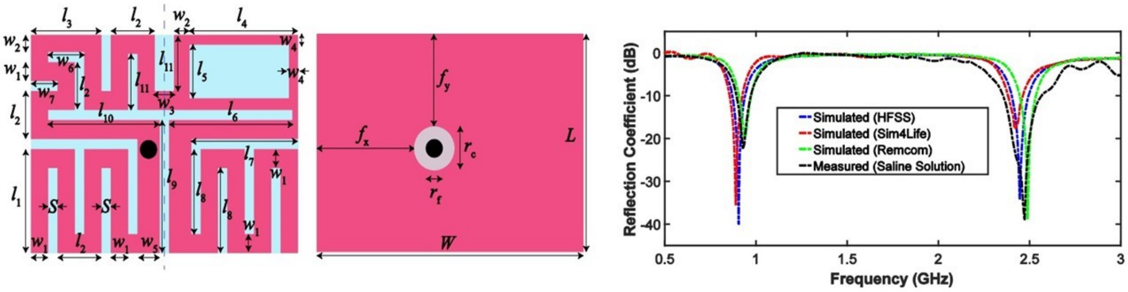

(a) (b)

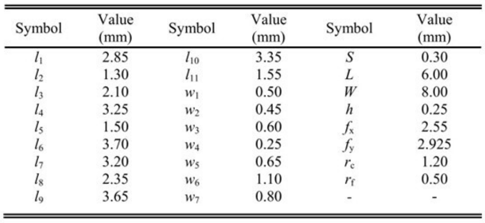

Symbol	Value (mm)	Symbol	Value (mm)	Symbol	Value (mm)
l_1	2.85	l_{10}	3.35	S	0.30
l_2	1.30	l_{11}	1.55	L	6.00
l_3	2.10	w_1	0.50	W	8.00
l_4	3.25	w_2	0.45	h	0.25
l_5	1.50	w_3	0.60	f_x	2.55
l_6	3.70	w_4	0.25	f_y	2.925
l_7	3.20	w_5	0.65	r_c	1.20
l_8	2.35	w_6	1.10	r_f	0.50
l_9	3.65	w_7	0.80	-	-

Figure 2.11: (a) Geometry structure of the antenna; (b) Simulation and measurement of the $|S_{11}|$ [9].

of $24\,\text{mm}^3$ ($8 \times 6 \times 0.5\,\text{mm}^3$). A meandered line slotting technique was applied to the patch to achieve size reduction, and a full ground plane was used to simplify the design, as shown in Figure 2.11. The antenna exhibits gains of -28.5 dBi at 915 MHz and -22.8 dBi at 2450 MHz. Both the substrate and the superstrate are made from Rogers RT/duroid 6010, a material with a relative permittivity of $\varepsilon_r = 10.2$, a loss tangent of $\tan\delta = 0.0023$, and a thickness of $h = 0.25\,\text{mm}$.

The study in [10] introduces a multiband spiral-shaped implantable antenna designed to operate across various frequency bands, including 403 MHz (MICS), 433 MHz (ISM), 1600 MHz (midfield), and 2450 MHz (ISM). The antenna has a compact size of $17.15\,\text{mm}^3$ ($7\,\text{mm} \times 6.5\,\text{mm} \times 0.377\,\text{mm}$), achieved by using a spiral-shaped radiator with symmetrical arms and an open-ended slot in the ground

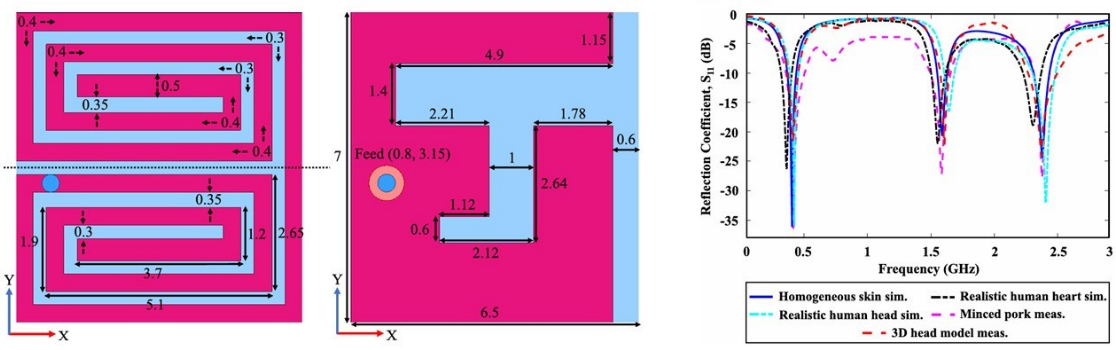

(a) (b)

Figure 2.12: (a) Geometry structure of the antenna; (b) Simulation and measurement of the $|S_{11}|$ [10].

plane, as shown in Figure 2.12. The design exhibits realized gains of −30.5 dBi, −30 dBi, −22.6 dBi, and −18.2 dBi at 402 MHz, 433 MHz, 1600 MHz, and 2450 MHz, respectively. To assess its biotelemetry capabilities, a wireless communication link budget was calculated, supporting data rates of 7 kb/s and 100 kb/s. The antenna substrate and superstrate are made from Rogers RT/duroid 6010, a material with a dielectric constant of $\varepsilon_r = 10.2$ and a loss tangent of $\tan\delta = 0.0035$, with thicknesses of 0.25 mm and 0.127 mm, respectively.

The study in [11] presents a compact dual-band antenna designed for implantable applications in the ISM bands at 915 MHz and 2.4 GHz. The antenna has a small form factor of $6 \times 6 \times 0.25\,\text{mm}^3$ and offers wide bandwidths of 12.6% and 12.8% at the respective frequency bands. It delivers comparatively high gains of −21.8 dBi at 915 MHz and −19.2 dBi at 2.4 GHz, making it well-suited for use in implantable environments. The antenna's performance was assessed in both healthy and adenocarcinoma-affected tissues. To validate the simulated results, a prototype was fabricated and tested in minced pork tissue, which closely mimics real biological conditions. Comparative analysis with recent literature confirms the proposed antenna's effectiveness in terms of compactness, bandwidth, and gain, as shown in Figure 2.13.

The study in [12] presents a compact ultra-wideband (UWB) implantable antenna intended for scalp-based biomedical applications within the 2.4–2.48 GHz ISM band. The antenna is realized on a 0.1 mm thick Liquid Crystal Polymer (LCP) Rogers ULTRALAM substrate and superstrate, selected for its low loss tangent

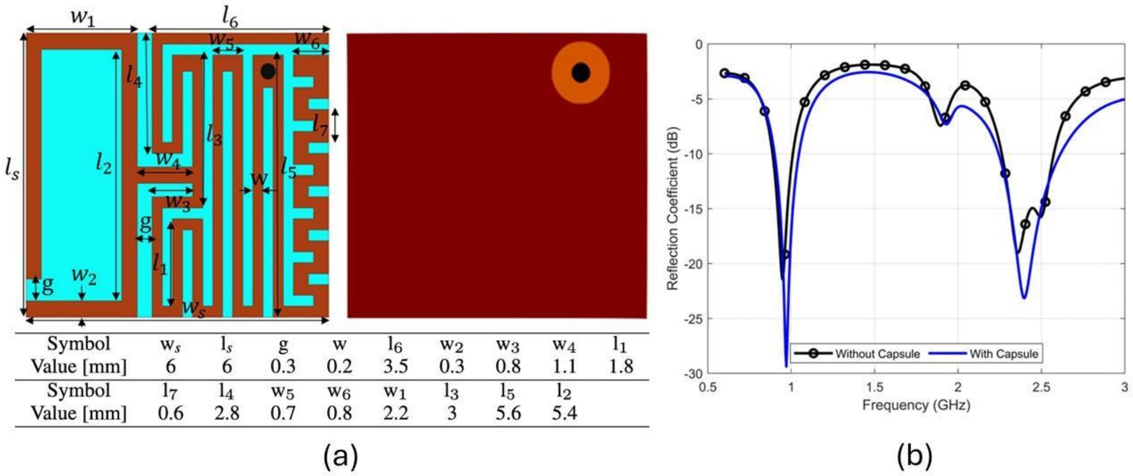

Symbol	w_s	l_s	g	w	l_6	w_2	w_3	w_4	l_1
Value [mm]	6	6	0.3	0.2	3.5	0.3	0.8	1.1	1.8
Symbol	l_7	l_4	w_5	w_6	w_1	l_3	l_5	l_2	
Value [mm]	0.6	2.8	0.7	0.8	2.2	3	5.6	5.4	

Figure 2.13: (a) Geometry structure of the antenna; (b) Simulation of the $|S_{11}|$ [11].

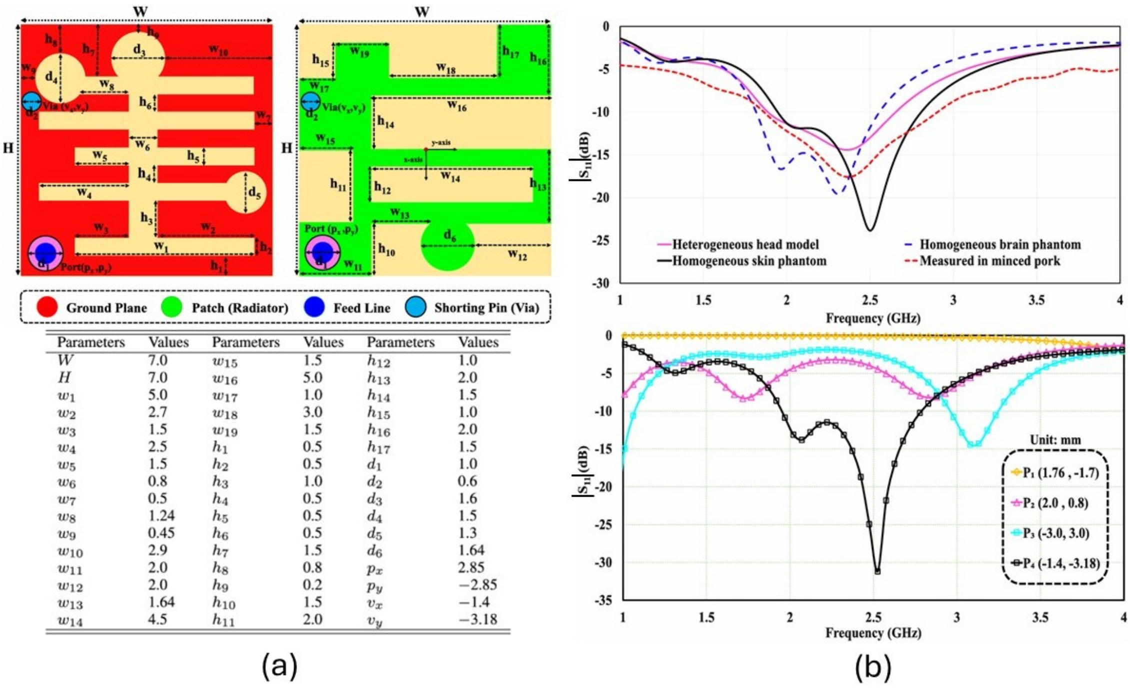

Parameters	Values	Parameters	Values	Parameters	Values
W	7.0	w_{15}	1.5	h_{12}	1.0
H	7.0	w_{16}	5.0	h_{13}	2.0
w_1	5.0	w_{17}	1.0	h_{14}	1.5
w_2	2.7	w_{18}	3.0	h_{15}	1.0
w_3	1.5	w_{19}	1.5	h_{16}	2.0
w_4	2.5	h_1	0.5	h_{17}	1.5
w_5	1.5	h_2	0.5	d_1	1.0
w_6	0.8	h_3	1.0	d_2	0.6
w_7	0.5	h_4	0.5	d_3	1.6
w_8	1.24	h_5	0.5	d_4	1.5
w_9	0.45	h_6	0.5	d_5	1.3
w_{10}	2.9	h_7	1.5	d_6	1.64
w_{11}	2.0	h_8	0.8	p_x	2.85
w_{12}	2.0	h_9	0.2	p_y	−2.85
w_{13}	1.64	h_{10}	1.5	v_x	−1.4
w_{14}	4.5	h_{11}	2.0	v_y	−3.18

Figure 2.14: (a) Geometry structure of the antenna; (b) Simulation of the $|S_{11}|$ [12].

($\tan\delta = 0.0025$), relative permittivity ($\varepsilon_r = 2.9$), flexibility, and biocompatibility. The design occupies a small volume of 9.8 mm^3 ($7 \times 7 \times 0.2$ mm^3) and incorporates a shorting pin along with both open- and close-ended slots to facilitate miniaturization, improve impedance matching, and expand bandwidth. The antenna demonstrates a wide impedance-matched bandwidth of 1038.7 MHz and a peak gain of −20.71 dBi, making it suitable for implantable use, as illustrated in Figure 2.14.

The antennas presented in [1–8] are not suitable for leadless cardiac pacemaker

(LCP) devices due to their larger dimensions compared to commercially available LCPs like Nanostim (42 mm × 5.9 mm) and Micra (25.9 mm × 6.7 mm). Although some compact antenna designs have been introduced in the literature, they exhibit limited bandwidth performance, as reported in [9, 10].

2.8.1.2 Flexible Antenna Design

These antennas are designed to bend or flex along curved surfaces, making them ideal for applications where the antenna must adapt to the contours of the implantation site, such as around cylindrical or irregularly shaped organs. Conformal designs improve comfort and compatibility with the surrounding biological environment while maintaining effective performance. Numerous conformal antenna designs have been proposed to achieve broad bandwidth characteristics. For example, in [13], a wideband antenna is proposed for MIMO applications, which enhances real-time communication by supporting high channel capacity while mitigating frequency detuning effects. The design is achieved using folding and meandering techniques, as shown in Figure 2.15. This MIMO configuration, consisting of two antenna elements, operates in the 0.61–1.51 GHz range, providing a fractional bandwidth (FBW) of 84.91%. The antenna achieves a maximum gain of −30.4 dBi and ensures a high isolation level greater than 20 dB, minimizing mutual coupling between elements. The specific absorption rate (SAR) is 0.0202 W/kg at a transmission power of −16 dBm, and the link margin (LM) is 20 dB at a distance of 2 meters. The antenna has volume of $30.5 \times 15 \times 0.04\,\text{mm} = 18.3\,\text{mm}^3$.

In [14], an ultra-wideband conformal capsule antenna with a volume of 18 mm^3 is designed for use in biomedical systems. The antenna employs a compact slotted planar microstrip structure, fed by a coplanar waveguide, and is constructed from flexible materials to ensure it conforms to the capsule's shape, as shown in Figure 2.16. Operating within the 2.45-2.48 GHz ISM band, it achieves ultra-wideband performance with a bandwidth of 108.9%. Despite its compact size, the antenna ensures radiation safety and achieves a gain of −25.4 dBi at 2.45 GHz.

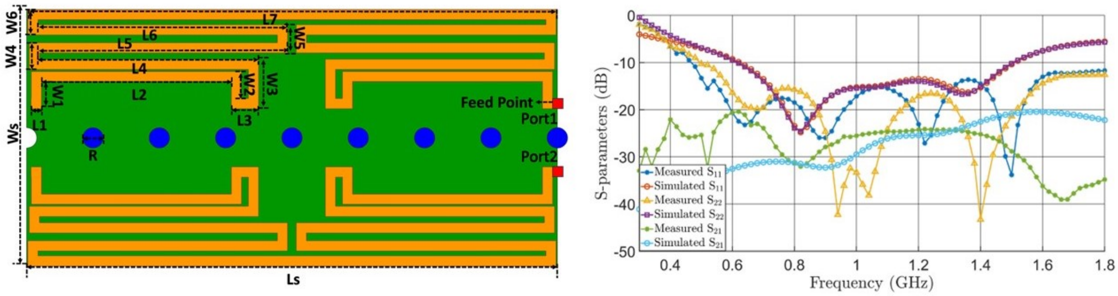

(a) LS = 30.5, WS = 15, L1 = 0.618, L2 = 11.088, L3 = 1.594, L4 = 12.799, L5 = 14.499, L6 = 14.585, L7 = 30.87, W1 = 1.585, W2 =1.585, W3 =2.9,W4 =1.5625, W5 =2.9,W6 = 1.4875, and R = 0.6 (unit: mm). (b)

Figure 2.15: (a) Geometry of the antenna structure; (b) Simulated $|S_{11}|$ response [13].

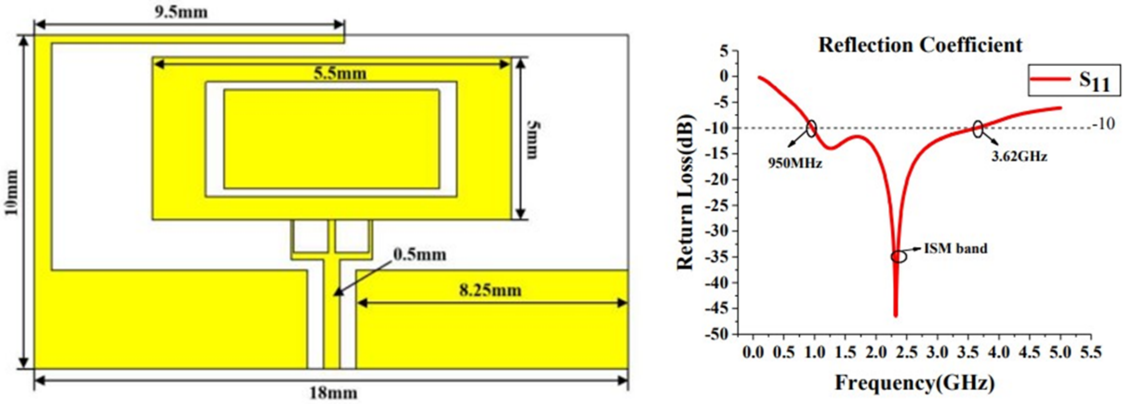

(a) (b)

Figure 2.16: (a) Geometry of the antenna structure; (b) Simulated $|S_{11}|$ response [14].

2.8.2 3D Antenna Type

In [15], a 3D implantable MIMO antenna is proposed to operate at 915 MHz and 2.45 GHz, both within the ISM frequency bands. The antenna features a meandered geometry with capacitive regions between the meandered arms and a partially slotted ground plane to maintain compact overall dimensions, as shown in Figure 2.17. Its total volume is 118.75 mm^3 (5 × 5 × 4.75 mm). MIMO channel parameters and safety assessments indicate favorable performance. Each antenna element exhibits peak specific absorption rate (SAR) values of 306.19 W/kg at 915 MHz and 252.36 W/kg at 2.45 GHz. The antenna is designed for high-speed data transmission, supporting a bit rate of 120 Mb/s and communication distances of up to 8 meters

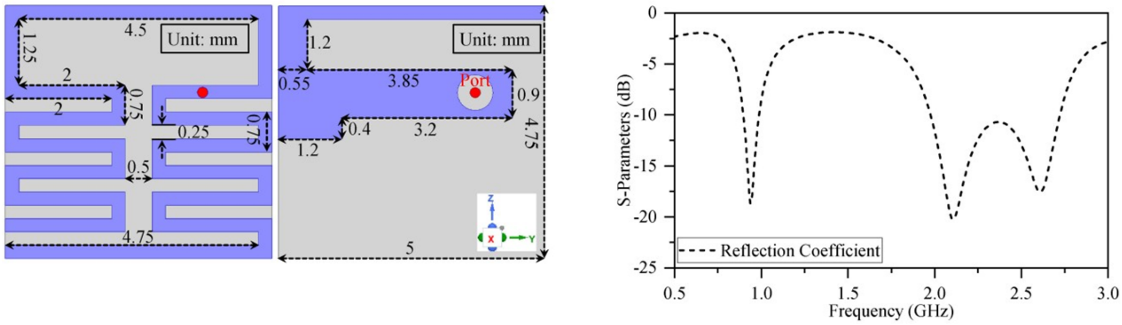

(a) (b)

Figure 2.17: (a) Geometry structure of the antenna; (b) Simulation of the $|S_{11}|$ [15].

at 915 MHz and 5.2 meters at 2.45 GHz.

2.9 Summary

This chapter has outlined the key aspects of implantable antenna design, providing a structured foundation for understanding this complex field. It began by discussing essential requirements and standards, with an emphasis on safety, power constraints, and accurate modeling. The influence of human tissue properties—such as conductivity and permittivity—on antenna performance was also examined. A solid theoretical basis was established to support the designs and analyses presented in later chapters.

Evaluation methods and techniques were introduced to ensure accurate performance assessment, and a step-by-step methodology was provided to guide the design process. Finally, the literature review highlighted prior research and key contributions in this area. Overall, this chapter equips the reader with the necessary knowledge and tools to explore implantable antenna design in greater depth, setting the stage for the more advanced topics covered in subsequent chapters.

CHAPTER 3

Compact Antenna With Broadband Wireless Biotelemetry for Future Leadless Pacemakers

This chapter introduces a wideband antenna tailored for next-generation leadless cardiac pacemakers (LCPs). Designed to overcome detuning challenges, the antenna offers a wide bandwidth, improving channel capacity and enabling the integration of advanced features in LCPs. The complex properties of the human body and the interaction between implantable antennas and electronic devices often cause detuning effects. To mitigate these issues, a broad bandwidth is critical for maintaining stable performance. With a compact volume of 9.44 mm^3, the antenna achieves a bandwidth of 3.39 GHz, resulting in a fractional bandwidth (FBW) of 138%. It covers a wide frequency range from 0.76 to 4.15 GHz, encompassing ISM bands at 0.869, 0.915, and 2.45 GHz, the WMTS band at 1.4 GHz, and the midfield band at 1.6 GHz. Simulations performed on a homogeneous phantom (HP) representing heart tissue show antenna gains of -32.4, -27.94, and -19.8 dBi at frequencies of 0.915 GHz, 1.4 GHz, and 2.45 GHz, respectively. Furthermore, the antenna demonstrates low Specific Absorption Rate (SAR) values in a full-body model (FBM), well below the safety limits of 1.6 W/kg for 1 g of tissue and 2.0 W/kg for 10 g of tissue. A link budget analysis, conducted at a data rate of 10 Mbps, assesses the telemetry range.

Experimental measurements of the antenna in minced pork tissue closely match the simulation results, confirming the practical performance of the antenna.

3.1 Introduction

Recently, the demand for miniaturized antennas in implantable medical devices (IMDs) has surged, particularly for wireless biotelemetry applications. Among these devices, pacemakers are crucial for monitoring and regulating heartbeats. However, traditional pacemakers (TP) face significant challenges related to transvenous leads, which can lead to serious complications, including infections. Studies reveal that approximately 1 in 14 patients experience lead-related complications, contributing to a mortality rate of 20% among those affected [79]. To overcome these critical issues, leadless cardiac pacemakers (LCPs) offer a promising solution for wireless pacing [80]. LCPs bring several advantages, such as cost-effectiveness, reduced invasiveness, and improved efficiency. These innovative devices are implanted directly into the heart, as depicted in Figure 3.1, and rely on implantable antennas to facilitate remote monitoring by healthcare providers using smartphones and computers. Despite their potential, the design of compact antennas for LCPs is not without challenges. The limited space available and the need for wideband performance make this task complex. Deep tissue placement introduces additional obstacles, including propagation losses in cardiac tissue that can attenuate RF signals. Therefore, careful antenna design is essential, focusing on optimal frequency selection and improved radiation efficiency. Furthermore, variations in human tissue properties due to age and changes in the implantation site add layers of complexity that designers must navigate. By addressing frequency detuning related to these variations and increasing the bandwidth of implantable antennas, channel capacity can be significantly improved. A wider bandwidth translates into higher data rates, which are crucial for integrating advanced features into LCPs. As technology advances, further developments in leadless pacing will undoubtedly require enhanced data transmission capabilities to support dynamic device programming and improved monitoring [81]. Ultra-wideband antennas offer an effective approach to optimizing LCP battery life

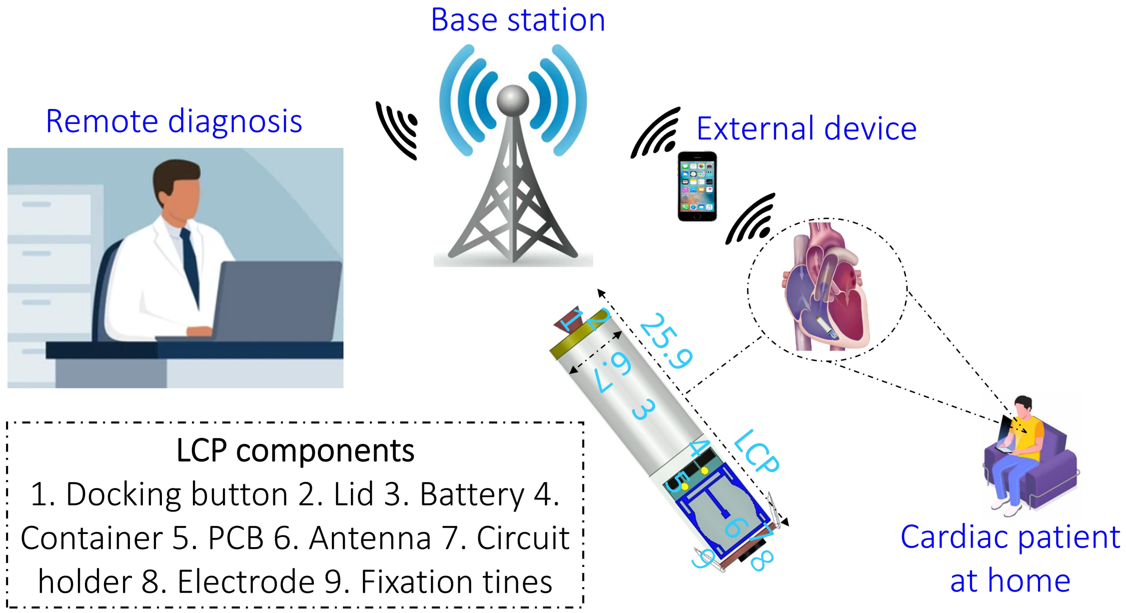

Figure 3.1: The architecture of the leadless cardiac pacemaker and its components.

through intermittent data transmission, activating only when necessary. These innovations have the potential to greatly enhance adaptability and patient outcomes. However, achieving a wide bandwidth while maintaining a compact antenna size remains a pressing challenge. Successfully addressing this issue could lead to significant advancements in the design of implantable antennas for LCPs, allowing us to strike a vital balance between miniaturisation and performance [82].

Various implantable antenna designs have been proposed to achieve wide bandwidth while ensuring compact antenna size [1, 3–6, 8, 83]. In [1], coupled small loop antennas are utilized to achieve a wide bandwidth of 74.1%. Capacitance loading techniques are employed in [3] to obtain a bandwidth of 20.5%. Similarly, metamaterials are used in [4] to achieve a wide bandwidth of 88.6%. The ground plane is truncated in [6] to attain a bandwidth of 40.8%. In another study [8], the authors utilized a spiral-shaped patch and a high permittivity substrate to achieve a bandwidth of 84% thanks to the inductive nature of the spiral structure. However, the antennas presented in [1, 3, 4, 6, 8] are not suitable for LCPs due to their larger dimensions compared to commercially available LCPs such as Nanostim (42 mm × 5.9 mm) and Micra (25.9 mm × 6.7 mm). More compact antenna designs have been reported in the literature, but they often suffer from narrow bandwidths.

For instance, in [7], an antenna with a volume of 39.3 mm^3 with a bandwidth of 14.9% was designed. Similarly, in [9], an antenna with dimensions of 24 mm^3 and a bandwidth of 8.57% is introduced. In another study [10], the authors presented an antenna with dimensions of 17.15 mm^3, operating at 2.45 GHz with a bandwidth of 9%. The authors in [84] presented a spiral-shaped antenna with a volume of 6 mm^3, operating at 2.4 GHz and achieving a bandwidth of 21.8%. Finally, [85] introduced an antenna with a volume of 10.66 mm^3 and a bandwidth of 131.6%, overcoming the issue of narrow bandwidth seen in other compact designs.

This research introduces an innovative implantable antenna tailored for next-generation leadless pacemakers, addressing current limitations through its compact size and wide bandwidth. With a volume of just 9.44 mm^3, it stands as one of the most compact implantable antennas documented to date. In particular, it achieves a fractional bandwidth of 138%, which is significantly higher than the leading designs in the field. The extended bandwidth supports high-speed data transmission and advanced pacemaker functions, while improving resistance to detuning caused by tissue variations, ensuring reliable in-body communication. According to the Shannon-Hartley theorem (Equation 3.1), channel capacity (C)—the maximum achievable data rate—is directly proportional to bandwidth (B) and the signal-to-noise ratio (SNR):

$$C = B \times \log_2(1 + \text{SNR}) \tag{3.1}$$

A broadband antenna, such as the one proposed, enhances channel capacity (C), particularly under high signal-to-noise ratio (SNR) conditions, making it ideal for modern pacemaker systems. This performance results from several advanced design strategies, including expanded ground plane slots, a U-shaped slot, additional rectangular slots on the radiating patch, and an inductive shorting pin. To the best of our knowledge, this design sets a new benchmark in fractional bandwidth while maintaining compact physical dimensions relative to the guided wavelength.

3.2 Methodology

3.2.1 Antenna Design

The detailed geometric model of the proposed antenna, with dimensions of 6.2 mm × 6 mm × 0.254 mm (9.44 mm^3), is shown in Figure 3.2. These dimensions are specifically designed to ensure that the antenna fits within a commercial leadless pacemaker. The radiating patch is rectangular and features a prominent U-shaped slot in its center. A shorting pin with a radius of 0.1 mm is positioned at one corner of the patch. In addition, several rectangular slots are placed along the edges of the patch, as shown in Figure 3.2(a). On the opposite side of the patch, a ground plane with a series of enlarged slots is incorporated, as shown in Figure 3.2(b). To achieve wideband performance while maintaining a compact design, reactive loading techniques are employed [86]. These design choices specifically address the requirements for deep tissue placement, especially for leadless pacemaker applications, as discussed in the following subsection. The antenna is fabricated using Rogers RO3003 material, which has a loss tangent ($\tan\delta$) of 0.0010 and a dielectric constant (ε_r) of 3. Both the substrate and the superstrate have a thickness of 0.127 mm, in accordance with standard Rogers material specifications. Figure 3.2(c) provides a side view of the antenna, which is fed through a coaxial connector with a characteristic impedance of 50 Ohms.

3.2.2 Design Evolution

Figure 3.3(a) illustrates the step-by-step progression of the proposed antenna design, divided into six distinct steps. A detailed comparison of the S-parameter (S_{11}) is provided in Figure 3.3(b). The primary objective of this design is to achieve a wide bandwidth while maintaining a compact size.

The design process begins with Step 1, where a rectangular patch antenna with a complete ground plane is introduced, featuring a large U-shaped slot at the center and fed by a coaxial connection. The U-slot introduces both capacitance and inductive loading, which alters the electric field distribution. According to coupled mode theory, these modifications create additional resonant points that expand the

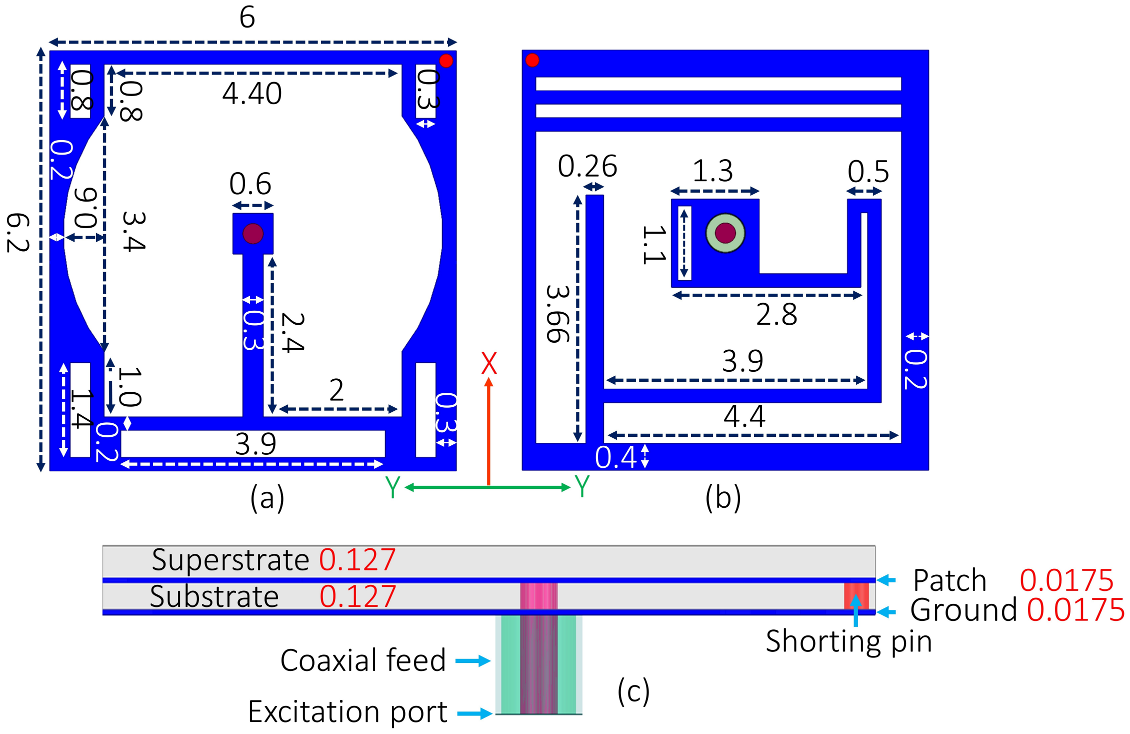

Figure 3.2: The configuration of the proposed implantable antenna is depicted with (a) front, (b) back, and (c) side views (dimensions in mm).

bandwidth [87]. In this initial configuration, the bandwidth ranges from 4.5 to 7.7 GHz.

In Step 2, a shorting pin is introduced in the top right corner, linking the patch to the ground plane (which remains unchanged). This shorting pin acts as a lumped inductor, modifying the current distribution and introducing a new low-frequency resonance around 1.95 GHz, resulting in a dual-band response [88,89]. However, the impedance matching at this new resonance is suboptimal, resulting in a narrowband response at 1.95 GHz.

In Step 3, several rectangular slots are added to the patch—one at the bottom and four at the corners. In addition, the original U-shaped slot is modified to include rounded cuts on both sides. These structural adjustments fine-tune the resonant modes and increase capacitive loading, facilitating the addition of resonances and broadening the impedance bandwidth via stagger-tuned resonance [90]. Each slot enhances capacitance, disrupts current paths, and modifies the effective permittivity, enabling resonance control without increasing the patch size. Consequently, this results in improved impedance matching for the first band and a slight increase in the bandwidth of the second band.

In Step 4, a U-shaped slot is introduced into the ground plane, while the radiating patch remains unchanged. This modification initiates a series of expansions to the ground slot, a process that continues in Steps 5 and 6. The U-shaped slot enhances the bandwidth by adding capacitive loading, lowering the resonant frequency, and improving impedance matching. Additionally, it enables the ground plane to contribute to radiation [91], thereby enhancing overall antenna performance. As a result, the dual-band response is maintained, with the lower frequency band shifting downward by approximately 500 MHz, while the higher frequency band shifts upward by about 1.2 GHz. This leads to a broader bandwidth ranging from 3.43 to 5.8 GHz.

In Step 5, the U-shaped slot in the ground plane is further enlarged, modifying the antenna's effective dielectric constant. This modification lowers the resonant frequency and enhances impedance matching over a wider frequency range. The impact on antenna performance is significant, as illustrated in the S_{11} plot (purple line). Consequently, the first and second frequency bands begin to merge, resulting in a wider bandwidth from 1.17 to 4.34 GHz.

In the final step (proposed antenna), two additional slots are introduced at the top of the ground plane. These slots create new current paths that couple with existing resonant modes, improving impedance matching and further widening the bandwidth [92]. This distributed tuning approach for inductance and capacitance stabilizes resonance points across different conditions and supports multi-band operation for effective in-body medical telemetry. Ultimately, a broad bandwidth of 3.39 GHz is achieved, covering a frequency range from 0.76 GHz to 4.15 GHz. This range effectively includes the ISM bands (0.869, 0.915, and 2.45 GHz), the WMTS band (1.4 GHz), and the midfield band (1.6 GHz).

3.2.3 Simulation and Measurement Configuration

The proposed antenna design was successfully simulated using the HFSS simulator, demonstrating its potential for use in essential medical devices. It is housed inside an LCP capsule that has been carefully sized to match the commercial Mi-

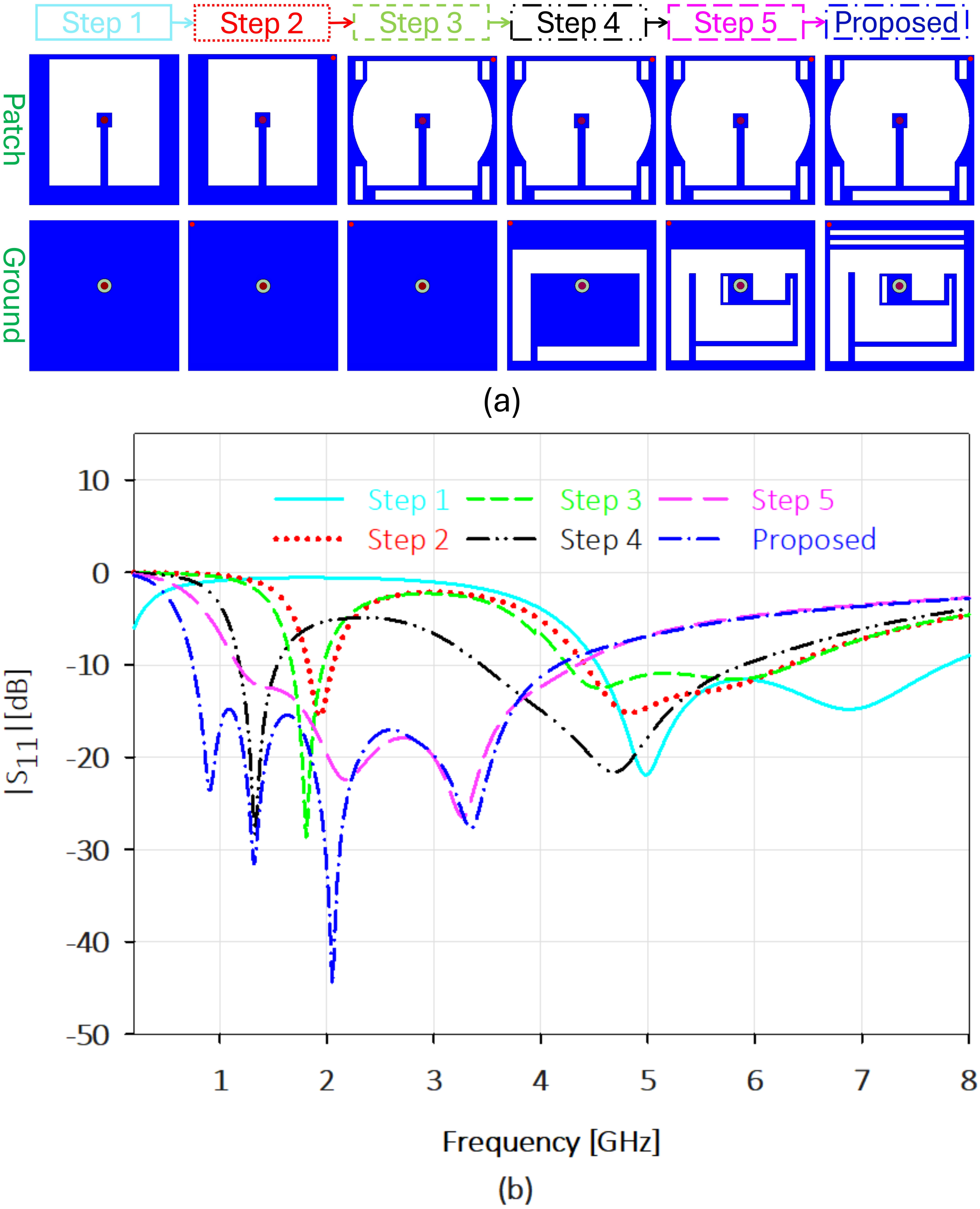

Figure 3.3: (a) Evolution of design adjustments. (b) $|S_{11}|$ at different design steps.

cra pacemaker, which measures 25.9 mm in length and 6.7 mm in diameter. The LCP capsule is made from biocompatible ceramic alumina (Al_2O_3, with $\varepsilon_r = 9.8$) and is only 0.2 mm thick, ensuring patient safety. Inside the capsule, the antenna is strategically positioned alongside a battery and dummy electronics, providing a compact and practical solution for medical applications. The antenna is placed at a depth of 30 mm at the center of a homogeneous phantom (HP) as shown in Figure 3.4(a), effectively simulating real-world conditions. To replicate the dimensions of a typical human heart, the HP measures 120 mm × 80 mm × 60 mm, following the guidelines outlined in [93]. The design also takes into account the heart's electrical properties at key frequencies of 0.915, 1.4, and 2.45 GHz—critical for biomedical applications (915 MHz for ISM use, 1400 MHz for telemetry, and 2450 MHz for wireless communication; see Table 3.1 in [94]). A radiation box was constructed to ensure placement at a distance greater than $\lambda_o/4$ from the edges of the antenna, ensuring accurate measurements [95]. Figure 3.4(b) shows the antenna integrated into a full-body model (FBM) positioned at the heart's location, which helps provide a realistic evaluation of its performance. Prototype antennas were then fabricated and installed into a 3D-printed leadless pacemaker capsule, with actual components replacing the simulated dummies for comprehensive testing, as illustrated in Figure 3.4(c). For the measurements, the LCP was placed at the center of a container filled with minced pork, which serves as a tissue-equivalent medium. The antenna's S-parameters were measured using a Keysight P5004 Vector Network Analyzer (VNA), with high-quality cables ensuring accurate and reliable data, as shown in Figure 3.4(d). The fabricated antenna was connected to the VNA after undergoing standard calibration procedures (open, short, and load). These techniques eliminated errors, including cable losses and connector mismatches. Once calibrated, the VNA was set to the desired frequency range. Radiation patterns were then measured in a SATIMO anechoic chamber, where a signal generator powered a high-gain horn antenna as the transmitter (Tx) and the proposed antenna acted as the receiver (Rx). The Tx and Rx antennas were maintained at a constant distance of 1 meter, as shown in Figure 3.4(e), confirming the antenna's effectiveness and its potential for practical use.

3.3 Performance Analysis and Discussion

The assessment of the antenna's suitability for deep tissue applications involved a series of detailed analyses. This process included simulations conducted in both a

Table 3.1: Dielectric Properties of Heart Tissue at Various Frequencies

Phantom type	Frequency (GHz)	Conductivity (S/m)	Relative permittivity
HP	0.915	1.2378	59.796
	1.4	1.5132	57.538
	2.45	2.2561	54.814

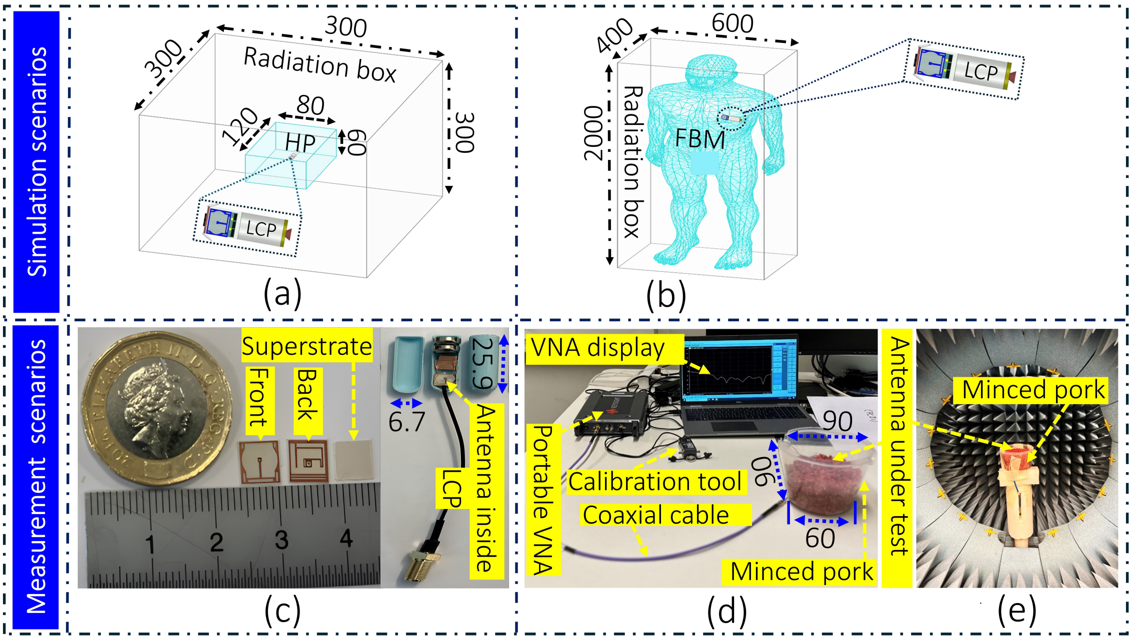

Figure 3.4: The setups are illustrated as follows: (a) Homogeneous phantom (HP), (b) Full body model (FBM), (c) Fabricated prototypes, (d) Setup for S-parameter measurements, and (e) Setup for gain measurements (dimensions in mm).

homogeneous phantom and a full-body model, followed by experimental validation using a tissue-simulating medium.

3.3.1 Bandwidth Characteristics

In antenna design, bandwidth represents the frequency range over which the antenna operates efficiently, maintaining critical performance metrics such as impedance matching, gain, and radiation efficiency. For implantable antennas, achieving a wide bandwidth is paramount to ensuring reliable functionality under varying conditions, such as tissue property changes, implantation depth, and surrounding environmental factors. Figure 3.5 illustrates the S-parameter (S_{11}) for the proposed antenna under various scenarios, both with and without LCP capsule. The antenna exhibits a broad bandwidth and excellent impedance matching across all intended frequency ranges. The recorded bandwidths are 3.39 GHz without LCP, 3.35 GHz with LCP, 3.55 GHz in the full-body model (FBM), and 3.63 GHz in measurements. The measured S_{11} data indicates slightly wider bandwidths, likely due to variations in tissue properties between. A frequency shift of approximately 0.5 GHz between the simulated and measured results is primarily attributed to differences in the permittivity of minced pork versus human heart tissue. The permittivity of minced pork ranges from 48 to 50, with conductivity between 0.6 and 2 S/m. These variations significantly affect the frequency shift, highlighting the importance of using accurate tissue-mimicking materials for experimental validation. The ultra-wide bandwidth achieved by the proposed antenna serves several critical roles in implantable applications. Biomedical environments present challenges such as frequency detuning caused by variations in tissue properties due to age, hydration, or differences in implantation sites. The wide bandwidth ensures stable communication despite these factors. Furthermore, the antenna's operational range (0.76–4.15 GHz) covers key medical communication bands, including ISM (0.869, 0.915, and 2.45 GHz), WMTS (1.4 GHz), and midfield (1.6 GHz) bands. This multi-band compatibility reduces the need for multiple narrowband antennas, simplifying device design and enhancing efficiency. Moreover, according to Shannon's channel capacity theorem, a wider bandwidth supports higher data rates, which are critical for next-generation medical devices such as leadless cardiac pacemakers (LCPs). While not all current applications require such extensive bandwidth, emerging medical technologies increasingly demand higher data rates, making this feature vital for future innovations.

3.3.2 Radiation Patterns

The radiation pattern of an antenna represents how it radiates energy in space, highlighting its directionality and coverage. For implanted antennas, understanding this pattern is vital as the properties of the tissue and depth of implantation significantly influence the performance. As illustrated in Figure 3.6, the radiation patterns of the proposed antenna are evaluated in different scenarios at frequencies of 0.915, 1.4,

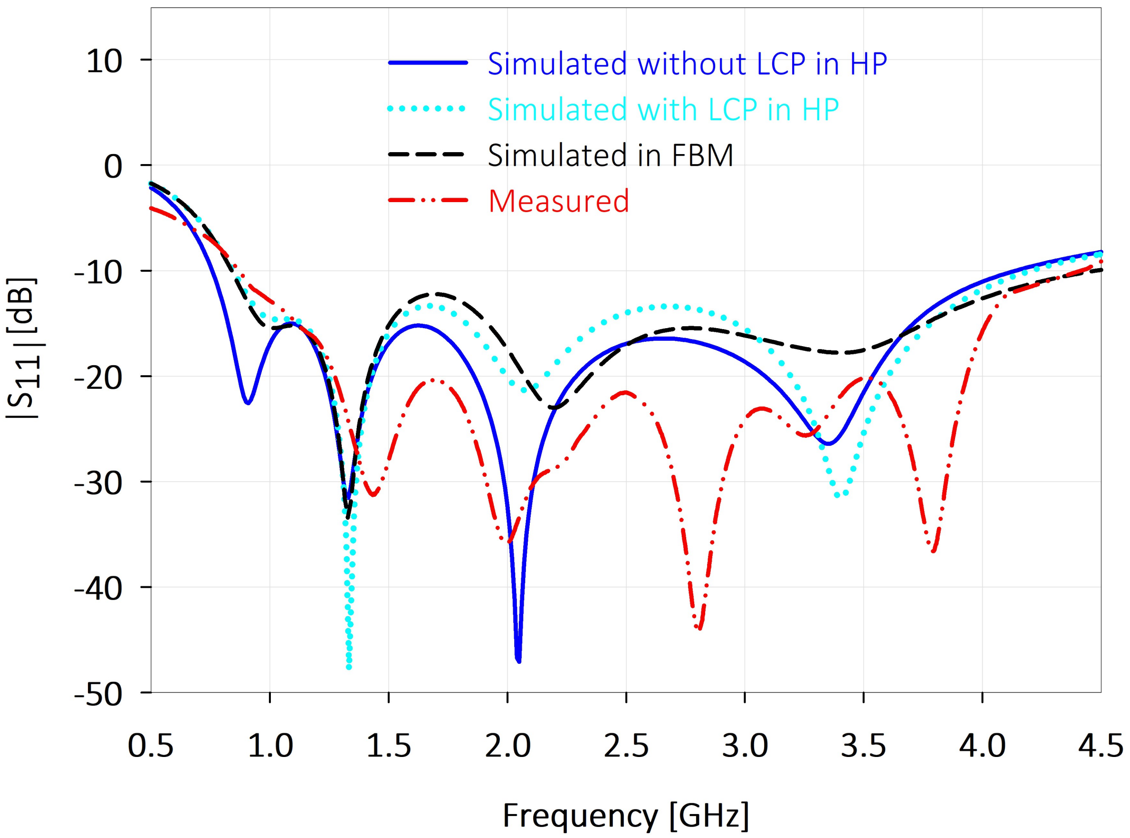

Figure 3.5: Analysis of the $|S_{11}|$ parameter for the proposed antenna across various scenarios, including configurations with and without the leadless cardiac pacemaker (LCP).

and 2.45 GHz. The findings demonstrate coverage in all directions. When LCP is not applied, the simulated peak gains in HP at these frequencies are −32.4, −27.94, and −19.8 dBi, respectively. However, when LCP is utilized, these gains drop to −34.6, −31, and −20 dBi. In the same frequency range, the maximum gains for the FBM are recorded at −22.06, −32.01, and −35.76 dBi, with corresponding measured gains of −29.3, −25.8, and −19.4 dBi. It is crucial to recognize that the depth of implantation greatly influences the gain of implanted antennas [96]. Additionally, the phantom size used in the simulations is larger than the one used for the measurements, which accounts for the observed slight difference, with the simulated gain values being somewhat lower than the measured ones. The radiation patterns in the H-plane exhibit exceptional stability across the evaluated frequencies. This stability is attributed to the antenna's inherent impedance matching over the operational bandwidth. Variability in tissue properties, such as changes in dielectric constant or conductivity across different layers, has minimal impact on the H-plane pattern due to the inherent impedance stability of the antenna in the specified operational bandwidth. More specifically, key design elements of the antenna, such as specific slot configurations and the short pin, improve impedance matching, thus reducing the effects of detuning and minimizing pattern distortion across a wide range of frequencies.

Moreover, the current distribution analysis across the patch shows that the current paths contributing to the H-plane radiation remain relatively constant at the targeted frequencies. Therefore, tissue types primarily affect the E-plane patterns, where asymmetry in tissue distribution is more pronounced, especially at the front and back of the antenna. The simulated and measured patterns were validated under a range of tissue conditions and operational depths, confirming the robustness of the design against environmental variability.

As expected, the radiation patterns do not exhibit a perfectly omnidirectional pattern in both the E- and H-planes, which is theoretically unachievable for practical antennas—especially in compact, implantable scenarios. However, the patterns demonstrate approximately omnidirectional behavior, which is suitable for biomedical applications where antenna orientation cannot be controlled. It's also important to note that the radiation plots use a scale from –60 dB to –30 dB, which compresses the range and makes the patterns appear more uniform than they actually are.

3.3.3 Surface Current Distributions

The surface current distribution on an antenna describes how electric currents flow across its surface when excited by an input signal. These currents play a crucial role in the generation of electromagnetic fields responsible for radiation. Analyzing their distribution is essential to understanding the efficiency and radiation characteristics of the antenna. Figure 3.7(a)–(c) illustrate the surface current distributions on the antenna patch at frequencies of 0.915 GHz, 1.4 GHz, and 2.45 GHz, respectively. At 0.915 GHz, as shown in Figure 3.7(a), the surface currents exhibit a consistent flow, starting from the feed port. The strongest current intensity is observed on the right side of the radiating patch. At 1.4 GHz, as shown in Figure 3.7(b), the current distribution shifts, with notable changes along the line near the port and

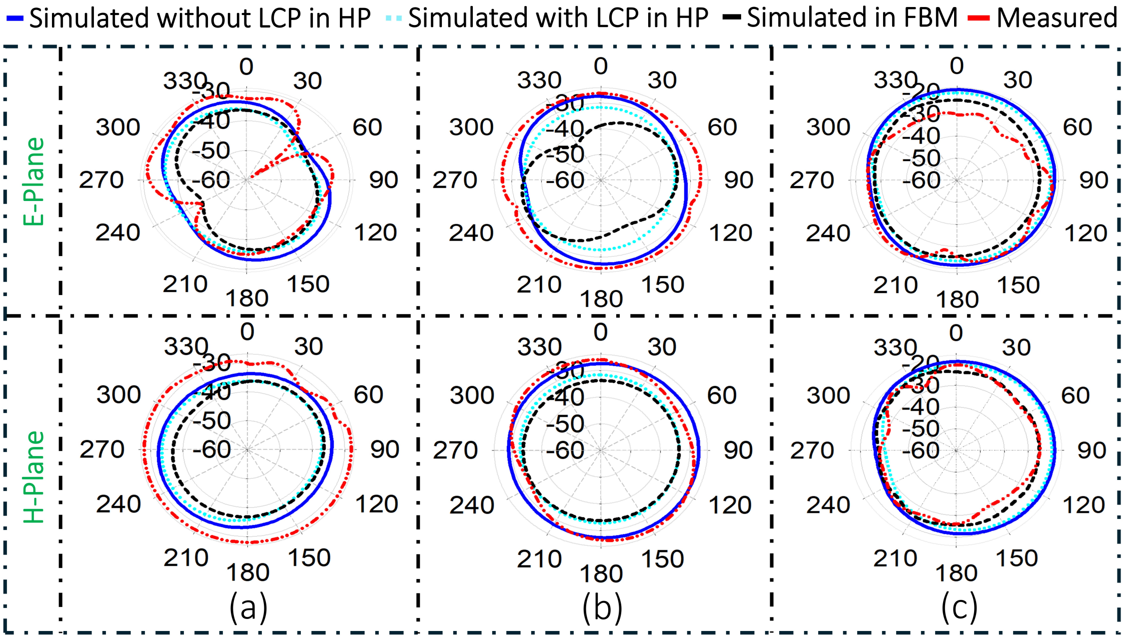

Figure 3.6: Far-field patterns at frequencies of (a) 0.915 GHz, (b) 1.4 GHz, and (c) 2.45 GHz.

Table 3.2: Maximum SAR and Maximum Allowable Power

Phantom type	Frequency (GHz)	SAR W/kg (1g)	MAP (mW)	SAR W/kg (10g)	MAP (mW)
FBM	0.915	262.8	6.08	54.6	36.6
	1.4	378.1	4.23	40.3	49.6
	2.45	556.9	2.87	31.5	63.5

the shorting pin. The current paths are longer than those at 0.915 GHz, with significant current build-up observed on both sides of the patch. At 2.45 GHz, as shown in Figure 3.7(c), the surface current distribution resembles that at 1.4 GHz but with slightly shorter current paths. These currents follow extended routes along the patch, which contributes to the compact design of the antenna while supporting efficient radiation. The changes in current distribution across frequencies reflect the antenna's multi-frequency operation and its ability to maintain stable performance within a compact form factor.

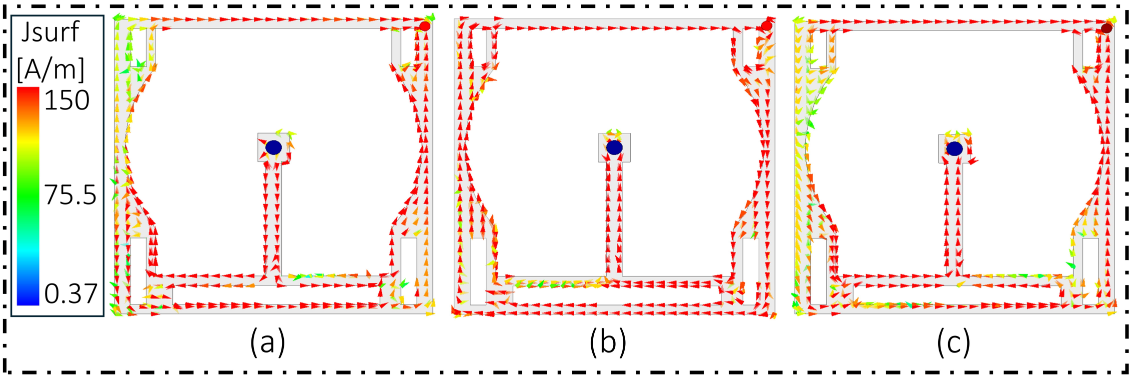

Figure 3.7: Current distribution on the patch at frequencies of (a) 0.915 GHz, (b) 1.4 GHz, and (c) 2.45 GHz.

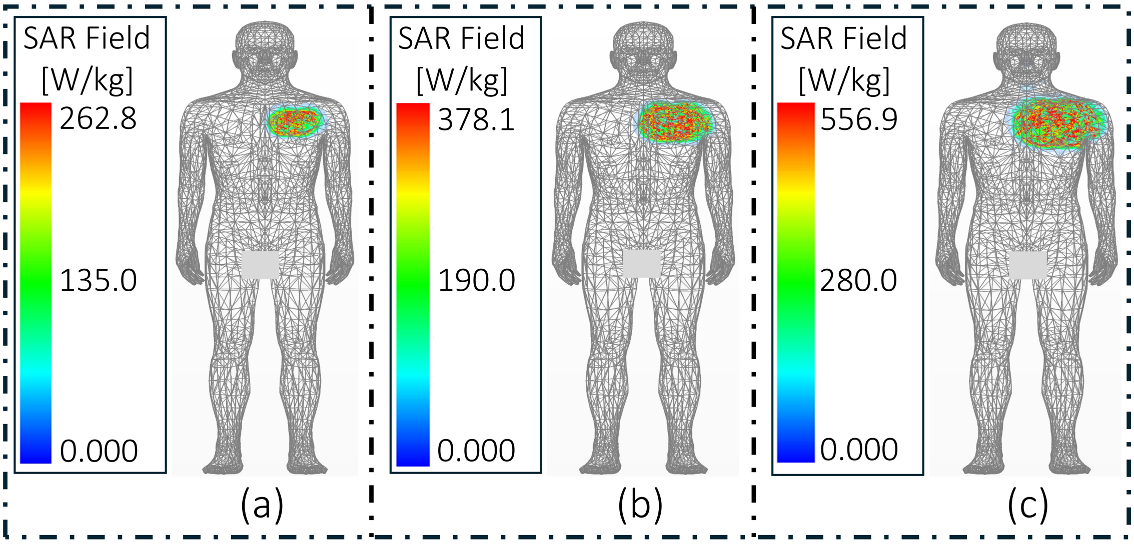

Figure 3.8: SAR values at frequencies of (a) 0.915 GHz, (b) 1.4 GHz, and (c) 2.45 GHz.

3.3.4 Specific Absorption Rate Distribution

The Specific Absorption Rate (SAR) quantifies the amount of electromagnetic energy absorbed by biological tissue when exposed to radiofrequency fields. To comply with safety standards, SAR values must not exceed 1.6 W/kg for 1 gram of tissue and 2 W/kg for 10 grams of tissue, as outlined in relevant health guidelines [33]. In the simulations conducted, the SAR levels within the FBM and the maximum allowed power (MAP) were evaluated. Initially, an input power of 1 W was applied to facilitate comparison with previous studies, However, this resulted in SAR values that exceeded safety limits: greater than 1.6 W/kg for 1 gram of tissue and greater than 2 W/kg for 10 grams of tissue. Figure 3.8(a)–(c) illustrate SAR values at frequencies of 0.915, 1.4, and 2.45 GHz, with the highest SAR value of 556.9 W/kg recorded at 2.45 GHz for 1 gram of tissue, which corresponds to a MAP of 2.87 mW. To meet safety regulations, an input power of −16 dBm was selected according to the European Research Council's guidelines [97]. This input power level ensures compliance with SAR limits while minimizing electromagnetic interference (EMI) with surrounding wireless devices, thereby preventing disruptions in multi-device environments. The SAR and MAP values for the antenna are summarized in Table 3.2. Under an adjusted input power of −16 dBm, the SAR values for the antenna were measured as 0.0066 W/kg at 0.915 GHz, 0.0095 W/kg at 1.4 GHz and 0.0140 W/kg at 2.45 GHz. These values are significantly lower than the safety thresholds of 1.6 W/kg and 2 W/kg, confirming that the antenna SAR levels are within the safe limits for human exposure.

3.3.5 Link Budget Analysis

The performance of the proposed implantable antenna is evaluated using the link budget framework detailed in Chapter 2, Section 2.6.1.4. This method assesses the received power at the external device by accounting for transmission power, antenna gains, propagation losses, and receiver sensitivity. A key metric derived from this framework is the link margin (LM), which reflects the difference between the received power and the minimum receiver sensitivity. For reliable communication, a positive link margin is essential, with a typical design target of at least 20 dB.

In this study, a bit rate of 10 Mbps is assumed. The implantable antenna functions as the transmitter, while the external receiver is modeled as an ideal half-wavelength dipole antenna with a gain of 2 dBi. The transmission power is set to −16 dBm, adhering to SAR safety requirements (see Section 2.4.1). The antenna exhibits directional gains of −32.4 dBi, −27.94 dBi, and −19.8 dBi at operating frequencies of 0.915 GHz, 1.4 GHz, and 2.45 GHz, respectively.

For this analysis, losses due to polarization mismatch and impedance mismatch are excluded, given the antenna's effective matching. All link budget parameters used in the calculations are summarized in Table 3.3.

As shown in Figure 3.9, the proposed antenna achieves maximum communication distances of approximately 12 m, 14 m, and 21 m at 0.915 GHz, 1.4 GHz, and

Table 3.3: Link Budget Parameter Analysis

Varaibale	Parameter	value	Unit
Signal power			
Transmitter Side			
P_t	Transmitted power	-16	dBm
f	Frequency	915, 1400, 2450	MHz
G_t	Antenna gain	-32.4, -27.94, -19.8	dBi
Propagation medium			
L_f	Path loss	Variable	dB
Receiver Side			
G_r	Receiver antenna gain	2	dBi
Noise power			
N_o	Noise power density	-203.93	dBm/Hz
T	Temperature	273	Kelvin
K	Boltzmann constant	1.38×10^{-23}	J/K
Signal quality			
B_r	Bit rate	various	Mbps
BER	Bit error rate	1×10^{-5}	-
E_b/N_o	Ideal PSK	9.6	dB
G_c	Coding gain	0	dB
G_d	Fixing deterioration	2.5	dB

2.45 GHz, respectively. These distances are well beyond the 1–2 m range typical in leadless pacemaker applications, confirming the antenna's suitability for reliable biotelemetry. Despite higher propagation losses at 2.45 GHz, the improved antenna gain at this frequency compensates for the increased attenuation, resulting in the best overall performance in terms of range and link margin.

As shown in Table 3.4, the proposed antenna is evaluated alongside recent state-of-the-art implantable antenna designs. It exhibits the smallest guided wavelength

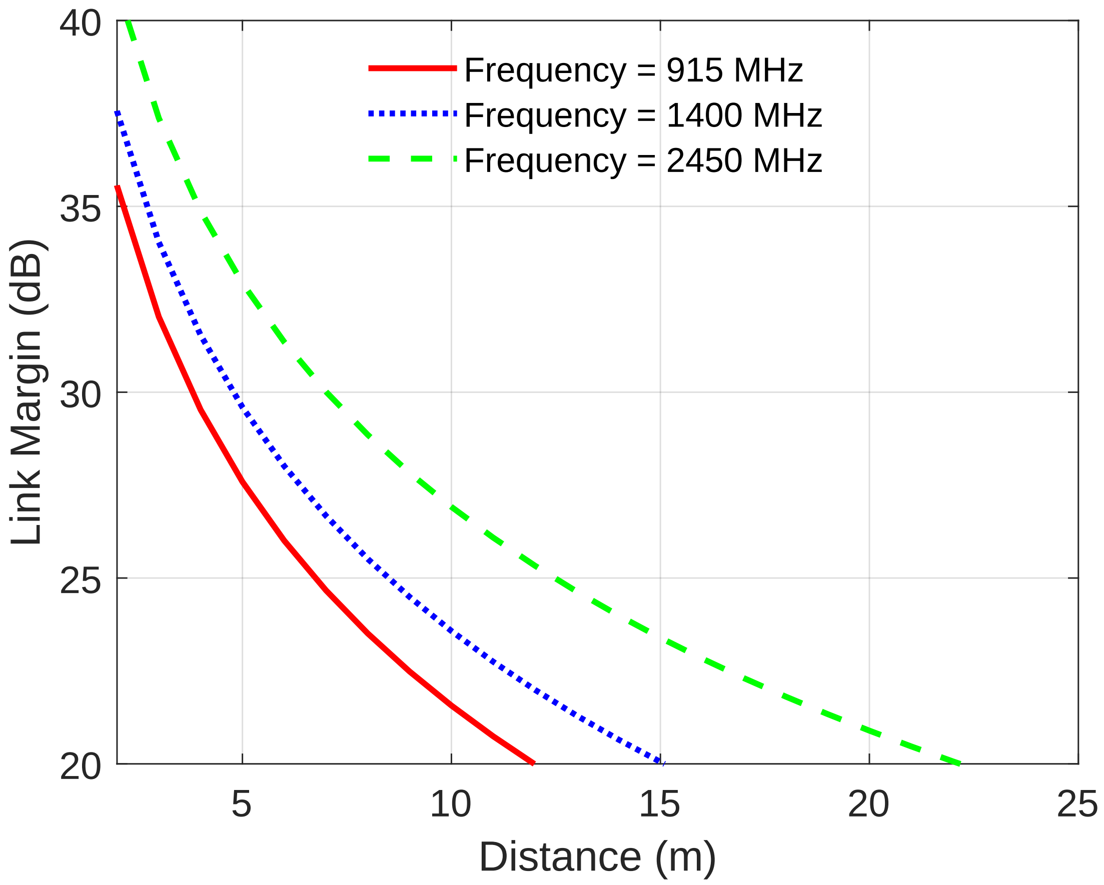

Figure 3.9: Link margin at 10 Mbps across different frequency bands.

and offers the broadest fractional bandwidth (FBW) compared to other implantable antennas reported in the literature. These characteristics make it particularly well-suited for use in pacemaker devices, where operation is required in lossy, heterogeneous heart tissue. To ensure a fair comparison, it is important to contextualise the performance parameters based on the operating frequency, antenna volume, bandwidth, gain, and SAR compliance. First, the proposed antenna operates at 1.4 GHz, which is an intermediate frequency between the MICS (0.403 GHz) and ISM (2.4/2.45 GHz) bands. This positioning enables a balance between acceptable tissue penetration (which improves at lower frequencies) and physical miniaturisation (which improves at higher frequencies). Designs operating at 2.4–2.45 GHz, such as [3,5,83], tend to have inherently smaller physical sizes due to shorter wavelengths, but suffer from higher tissue absorption and SAR values. In contrast, antennas operating at lower frequencies such as 0.433 GHz and 0.915 GHz [1,8,13] demonstrate superior penetration depth but require significantly larger physical volumes to main-

Table 3.4: Comparison of the Proposed Antenna with Previous Designs

Ref.	Frequency (GHz)	Volume (mm^3)	FBW (%)	Gain (dBi)	Size $(\lambda_g)^3$	SAR (W/kg)	
						1-g	10-g
[1]	0.433	240	74.1	-23.19	3.02×10^{-1}	177.1	-
[83]	2.4	121.9	21.5	-33	2×10^{-3}	486	90
[3]	2.45	99.7	20.5	-26.4	1.76×10^{-3}	712.1	-
[4]	2.45	70.4	88.6	-16.5	1.25×10^{-3}	269	-
[5]	2.4	63.8	16.12	-37.3	1.06×10^{-3}	856.4	-
[6]	2.45	59.5	40.8	-16	1.11×10^{-4}	330.4	39.9
[8]	0.915	28.85	84	-30.2	2.66×10^{-5}	796.1	64.1
[7]	2.4	39.3	14.9	-20.75	1.31×10^{-4}	568.2	84.6
[9]	2.45	24	8.57	-22.8	4.26×10^{-4}	807.3	102.4
[13]	0.915	18.3	84.91	-30.4	3.4×10^{-6}	-	-
[10]	2.45	17.15	9	-18.2	3.04×10^{-4}	305	81.7
T.W	1.4	9.44	138	-27.94	1.39×10^{-6}	378.1	40.3

tain resonance and impedance matching. The proposed antenna outperforms many of these in terms of miniaturisation, achieving a volume of only 9.44 mm^3, which is among the smallest reported, especially for frequencies below 2 GHz. Furthermore, the proposed design achieves a fractional bandwidth (FBW) of 138%, the highest among all compared antennas, confirming its ultra-wideband (UWB) nature as defined by FCC and theoretical standards. This broad bandwidth allows for stable performance under various detuning conditions, which is essential for implantable applications. Although the gain of the proposed antenna (-27.94 dBi) is moderate compared to some designs operating at higher frequencies, this is expected due to the lossy nature of tissue and the low profile of the structure. More importantly, the proposed antenna demonstrates strong compliance with SAR constraints, showing values well within the IEEE safety limits. This ensures its suitability for long-term implantation in biomedical applications. In summary, the proposed design presents a favourable trade-off between size, bandwidth, and safety at a mid-range frequency. It effectively bridges the performance gap between antennas designed for low-frequency deep-tissue penetration and high-frequency miniaturisation, offering a balanced and practical solution for next-generation leadless cardiac pacemaker systems.

3.4 Conclusion

A compact ultra-wideband antenna has been designed, simulated, and experimentally verified for use in next-generation leadless cardiac pacemaker (LCP) systems. The impressive performance of the antenna is attributed to innovative design elements, such as enlarged slots in the ground plane, a U-shaped slot, additional rectangular slots in the radiating patch, and an inductive shorting pin. As a result, the antenna occupies a small volume of 9.44 mm^3 and achieves a broad bandwidth of 3.39 GHz (FBW = 138%). It demonstrates antenna gains of -32.4 dBi, -27.94 dBi, and -19.8 dBi at frequencies of 0.915 GHz, 1.4 GHz, and 2.45 GHz, respectively. The simulation was performed within a human phantom model, and the experimental measurements were conducted in minced pork tissue. Both the simulation results and experimental data confirm stable impedance matching, wide bandwidth, high gain, and consistent radiation patterns. The SAR values are within the IEEE safety limits, confirming the suitability of the antenna for LCP applications.

CHAPTER 4

A Low-Profile Implantable Antenna for Heart Implants

This chapter presents an ultra-compact, ultra-wideband antenna specifically designed for use in LCPs. The antenna has a compact dimension of 8.33 mm^3 and achieves a -10 dB bandwidth of 4.33 GHz, resulting in a fractional bandwidth of 152.7% that spans from 0.67 to 5 GHz. It effectively facilitates communication across a variety of critical frequency bands, such as the Industrial, Scientific, and Medical (ISM) bands at 0.915 GHz and 2.45 GHz, the Wireless Medical Telemetry Service (WMTS) band at 1.4 GHz, and the midfield band at 1.6 GHz. The simulation results indicate antenna gains of -31.3 dBi at 0.915 GHz, -25.8 dBi at 1.4 GHz, and -21.9 dBi at 2.45 GHz. The antenna also demonstrates high SAR values, with a peak of 320.4 W/kg at 0.915 GHz, 332.8 W/kg at 1.4 GHz and 464.1 W/kg at 2.45 GHz. The communication range between the implantable transmitter and the external receiver was estimated by conducting a link budget analysis at data rates of 10 Mbps and 25 Mbps to ensure reliable wireless telemetry. A prototype was fabricated and experimentally tested using minced pork as a tissue-equivalent medium. The measured results showed close agreement with the simulated predictions, validating the antenna's performance.

4.1 Introduction

Recent developments in wireless biotelemetry have increased the demand for smaller antennas intended for implantable medical devices (IMDs). One of the most crucial applications is in cardiac pacemakers, which help improve the quality of life for individuals with bradycardia, a condition in which the heart rate is abnormally slow. Traditional cardiac pacemakers (TCPs) are surgically implanted beneath the skin, with leads (wires) passing through the veins to the heart. Despite their widespread use, TCPs often face complications related to their leads, which can cause potential problems. Complication rates are reported to range between 7.76% and 12.4% during the first 90 days, with almost half of these problems associated with lead failure and infections. In response to these challenges, compact leadless cardiac pacemakers (LCPs) have emerged as a promising alternative. These devices offer advantages such as smaller size, reduced invasiveness, improved efficiency, and cost-effectiveness. Unlike TCPs, LCPs eliminate the need for pacing leads, as the entire device is implanted directly into the right ventricle. A key component of wireless LCPs is the implantable antenna, which facilitates essential wireless communication, enabling remote monitoring of cardiac activity via mobile devices and digital systems. The design of compact antennas for LCPs comes with several challenges, including spatial limitations and the need for wideband frequency coverage. To address this, achieving ultra-wideband properties is crucial, as it helps counteract frequency shifts caused by the varying characteristics of human tissue. These tissue variations can change due to factors such as age or location of the implantation. Expanding the antenna's bandwidth not only solves frequency detuning issues but also increases channel capacity. A wider bandwidth supports higher data rates, which are essential for advanced features in LCPs, such as faster communication speeds. According to Shannon's channel capacity theorem, a larger bandwidth allows for more data to be transmitted in a given period compared to narrowband antennas. As technology advances, leadless pacemakers will require higher data transmission rates to support new functionalities and enhance overall device performance. For example, real-time heart monitoring and transmission of critical data will require faster data rates to provide timely and accurate medical assessments. In addition, improved data rates will allow for more sophisticated functions, such as dynamic programming and real-time battery monitoring, which ultimately lead to better patient outcomes. However, designing antennas for LCPs presents the challenge of balancing a broad bandwidth with the constraints of miniaturizing the antenna. Efforts to make antennas smaller often come with trade-offs that can limit their ability to cover a wide frequency range effectively.

Several designs of implantable antennas have been suggested with the goal of achieving both wide bandwidth and compact size [1, 3–6, 8, 98, 99]. In [1], a bandwidth of 74.1% has been achieved using coupled small loop antennas. In [3], a bandwidth of 20.5% is achieved using capacitance loading techniques. Similarly, metamaterials highlighted in [4] attain a bandwidth of 88.6%. Utilizing two orthogonal slots on the ground plane, [5] achieves a bandwidth of 16.3%. Truncating the ground plane, [6] attains a bandwidth of 40.8%. Utilising open-ended slots on both the patch and ground achieve a bandwidth of 19.6% [99]. In [8], the combination of a high permittivity substrate with a spiral-shaped radiator facilitates an 84% bandwidth, capitalizing on the inductive characteristics inherent in the spiral geometry. Nevertheless, the antennas discussed in [1–6, 8, 99] are unsuitable for LCPs because they are larger in size when compared to current commercial models like the Micra, which measures 25.9 mm by 6.7 mm. Although miniaturized designs are available in existing research, bandwidth limitations are frequently encountered. An example from [7] illustrates an antenna with a volume of 39.30 mm^3 and achieves a fractional bandwidth of 14.90%. Another example, [9], describes an antenna measuring 24 mm^3 with an 8.57% bandwidth. Furthermore, [10] describes an antenna operating at 2.45 GHz with dimensions measuring 17.1 mm^3, achieving a bandwidth of 9.0%.

This work presents a novel antenna design specifically created for advanced leadless cardiac pacemakers (LCPs). The design addresses the shortcomings of existing models by optimizing both size and bandwidth. With a volume of only 8.33 mm^3, it is the smallest antenna reported in the current literature. In addition to its compact form, it achieves an impressive fractional bandwidth (FBW) of 152.7%, surpassing the capabilities of many existing designs. This extended bandwidth supports faster data rates, enabling the integration of advanced features in future LCPs. Key elements contributing to this performance include strategically designed enlarged slots in the ground plane, a C-shaped slot in the radiating patch, and the use of a via. The main advantages of this antenna are (a) its minimal size, (b) wide bandwidth, (c) resistance to frequency detuning, and (d) its ability to accommodate high channel capacity.

4.2 Methodology

4.2.1 Device Architecture

The specific geometric configuration of the antenna is shown in Figure 4.1, with dimensions of 5.8 mm × 6.0 mm × 0.254 mm, resulting in a total volume of 8.33 mm^3. Wideband performance is achieved by employing reactive loading techniques, while maintaining a compact form [86]. The antenna has a rectangular radiating patch with a central C-shaped slot, as illustrated in Figure 4.1(a). A via, located in the bottom corner with a radius of 0.08 mm, enhances the inductive properties of the antenna. This radius was intentionally kept below 0.1 mm to ensure proper fit and efficiency, considering the 0.2 mm width of the metal loop at the shorting pin. The vias were fabricated using precision laser microdrilling, a method known as Plated Through Hole (PTH), which creates holes that extend through the entire PCB, connecting the top and bottom copper layers. Figure 4.1(b) shows the ground plane

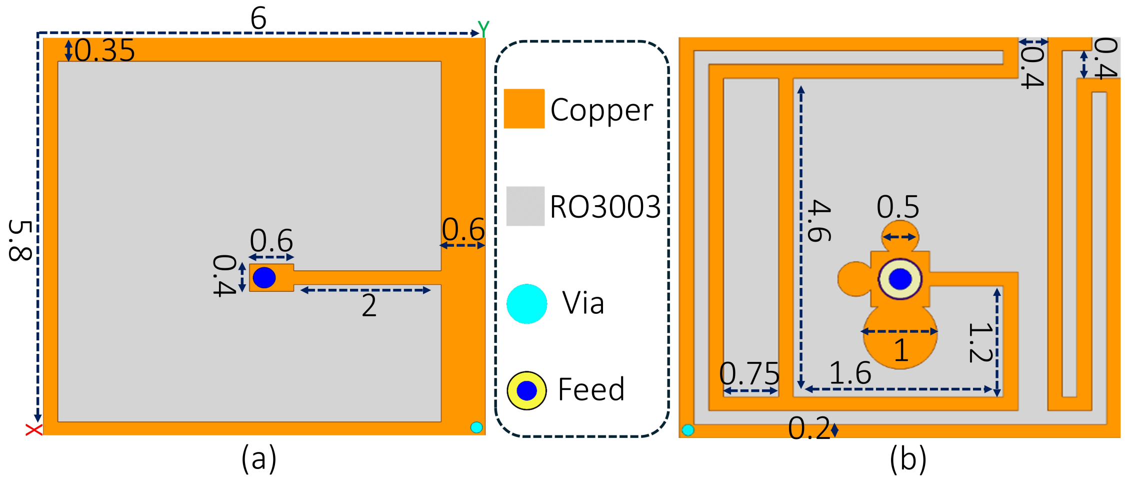

Figure 4.1: (a) shows the front view and (b) the back view of the proposed design, (dimensions in mm).

design, which incorporates enlarged slots and asymmetric circles positioned around the center. The antenna is made of RO3003 material, with a dissipation factor (tan δ) of 0.0013 and a relative permittivity (ϵ_r) of 3, and a combined thickness of 0.254 mm for both the substrate and the superstrate. The antenna is fed by a 50 ohm coaxial feed.

4.2.2 Parametric Study

The development of the proposed antenna is structured in six progressive stages, as depicted in Figure 4.2(a), with the results of the S-parameter (S_{11}) for each stage compared in Figure 4.2(b). The primary objective is to achieve wide bandwidth while maintaining a compact form factor.

Stage 1: The initial configuration includes a rectangular patch antenna with dimensions of 5.8 mm × 6 mm, ensuring compatibility with commercially available leadless cardiac pacemakers like the Micra, which measures 6.7 mm × 25.9 mm. The design incorporates a C-shaped slot in the center of the patch, a continuous ground plane, and a coaxial feed located near the center. This setup produces two mismatched resonance modes at 3.3 GHz and 7.5 GHz, with S_{11} values exceeding -5 dB. The central slot generates multiple current paths, enabling dual-band operation, which will serve as the foundation for merged resonances in subsequent stages [100].

Stage 2: The C-shaped slot on the radiating patch undergoes adjustments, leaving the ground plane unchanged. These changes improve impedance matching, shifting the two operating bands to 3.8 GHz and 9 GHz.

Stage 3: A C-shaped slot is added to the ground plane while retaining the previous configuration of the patch. Simulations reveal that this addition introduces new current paths, improving performance. The lower resonant frequency shifts by approximately 300 MHz, while the higher band shifts by around 2 GHz. A third resonance emerges at 1.7 GHz, with S_{11} reaching -8.9 dB. The introduction of the ground-plane slot increases capacitance, resulting in these frequency shifts and broadening the upper bandwidth range from 5.8 GHz to 9 GHz.

Stage 4: Additional slots are introduced in the central area of the ground plane, strategically placed based on simulation results to improve impedance matching.

This modification shifts the first resonance to 1 GHz and merges the second and third resonances into a single band spanning 1.9 to 5.9 GHz. These slots extend the antenna's effective electrical length, reducing the resonant frequencies. The additional capacitance created by these slots contributes to further downward frequency shifts [8].

Stage 5: Building upon the adjustments in Stage 4, three asymmetric circular features are added to the ground plane to further optimize impedance matching. These features shift the first resonance to 0.92 GHz and adjust the second resonance. Their placement helps refine impedance matching across the operating frequencies.

Stage 6 (Proposed Design): The final stage introduces open-ended slots and a via to enhance reactive loading. Open-ended slots increase capacitive loading, while a via in the bottom corner, with a radius of 0.08 mm, increases inductance. Together, these features extend the antenna's current path, reducing the resonant frequency to 0.67 GHz and improving impedance matching at lower frequencies. Simulations guided the placement of these components in regions with high current density, maximizing their impact on performance. All geometric parameters, including dimensions and positioning, were rigorously optimized through simulation to ensure the highest performance of the proposed antenna.

4.2.3 Simulation and Measurement Setup

The design and analysis of the proposed antenna are carried out using HFSS simulation software. An LCP capsule, with dimensions of 25.9 mm in length and 6.7 mm in diameter, is modeled to house the antenna alongside a simulated battery and electronic components. The capsule is made of ceramic alumina (Al_2O_3), a biocompatible material with a dielectric constant (ε_r) of 9.8 and a wall thickness of 0.2 mm. To emulate the electrical environment of the human heart, a homogeneous phantom (HP) is designed, measuring 120 mm × 80 mm × 60 mm. The phantom's properties are configured to correspond to key biomedical frequencies of interest: 0.915 GHz for ISM applications, 1.4 GHz for telemetry, and 2.45 GHz for wireless communication, as detailed in Table 4.1. To ensure accurate predictions in the far field, a simulation boundary is set at a distance of $\lambda_o/4$ from the antenna edges, fol-

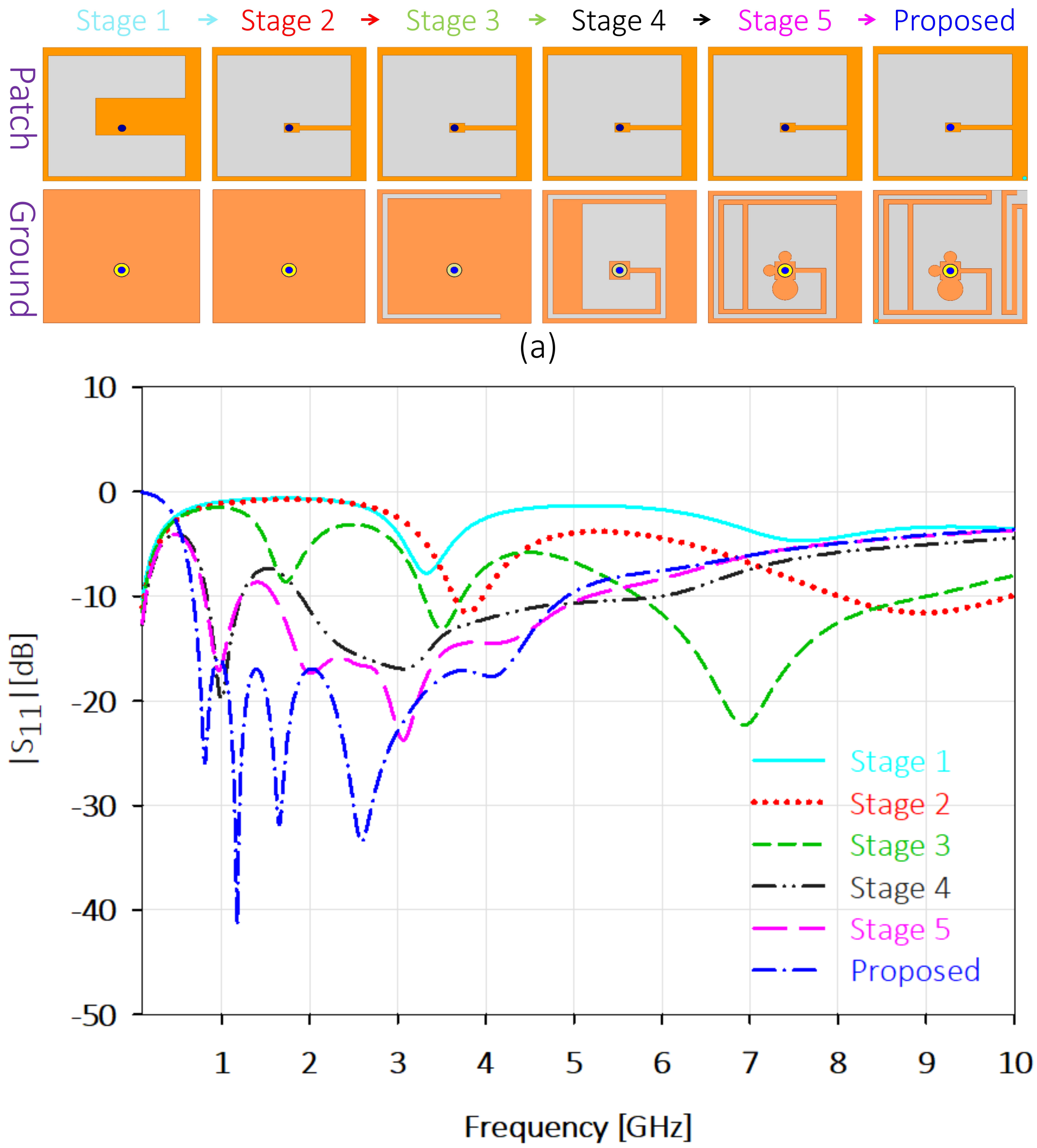

(b)

Figure 4.2: (a) Design evolution of the proposed antenna. (b) $|S_{11}|$ at various stages of the design process.

lowing to the recommendations of [95]. The antenna is embedded at a depth of 30 mm within the phantom for testing, as illustrated in Figure 4.3(a). For a more realistic evaluation, the design is also tested using a human torso model (HTM), where the antenna is placed near the heart region, as shown in Figure 4.3(b). Antenna prototypes are integrated into a 3D printed polylactic acid (PLA) capsule, which includes placeholder components to mimic the electronic setup, as demonstrated in

Table 4.1: Electrical properties at different frequencies

Phantom	Frequency (GHz)	Conductivity (S/m)	Relative permittivity
HP	0.915	1.2	59.7
	1.4	1.5	57.5
	2.45	2.2	54.8

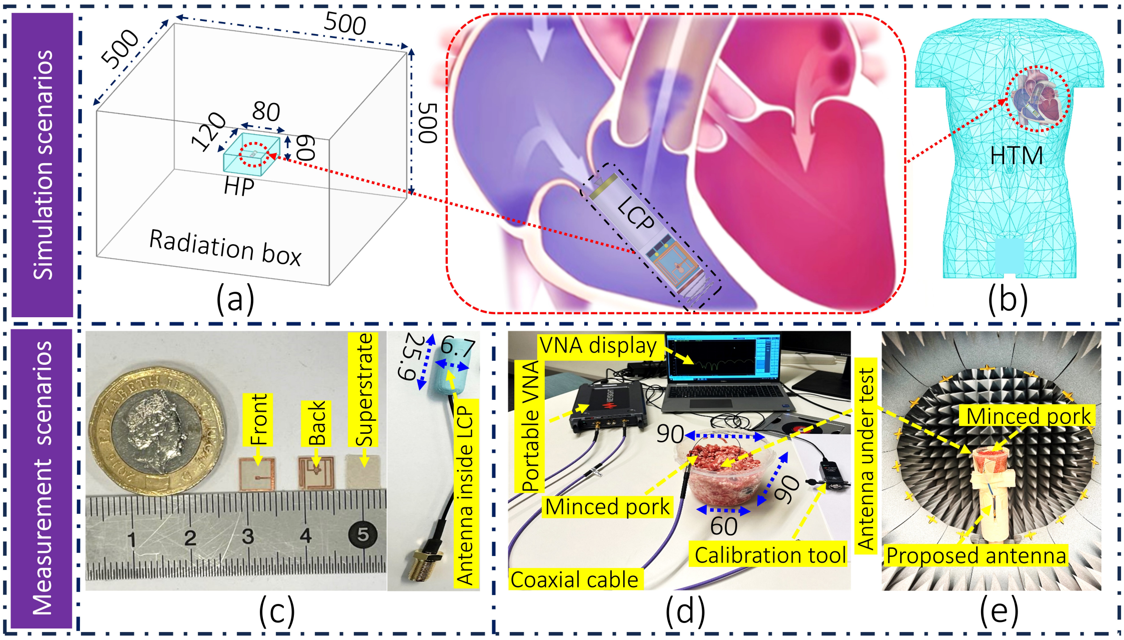

Figure 4.3: (a) Homogeneous phantom, (b) Human torso model (HTM), (c) Fabricated prototypes, (d) S-parameters measurement setup, and (e) Gain measurement setup (dimensions in mm).

Figure 4.3(c). In vitro testing is conducted by placing the antenna within a circular plastic container filled with minced pork meat, with dimensions of 90 mm × 90 mm × 60 mm. The LCP capsule is centrally placed within the phantom to ensure reliable measurement conditions. A Keysight Vector Network Analyzer P9374A is used to assess the reflection coefficient, as shown in Figure 4.3(d). Additional evaluations, including gain measurements, are carried out in a SATIMO anechoic chamber, as depicted in Figure 4.3(e).

4.3 Performance Evaluation and Discussion

4.3.1 Reflection Coefficient Analysis

The S_{11} response of the proposed antenna was evaluated in multiple scenarios, as depicted in Figure 4.4. In each case, the antenna exhibited a broad operational bandwidth while maintaining reliable impedance matching. The recorded bandwidth was 4.33 GHz without the LCP, 4.37 GHz when paired with the LCP, 4.39 GHz in conjunction with the HTM, and 4.45 GHz in real-world tests. Slight differences in the measured S_{11} bandwidth can be attributed to changes in the properties of the surrounding tissue.

In the homogeneous phantom, torso model, and pacemaker-integrated scenarios, the high permittivity of biological tissues reduces the effective wavelength, resulting in a notable downward shift in the resonant frequency. This behavior aligns with established electromagnetic theory and underscores the significant role of dielectric loading in implantable antenna design. By contrast, minced pork tissue exhibits a lower effective permittivity than the simulated tissue models. As a result, a slight upward shift in the resonance frequency is observed in the measurements, reflecting the impact of more realistic dielectric properties on antenna behavior. These results validate the sensitivity of the antenna design to varying dielectric environments and support the effectiveness of the proposed structure across practical biomedical conditions.

4.3.2 Far-field Radiation Characteristics

Figure 4.5 illustrates the omnidirectional radiation patterns of the proposed antenna, with gain measurements taken at 0.915, 1.4, and 2.45 GHz under various conditions. In simulations with a homogeneous phantom (HP) and without LCP, the recorded gains were -31.3 dBi, -25.8 dBi, and -21.9 dBi, respectively. When the LCP was included, the gains decreased slightly to -33 dBi, -27.8 dBi, and -22.7 dBi. In the human torso model (HTM), the gains were reduced to -34.3 dBi, -28.2 dBi, and -23.4 dBi. In real-world measurements, the antenna demonstrated gains of -29.5 dBi, -24.9 dBi, and -19 dBi. It is important to note that the smaller

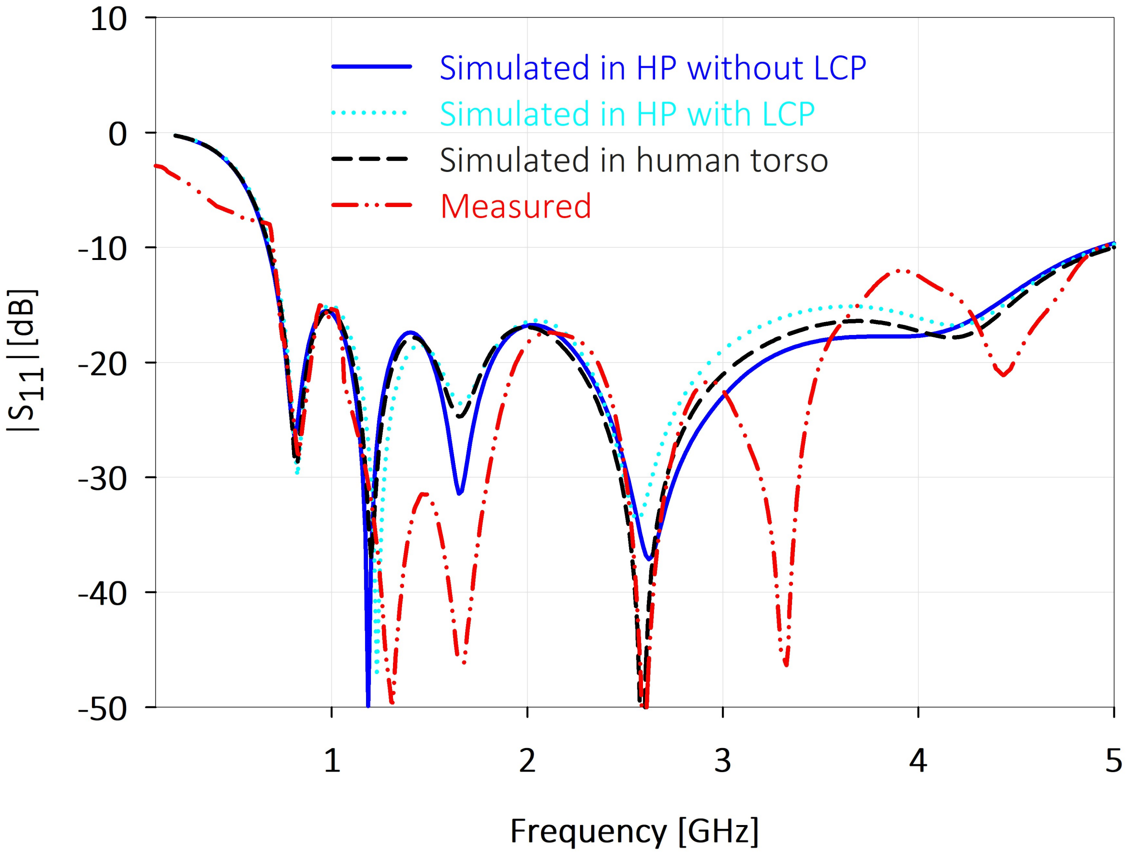

Figure 4.4: Proposed antenna $|S_{11}|$ analysis under varying circumstances.

size of the measurement phantom compared to the simulation model may result in slightly higher gain values. In addition, the depth at which the antenna is implanted significantly affects its performance.

The antenna design incorporates a partial ground plane, which supports wider bandwidth and enables backward radiation—crucial for achieving omnidirectional radiation patterns. This ensures robust communication with external devices, regardless of the antenna's orientation within the body [84, 101].

As expected, the radiation patterns do not exhibit perfectly omnidirectional behavior in either the E- or H-plane, which is theoretically unachievable for practical antennas—especially in compact, implantable scenarios. However, the patterns demonstrate approximately omnidirectional characteristics, which are suitable for biomedical applications where antenna orientation cannot be controlled. It is also worth noting that the radiation plots are displayed using a scale from –60 dB to –30 dB, which compresses the dynamic range and visually smooths out the variations, making the patterns appear more uniform than they actually are.

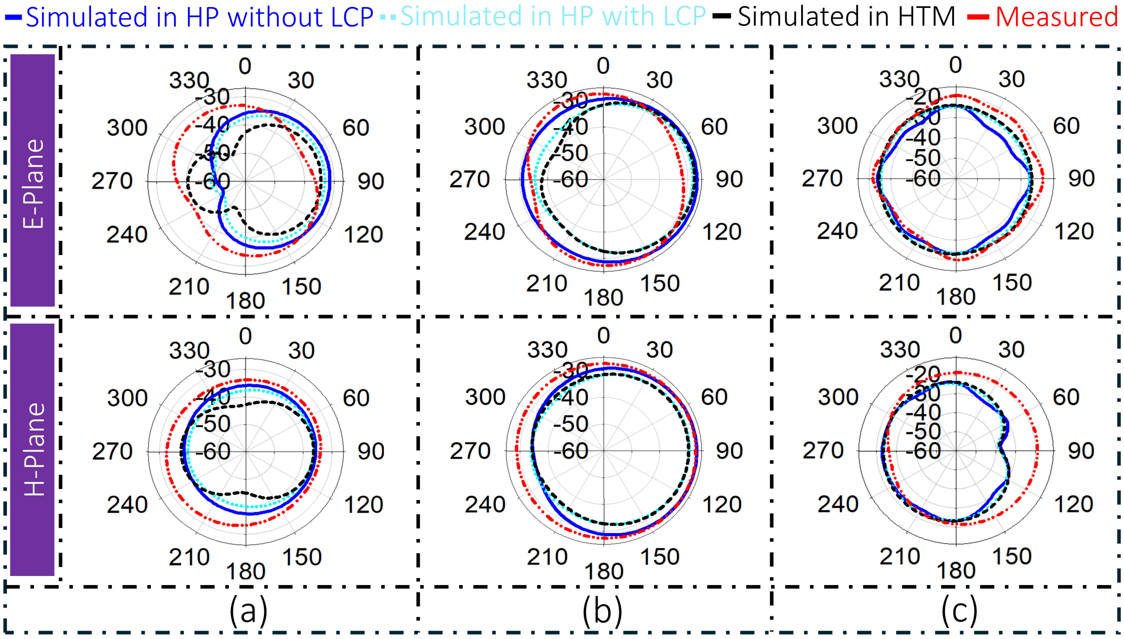

Figure 4.5: Radiation patterns. (a) 0.915 GHz, (b) 1.4 GHz, and (c) 2.45 GHz.

The implantable antenna delivers a wide 4.33 GHz bandwidth with high gain, attributed to several key design techniques.

- **Multi-Resonant Design:** By overlapping multiple resonances, the antenna achieves a wideband response. Through careful optimization, three resonances were closely aligned, resulting in a large bandwidth.

- **Use of Low-Loss Material:** The antenna's substrate and superstrate are made from Roger material RO3003, which has a low loss tangent of 0.0013. This property reduces signal loss within the antenna, improving both its bandwidth and overall efficiency.

- **Patch and Ground Plane Structures:** The antenna's looped design enhances its magnetic properties, making it less sensitive to the lossy dielectric environment. This design choice improves radiation efficiency, which, in turn, maximizes gain (since gain is a product of efficiency and directivity). The looped patch structure increases efficiency across the wide bandwidth, contributing to higher gain.

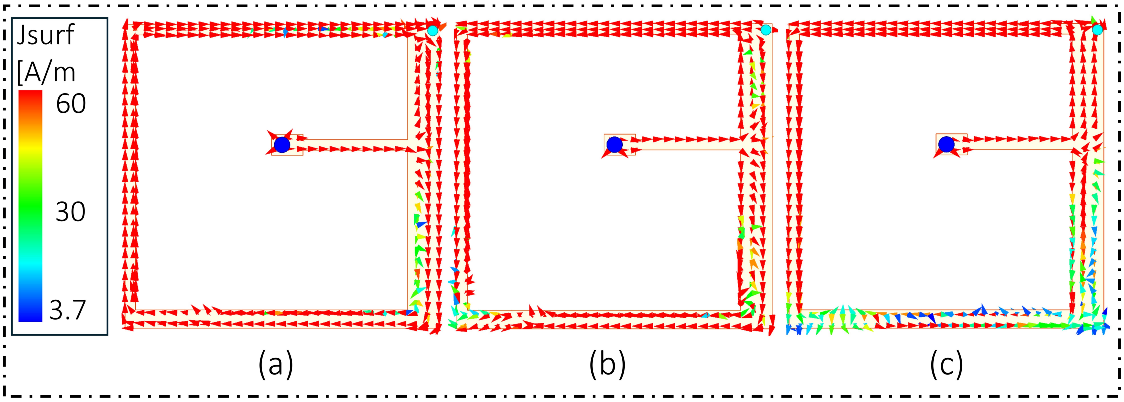

Figure 4.6: Current surface distribution on the radiating patch at (a) 0.915 GHz, (b) 1.4 GHz, and (c) 2.45 GHz.

4.3.3 Current Distribution Analysis

The current distributions across the radiating patch of the proposed antenna at frequencies of 0.915 GHz, 1.4 GHz, and 2.45 GHz are shown in Figure 4.6(a)–(c). For each frequency, the current flows evenly across the radiation field from the antenna port, with the top and left edges of the radiating patch being activated in all bands. However, at 2.45 GHz, as illustrated in Figure 4.6(c), the current is weaker at the right and bottom edges of the patch, indicating a shorter current path at this frequency. In general, the majority of the patch is energized across all frequency bands, and the extended current paths over the radiating patch play a key role in maintaining the antenna's compact size.

4.3.4 Specific Absorption Rate Distribution

To ensure the safety of implantable devices equipped with the proposed antenna, SAR values must remain within safe limits: specifically, 1.6 W/kg for a tissue mass of 1 gram and 2 W/kg for a tissue mass of 10 gram, as outlined in previous research [33]. For comparison with recent studies, the initial evaluation assumes an input power of 1 W. This evaluation includes the determination of the SAR values in the HTM and the calculation of the highest allowable power (HAP). The SAR is given by Equation 4.1:

$$\mathrm{SAR} = \frac{\sigma E^2}{2\rho} \tag{4.1}$$

Table 4.2: SAR and HAP Values

Phantom	Frequency (GHz)	SAR W/kg (1g)	HAP (mW)	SAR W/kg (10g)	HAP (mW)
HTM	0.915	320.4	4.9	32.5	61.5
	1.4	332.8	4.8	34.7	57.6
	2.45	464.1	3.4	49.1	40.7

where σ is the tissue conductivity, E is the electric field strength, and ρ is the mass density of the tissue. Figure 4.7(a–c) present the SAR values at frequencies of 0.915 GHz, 1.4 GHz, and 2.45 GHz. At 2.45 GHz, the maximum SAR value recorded for 1-gram tissue is 464.1 W/kg, corresponding to a HAP of 3.4 mW. For 10 grams of tissue at the same frequency, the highest SAR value is 49.1 W/kg, with an HAP of 40.7 mW. In real-world scenarios, to avoid interference with nearby devices operating within the same frequency band, the input power is typically reduced to 25 µW rather than 1 W [35]. This lower input power standard also helps protect surrounding tissues from potential damage [102]. As a result, the SAR values for this antenna remain within the safe limits of 1.6 W/kg and 2 W/kg, ensuring safety during human body operation. The peak SAR values (0.00801 W/kg at 0.915 GHz, 0.00832 W/kg at 1.4 GHz, and 0.0116 W/kg at 2.45 GHz for 10 grams of tissue) confirm that the antenna is well within the allowable limits when using the typical 25 µW input power for implantable devices. The SAR and HAP data in Table 4.2 further verify that the antenna meets the required safety standards.

4.3.5 Link Budget Calculation

The communication range between the proposed implantable antenna—operating within the human heart—and an external receiver was evaluated using link budget analysis. This analysis calculates the **link margin (LM)**, defined as the difference between the received power (P_r) and the receiver sensitivity (P_s). To ensure reliable communication, a conservative margin of 20 dB was adopted, exceeding the

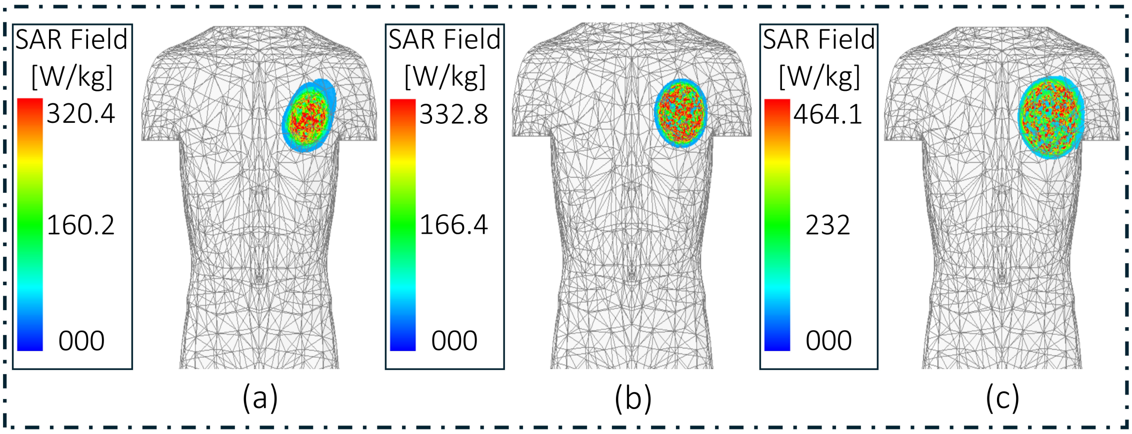

Figure 4.7: SAR within HTM at (a) 0.915 GHz, (b) 1.4 GHz, and (c) 2.45 GHz.

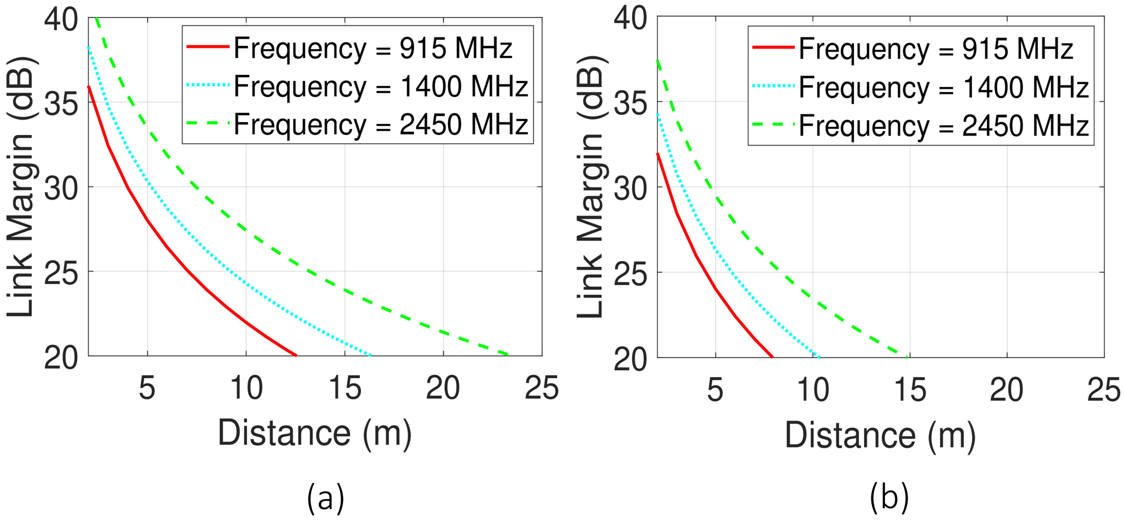

Figure 4.8: Link margin at (a) 10 Mbps and (b) 25 Mbps across various frequency bands.

minimum 0 dB requirement.

Two bit rates were analyzed—**10 Mbps** and **25 Mbps**—to assess how increased data throughput impacts the link margin and communication distance. The calculations follow the theoretical framework established in Section 2.6.1.4.

The resulting communication distances are summarized in Table 4.3. At 10 Mbps, the antenna supports transmission distances of 13 m at 0.915 GHz, 16 m at 1.4 GHz, and 24 m at 2.45 GHz. When the bit rate increases to 25 Mbps, the corresponding ranges decrease to 7 m, 11 m, and 15 m, respectively. As shown in Figure 4.8, this confirms that higher data rates lead to reduced range across all frequencies.

Although higher frequencies like 2.45 GHz are generally associated with increased

Table 4.3: Link Budget Parameters

Varaibales	Parameters	values	Units
Transmission			
P_t	Power	25	µW
f	Frequency	0.915, 1.4, 2.45	GHz
G_t	Gain	-31.3, -25.8, -21.9	dBi
Meduim			
L_p	Path loss	Variable	dB
Reception			
G_r	Gain	2	dBi
N_o	Noise power density	-203	dBm/Hz
T	Temprature	273	Kelvin
K	Boltzmann constant	1.38×10^{-23}	J/K
B_r	Bit rate	10, 25	Mbps
BER	Bit error rate	1×10^{-5}	-
E_b/N_o	Ideal PSK	9.6	dB
G_c	Coding gain	0	dB
G_d	Fixing deterioration	2.5	dB

propagation losses, the proposed antenna exhibits a relatively higher gain at this frequency (-21.9 dBi), compared to -31.3 dBi at 0.915 GHz and -25.8 dBi at 1.4 GHz. This higher gain compensates for the additional loss and contributes to an extended communication range at 2.45 GHz. These results underscore the trade-offs between operating frequency, antenna gain, and data rate in determining system

Table 4.4: Comparison between the Proposed Antenna and Earlier Works

Ref.	Frequency (GHz)	FBW (%)	Gain (dBi)	Size $(\lambda_g)^3$	SAR (W/kg) 1-g	10-g
[98]	2.4	130.9	-12	6.75×10^{-4}	223	-
[1]	0.433	74.1	-23.19	3.02×10^{-1}	177.1	-
[3]	2.45	20.5	-26.4	1.76×10^{-3}	712.1	-
[4]	2.45	88.6	-16.5	1.25×10^{-3}	269	-
[5]	2.45	16.3	-36.8	1.13×10^{-3}	869.9	92.9
[6]	2.45	40.8	-16	1.06×10^{-3}	330.4	39.9
[99]	0.915	19.6	-19.7	6.7×10^{-6}	263.5	53.9
[8]	0.915	84	-30.2	2.66×10^{-5}	796.1	64.1
[2]	2.4	21.5	-33	2×10^{-3}	486	90
[7]	2.4	14.9	-20.75	1.31×10^{-4}	568.2	84.6
[9]	2.45	8.57	-22.8	4.26×10^{-4}	807.3	102.4
[10]	2.45	9	-18.2	3.04×10^{-4}	305	81.7
T.W	1.4	152.7	-25.8	4.40×10^{-6}	332.8	34.7

performance.

As shown in Table 4.4, the performance of the proposed antenna (T.W) is evaluated against several state-of-the-art implantable antenna designs. The comparison includes key performance metrics such as operational frequency, fractional bandwidth (FBW), realized gain, normalized size (in guided wavelength volume, $(\lambda_g)^3$), and Specific Absorption Rate (SAR) values. To ensure a fair and meaningful comparison, it is important to consider designs operating at or near similar frequencies. For example, several antennas in the table operate around the 2.4–2.45 GHz ISM band [3–5], whereas the proposed design operates at 1.4 GHz—a lower frequency that typically requires a physically larger antenna. Despite this, the proposed design maintains an exceptionally small normalized size of $4.40 \times 10^{-6} (\lambda_g)^3$, making it among the most compact antennas in the table, even when compared with higher-frequency counterparts. The proposed antenna also achieves the highest FBW at 152.7%, significantly surpassing other designs such as [4] (88.6%) and [8] (84%). This ultra-wideband capability is especially valuable in biomedical applications, where variations in tissue properties can lead to detuning. A broader bandwidth ensures more robust communication performance in such environments. In terms of SAR, the proposed antenna demonstrates safe performance with a 1-g average SAR of 332.8 W/kg and a 10-g SAR of 34.7 W/kg. These values are lower than or comparable to many other designs operating at similar frequencies, such as [5] and [7], confirming its suitability for safe implantation under regulatory guidelines. Finally, while the peak gain of the proposed antenna (-25.8 dBi) may not be the highest in the table, it is acceptable for deep-tissue communication, particularly considering the lossy environment and compact structure. In implantable applications, gain is often sacrificed to meet miniaturization and safety constraints. In summary, the proposed antenna achieves a superior balance between bandwidth, compactness, and SAR compliance, making it highly competitive for leadless cardiac pacemaker and similar biomedical applications, even when compared against higher-frequency and less space-constrained alternatives.

4.4 Conclusion

A new implantable antenna for leadless pacemakers has been designed, simulated, and validated through experiments, offering a compact size and broad bandwidth. The simulation process was carried out in two phases: initially within a homogeneous phantom and then in a human torso model. The antenna was tested in vitro using minced pork meat to simulate the tissue properties. With a volume of 8.33 $\mathbf{mm^3}$, the antenna achieves a wide bandwidth of 4.33 GHz, corresponding to a fractional bandwidth of 152.7%. Its measured gains are -31.3 dBi at 0.915 GHz, -25.8 dBi at 1.4 GHz, and -21.9 dBi at 2.45 GHz. The recorded SAR values are 320.4

W/kg at 0.915 GHz, 332.8 W/kg at 1.4 GHz and 464.1 W/kg at 2.45 GHz. Link margin calculations show that the antenna can communicate over distances of 13 m at 0.915 GHz, 16 m at 1.4 GHz, and 24 m at 2.45 GHz at a bit rate of 10 Mbps. At 25 Mbps, the ranges decrease to 7 m, 11 m and 15 m, respectively. The consistency between simulated and experimental data emphasizes the antenna's stable impedance matching, wide bandwidth, and reliable radiation patterns, making it an ideal candidate for leadless pacemaker applications.

CHAPTER 5

A Compact Ultra-Wideband MIMO Antenna for Next-Generation Leadless Pacemakers

This chapter presents a two-port ultra-wideband (UWB) multiple-input multiple-output (MIMO) antenna, developed for potential integration into next-generation leadless pacemakers. The antenna utilises a dual rectangular loop design, arranged side by side, to optimise performance for these advanced medical devices. A shared slotted ground plane, substrate, and superstrate are utilised to optimise performance. The antenna achieves a compact size of $12 \times 5.4 \times 0.254\,\mathrm{mm}$ ($16.4\,\mathrm{mm}^3$) through a combination of advanced miniaturization techniques, including the use of conductive vias, metallic rectangular strips, and strategic slotting. A low-permittivity material with a dielectric constant of 2.2 is employed to improve radiation efficiency and support wideband operation, which is crucial for biomedical applications. Each antenna loop is designed with conductive vias and metallic rectangular strips to reduce the antenna's size. To enhance isolation between antenna elements, two rectangular slots are introduced in the center of the ground plane, one for each loop, with a spacing of only 0.8 mm between the elements. This configuration ensures a mutual coupling lower than $-$ 21 dB throughout the operating bandwidth. The antenna achieves an impressive fractional bandwidth (FBW) of 165.2%, covering frequencies from 710 MHz to 7438 MHz. Key performance metrics, including Specific Absorption Rate (SAR), Link Budget, Channel Capacity, and Correlation coefficient, were evaluated. SAR was measured at acceptable levels: 0.042 W/kg at 915 MHz, 0.072 W/kg at 1.4 GHz, 0.083 W/kg at 2450 MHz, and 0.132 W/kg at 5.8 GHz with an input power of 25 µW. At a signal-to-noise ratio (SNR) of 20 dB, the antenna's channel capacity reached 15.04 bps/Hz. A prototype was fabricated to validate the simulation results obtained from HFSS, and experimental testing was carried out using minced pork as a tissue-equivalent medium. The agreement between the simulated and measured results confirms the practicality and suitability of the antenna for next-generation leadless pacemaker applications.

5.1 Introduction

The market for implantable medical devices (IMDs) is projected to grow significantly, reaching \$205.5 billion by 2032, up from \$135 billion in 2023 [103]. These devices have revolutionized healthcare by improving patient care in various ways, including chronic disease management, emergency interventions, and overall well-being [104, 105]. IMDs are used in a range of applications, from cardiac care with pacemakers and defibrillators to pain management through spinal cord stimulators and neurological treatments such as deep brain stimulation. Recent innovations, such as closed-loop neuromodulation and automated insulin delivery systems, have further expanded their capabilities [106–110]. To enable these advanced features, reliable wireless communication is crucial, relying on precisely designed implantable antennas that serve as the vital link between the device and external monitoring systems. These antennas facilitate real-time monitoring and remote care, ensuring timely medical interventions and improved outcomes [111], as shown in Figure 5.1. However, the design of implantable antennas remains a significant technical challenge.

The primary challenge of miniaturisation lies in designing antennas that deliver optimal performance within extremely confined dimensions, as seen in leadless pacemakers and similar applications. For example, the Nanostim pacemaker, with

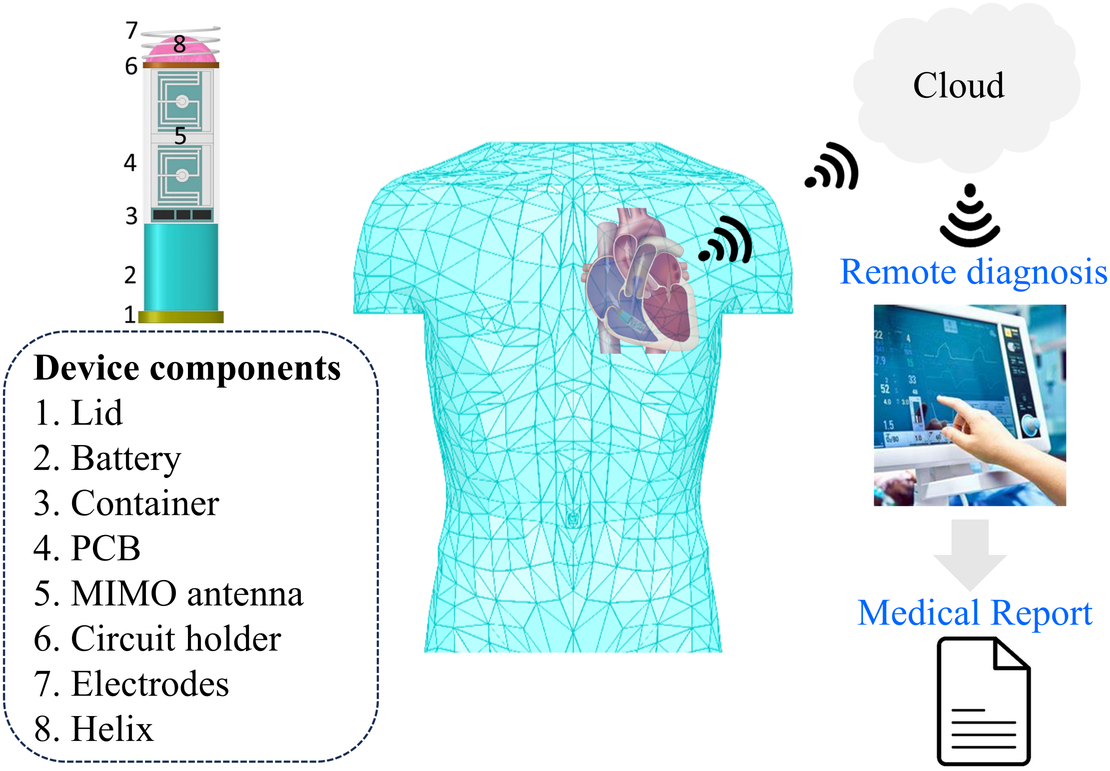

Figure 5.1: Configuration and components of the leadless cardiac pacemaker, including the UWB-MIMO antenna.

a small volume of 1 cm^3, highlights the possibilities of miniaturisation in medical devices. In contrast, the Micra pacemaker is even more compact, at just 0.8 cm^3, illustrating significant progress in reducing device size while maintaining full functionality [112]. Achieving this degree of miniaturisation is essential to ensure patient comfort [69]. The transmission of signals through human tissue, particularly at radio frequencies, presents substantial challenges. At 2.45 GHz, RF signals experience significant attenuation, with the muscle layer contributing to approximately 1 dB/cm of signal loss, a result of the high absorption rate of the tissue and the distinct dielectric characteristics [38,78]. The design of IMDs is further complicated by power constraints, as these devices must operate efficiently within the stringent SAR limits defined by the IEEE C95.1-2005 standard. Another challenge is detuning, where changes in surrounding tissue properties, device movement, and biological variations can affect the resonant frequency of the antenna, ultimately jeopardizing the reliability of communication [85].

To tackle these challenges, several implantable antennas have been designed and developed [1,3–6,8,83]. Despite their success in miniaturisation and tissue compatibility, these designs face inherent limitations due to their Single-Input Single-Output (SISO) configurations. These limitations include data rates of only 5.77 and 5.89 bps/Hz at 20 SNR in recent studies [35, 113], along with poor resistance to multipath distortion in complex tissue environments and limited spectral efficiency [114]. Recent studies highlight that multiple input, multiple output (MIMO) technology offers a promising solution to overcome these limitations, emphasizing the need for more advanced architectures to improve performance in biomedical applications. Research [35,113] indicates that MIMO systems can deliver much higher data rates, achieving 9.97 and 10.2 bps/Hz at 20 SNR. Moreover, MIMO systems are essential in medical implants, as they ensure reliable communication despite the challenging propagation conditions within human tissues. Recent developments in MIMO technology have made significant improvements in overcoming the constraints of single-element systems. For example, [115] shows a compact design measuring 5.35 × 6.2 mm^2. This design achieves significant performance improvements, including a channel capacity of 9.9 bps/Hz (compared to 5.8 bps/Hz for SISO), data rates of up to 120 Mbps, and a high isolation level of 28 dB. Similarly, [116] demonstrated a larger design (18.5 mm × 18.5 mm × 1.27 mm) that improved spectral efficiency, achieved good channel capacity, and increased the transmission rate over an 18.64% bandwidth within the 2.4–2.48 GHz frequency range. Likewise, [117] introduces a MIMO antenna operating at 433 MHz, designed with the same goal of improving data transmission. The antenna incorporates a small magnetic loop with horizontal polarization and a conformal meandered dipole with vertical polarization. However, the limited operating bandwidths of these designs restrict their adaptability in modern medical applications, where the ability to function across multiple frequency bands simultaneously is becoming increasingly necessary for various tasks.

To achieve wider bandwidth, [118] proposed a conformal MIMO loop antenna with a rectangular and meandered line design, offering a 2.2 GHz bandwidth and 20 dB isolation. Significant advances in miniaturisation include a design by [35], which offers compact dimensions of $\pi \times 31.92 \times 0.13\,\mathrm{mm}^3$, achieved through innovative integration of posts and slots. The design also offers a 33.9% fractional bandwidth and a gain of -30 dBi. In [119], an additional size reduction was achieved by adding an H-shaped parasitic patch to the superstrate, leading to dimensions of $9 \times 9 \times 0.508\,\mathrm{mm}^3$, an isolation level exceeding 20 dB, and a fractional bandwidth of 62.6%. The conformal meander technique introduced in [13] resulted in the creation of a 18.5 mm^3 antenna design, achieving a bandwidth of 84.91%, a gain of -30.4 dBi and an isolation level that exceeded 20 dB. In [120], a fractal-based MIMO antenna operating in the 2.4–2.48 GHz ISM band was developed, achieving a gain of -21.3 dBi, an isolation level greater than 20 dB, a fractional bandwidth of 36.76%, and a -10 dB bandwidth of 1.02 GHz.

This research introduces a small two-port ultra-wideband (UWB) MIMO antenna, specifically designed for the next generation of leadless cardiac pacemakers (LCPs). For deeply implanted devices, such as LCPs, maintaining reliable communication is essential. This requires overcoming challenges such as signal attenuation due to tissue interference, multipath interference, and frequency detuning caused by diverse environments within the body. With a channel capacity of 15.04 bits/s/Hz at an SNR of 20 dB, the proposed two-element UWB-MIMO antenna design delivers reliable long-term performance, effectively overcoming the constraints typically associated with conventional implantable antennas. The design offers superior data rates, a reliable communication link and wide bandwidth capabilities, significantly outpacing the performance of existing top-tier implantable antennas [13,35,118–120]. Although antennas with larger bandwidths and higher data rates tend to consume more energy, the leadless pacemaker addresses this issue by employing intermittent data transmission, activating only when necessary. This method strikes a balance between high data rates and low power consumption, ensuring its suitability for long-term use. In addition, digital CMOS pulse generator techniques are utilized to further minimize power consumption in UWB applications [121]. Future advancements in wireless power transfer may allow the continuous recharging of implant batteries, thereby prolonging the operational lifespan of the pacemaker. The compact design of the antenna utilizes low-permittivity materials ($\varepsilon_r = 2.2$) for both the substrate and superstrate to enhance bandwidth. Size reduction is achieved through techniques such as optimized rectangular loop elements, via-based inductive loading, and strategically placed U-shaped and open-ended slots in the ground plane. These methods enable effective miniaturization, achieving a compact form factor of $12 \times 5.4 \times 0.254\,\text{mm}^3$ (16.4 mm^3), along with impedance matching and bandwidth enhancement. Mutual coupling between elements is minimized by incorporating a 0.8 mm gap between the rectangular loop antenna elements and utilizing optimized ground-plane slots, including two rectangular slots, one for each loop antenna. The design achieves an isolation greater than 21 dB over the full operating bandwidth, which exceeds the 15 dB threshold necessary for optimal MIMO performance [122]. In addition, the antenna demonstrates peak gains of -34.7 dBi at 0.915 GHz, -28.4 dBi at 1.4 GHz, -23.3 dBi at 2.45 GHz, and -20.1 dBi at 5.8 GHz. The specific absorption rate (SAR) values are 0.042 W/kg at 915 MHz, 0.072 W/kg at 1.4 GHz, 0.083 W/kg at 2.45 GHz and 0.132 W/kg at 5.8 GHz, all with an input power of 25 μW, which remain well below the safety limits outlined in [123]. Featuring high gain, wide bandwidth, low SAR, and outstanding 2x1 UWB-MIMO channel performance, this antenna stands out as an excellent candidate for next-generation leadless pacemakers.

5.2 Methodology

Figure 5.2 illustrates the proposed implantable UWB-MIMO antenna, which consists of a superstrate, two rectangular loop antenna elements, a substrate, and a shared ground plane. To maintain consistent signal interpretation and stable system performance, it is crucial to use a single shared ground plane. The use of multiple ground planes can result in voltage irregularities, which can cause noise, signal distortion, and instability, especially in MIMO systems [124]. Throughout the bandwidth, the design maintains a mutual coupling value of $-21\,\text{dB}$, ensuring strong isolation between the elements. Rogers RO5880 material, with a relative permittivity of $\varepsilon_r = 2.2$, is used for both the substrate and the superstrate. The common ground plane is designed with multiple U-shaped and open-ended slots to enhance bandwidth and improve impedance matching.

To achieve miniaturization, metallic vias connect the rectangular loop antenna

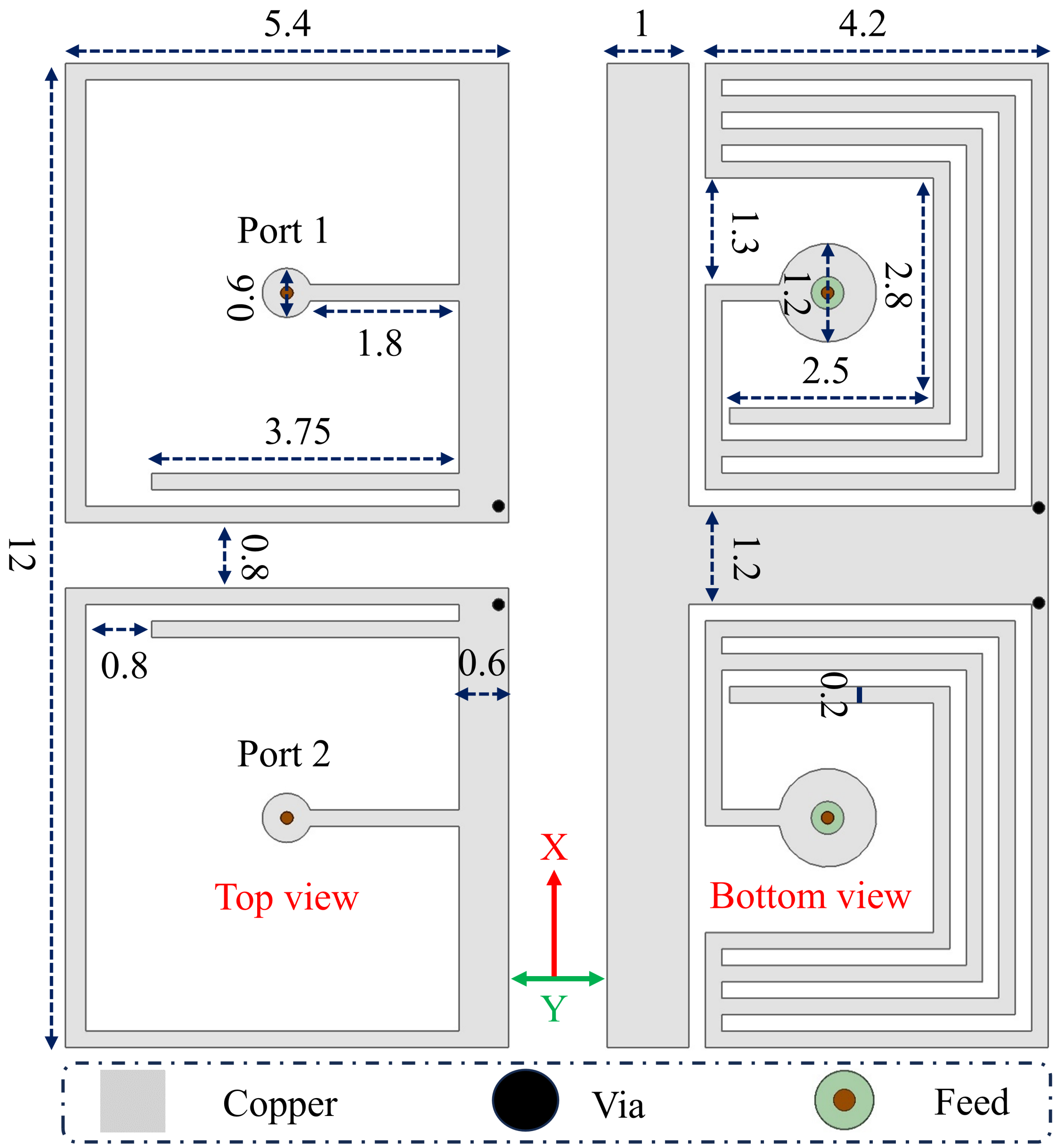

Figure 5.2: Configuration of the proposed 2x1 UWB-MIMO antenna (units = mm).

elements to the ground plane, resulting in a compact design with dimensions of $12 \times 5.4 \times 0.25$ mm^3. Each antenna element is connected through a coaxial cable with a characteristic impedance of $Z_0 = 50\,\Omega$. The cable has an inner conductor with a diameter of 0.18 mm, a Teflon insulating layer with a relative permittivity (ε_r) of 2.1, and an outer conductor with a diameter of 0.6 mm. The characteristic impedance Z_0 of a coaxial cable is derived using Equation 5.1.

$$Z_0 = \frac{60}{\sqrt{\epsilon_r}} \ln\left(\frac{D}{d}\right) \tag{5.1}$$

The characteristic impedance Z_0 is influenced by the coaxial cable's structure, where ε_r represents the relative permittivity of the insulating layer, D denotes the outer conductor's diameter, and d specifies the inner conductor's diameter. To enhance compactness, the design employs ultra-thin substrate and superstrate layers, each with a thickness of 0.127 mm. Biocompatibility, a critical requirement for medical implants, is ensured by enclosing the antenna within a PLA capsule (polylactic acid), a material with a relative permittivity of $\varepsilon_r = 3.1$. The capsule dimensions—5.5 mm in diameter and 24 mm in length—accommodate the antenna along with essential components, including a printed circuit board (PCB) for interconnections and a battery. All components are securely housed within a robust protective shell, as illustrated in Figure 5.1. This encapsulation effectively isolates the device from surrounding tissues, while adhering to stringent biocompatibility standards, ensuring safe and reliable operation within the human body.

5.2.1 Simulation Setup

Simulating implantable antennas demands a specialized setup due to their operation within complex biological tissues, which differs significantly from free-space antenna scenarios. Initial simulations were carried out using HFSS within a phantom model with dimensions of $100 \times 100 \times 100\,\text{mm}^3$. The chosen size provides a sufficiently large volume to mimic the electromagnetic properties of the human heart surrounding the implanted antenna. This helps replicate the propagation and attenuation of the signal realistically. The antenna was designed to fit inside a capsule shell made of PLA, which has a thickness of 0.2 mm. The capsule was placed at a depth of 50 mm to mimic typical implantation depths for leadless pacemakers, which range between 40 and 60 mm, as described in clinical studies [125]. The capsule shell's 0.2 mm thickness adheres to medical implant standards by balancing the transmission of the RF signal with structural integrity. Thinner shells could enhance signal transmission but compromise durability, whereas thicker shells may reduce signal strength [126]. To obtain reliable far-field simulation results, a radiation box measuring $500 \times 500 \times 500\,\text{mm}^3$ was placed around the antenna. The box was sized to ensure that the distance from the antenna to the box walls exceeded $\lambda_0/4$ at the res-

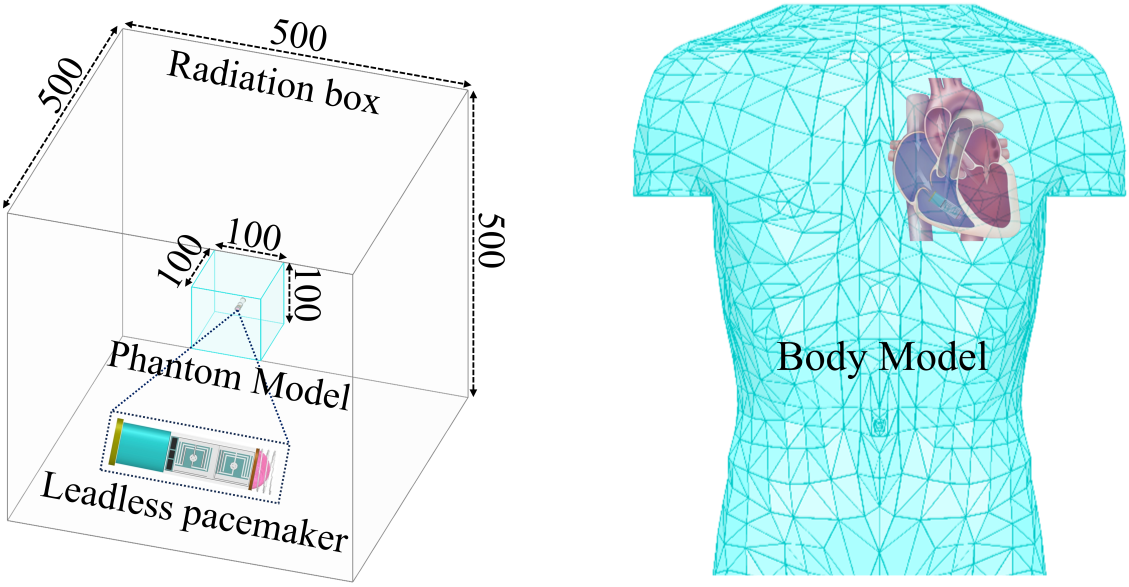

(a) Phantom Model (b) Body Model

Figure 5.3: Simulation setups of the 2x1 UWB-MIMO antenna: (a) Phantom Model and (b) Body Model (units = mm).

Table 5.1: Dielectric properties of the heart tissue at various frequencies

Phantom type	Frequency (GHz)	Conductivity (S/m)	Relative permittivity
Phantom Model	0.915	1.2378	59.796
	1.4	1.5132	57.538
	2.45	2.2561	54.814
	5.8	5.8622	48.949

onant frequency of 915 MHz, preventing boundary reflections from interfering with the simulation, as shown in Figure 5.3(a). The electrical properties of the Phantom Model were carefully adjusted to mimic the characteristics of heart tissue, with specific permittivity and conductivity values at different frequencies, as detailed in Table 5.1. The UWB-MIMO antenna uses a thin Rogers RO5880 substrate with a relative permittivity (ε_r) of 2.2, a loss tangent ($\tan\delta$) of 0.0022, and a thickness of 0.127 mm. Following the initial simulation, the capsule was repositioned within the Body Model to more accurately reflect the position of the human heart, as shown in Figure 5.3(b).

5.2.2 Design Process

Designing an antenna for implantation in the human body involves addressing several factors that influence its performance, requiring a multi-stage approach to achieve optimal outcomes. Throughout this iterative design process, key objectives are prioritized: (1) achieving a compact form factor, (2) enhancing impedance matching, (3) ensuring UWB-MIMO functionality, and (4) maintaining excellent isolation. To achieve these objectives, the rectangular loop antenna is developed through four distinct designs, as shown in Figure 5.4(a), with the corresponding results presented in Figure 5.4(b) and Figure 5.4(c).

Design I (Initial): The size of the rectangular loop antenna element was determined based on the resonant frequency formula provided in Equation 5.2. This design ensures that the antenna fits within the compact capsule dimensions of 5.5 mm × 24 mm, which are suitable for modern leadless pacemaker devices.

$$f_r = \frac{C}{\sqrt{\varepsilon_r} \cdot \text{Perimeter of the loop}} \tag{5.2}$$

where f_r denotes the resonant frequency, C is the speed of light in a vacuum, ε_r represents the relative permittivity of the substrate, and the perimeter of the loop refers to the effective length of the rectangular loop, considering any modifications for slots or structural features. The limited size of the leadless pacemaker capsule presents a major challenge in achieving adequate isolation and minimizing mutual coupling between antennas in MIMO system applications. Traditional designs for spatial diversity typically require antenna separations of at least half the wavelength [127], which is impractical within the small dimensions of a pacemaker capsule. To address this challenge, a parametric study was conducted to determine the optimal edge-to-edge separation between the two rectangular loop elements. The study revealed that a 0.8 mm separation strikes an ideal balance between performance and compactness. While decreasing the separation increases mutual coupling due to enhanced near-field interactions [128], the 0.8 mm spacing provides sufficient isolation, as verified through both simulations and experimental tests. To introduce capacitance and inductive loading, rectangular loop elements were integrated with a complete ground-plane configuration. This modification altered the electric-field distribution on the loop and created multiple resonant points based on coupled-mode theory. This approach resulted in a broader bandwidth and more precise control over resonant frequencies, as demonstrated in [129]. As a result, the design exhibited two mismatched resonances at 2.5 GHz and 4.5 GHz, but achieved a well-matched resonance at 8 GHz with excellent impedance matching and a bandwidth exceeding 4 GHz. In addition, an inductive shorting pin was added to increase inductance, aiding in miniaturizing the antenna. More specifically, the shorting pin creates a voltage-null boundary condition, causing the antenna to resonate at a longer wavelength [130]. By positioning the shorting pin at the edge, far from the feed point, its effect on the loop's impedance is minimized. This is because the impedance of the loop depends on its geometry and the feeding point, where the voltage is highest. Mutual coupling in this design is kept very low, below -33 dB, primarily due to the poor impedance matching at lower frequencies. Although better matching is achieved at higher frequencies, they are more susceptible to surrounding tissue and suffer greater signal attenuation.

Design II: The rectangular loop radiating elements from the previous design were retained, with the addition of two open-ended rectangular slots in the ground plane. These slots extend the effective length of the current path, thereby reducing the resonance frequency. Consequently, the three resonances observed in the initial design shifted to 1.8, 3.2, and 5.8 GHz. This modification also led to a significant increase in mutual coupling to -16.2 dB, primarily due to improved impedance matching.

Design III: In this step, the rectangular loop elements from the previous design were retained, with the addition of multiple U-shaped slots in the ground plane to enhance bandwidth and improve impedance matching. This modification increases the antenna's electrical length, resulting in a further reduction of the resonant frequencies from 1.8 GHz and 3.2 GHz to 0.9 GHz and 2.5 GHz, respectively. The introduction of multi-loop slots also expands the bandwidth and optimizes impedance matching by generating multiple resonance frequencies, yielding an impedance bandwidth that spans from 2 GHz to 9.5 GHz [131]. Furthermore, this design achieves

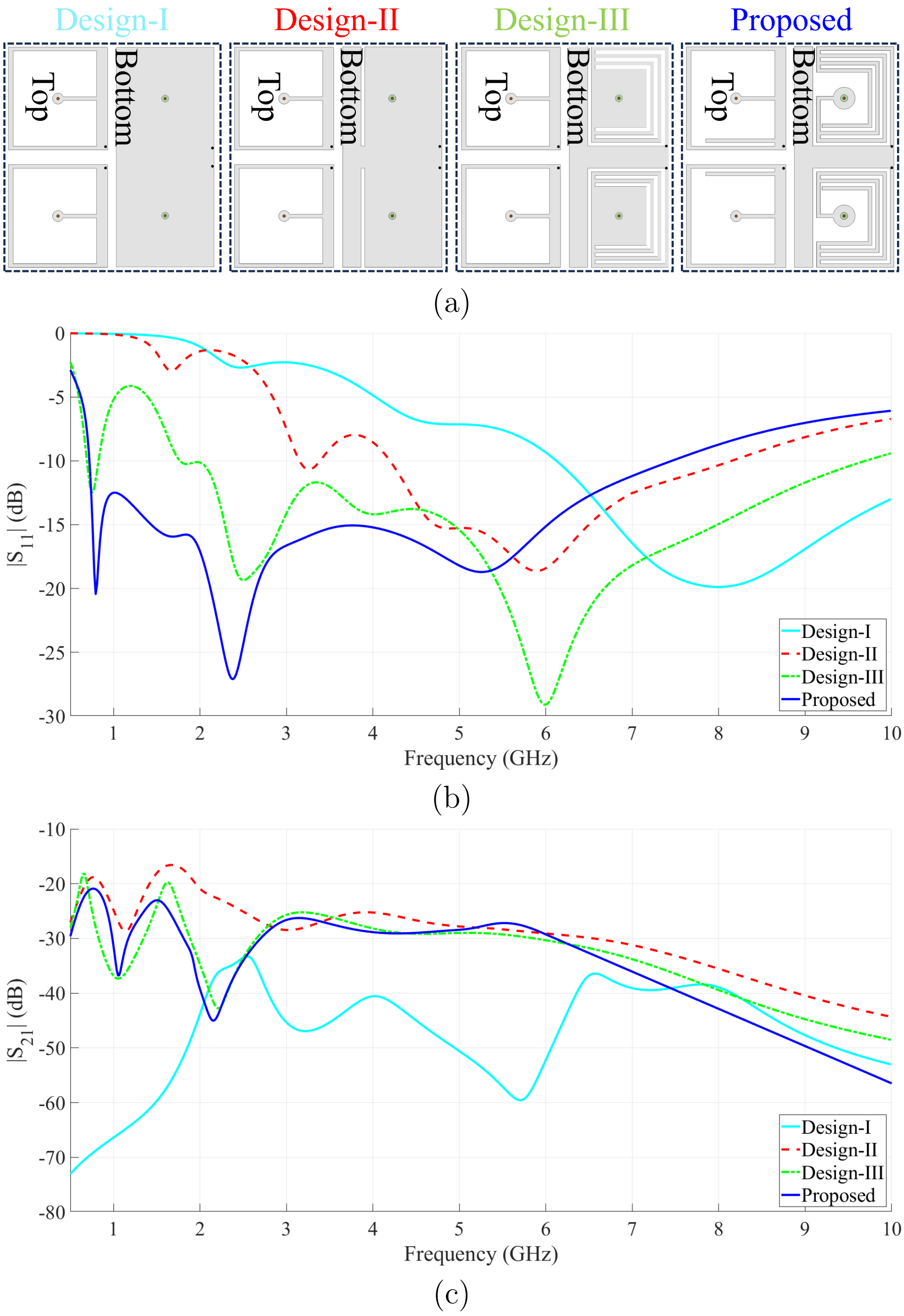

Figure 5.4: (a) Evolution of the proposed 2x1 UWB-MIMO antenna design; (b) S-parameter analysis ($|S_{11}|$); and (c) Mutual coupling analysis (S_{21}).

a reduction in mutual coupling at -17.2 dB. The final shape and dimensions of the slots were carefully optimized through both theoretical calculations and simulation-based refinements.

Design IV (Proposed): In this design, a metallic rectangular strip is incorporated into each of the rectangular loop elements. This addition reduces the resonance frequency by effectively increasing the electrical length of the antenna without physically extending the loop. The strip length is carefully chosen to fine-tune the resonance frequencies; as the strip length increases, the resonance frequency decreases. However, adding metallic strips also reduces the isolation between the two radiating elements. This is due to an increase in current density at specific points along the loop, which enhances the electromagnetic coupling between the elements. To counteract this effect, two rectangular slots were added around the center of the ground plane, beneath each loop—resulting in a mutual coupling level of less than -21 dB throughout the bandwidth.

5.2.3 Circuit Model

The proposed antenna features closely spaced resonances and overlapping frequency bands, each represented by a parallel RLC circuit. In wideband antenna systems, multiple parallel RLC circuits are connected in series to model adjacent frequency bands. To conduct a more thorough analysis, a circuit model was developed using Advanced Design System (ADS) software, following the degenerate Foster canonical form—a standard approach for analyzing ultra-wideband (UWB) antennas [132–134]. The optimization of the circuit model, which involved setting initial conditions and aligning electromagnetic (EM) simulations with ADS circuit simulations, resulted in the equivalent circuit shown in Figure 5.5(a). Both antenna elements (Antenna 1 and Antenna 2) share the same equivalent circuit configuration. In this model, the inductance (L_f) and capacitance (C_f) represent the primary resonance of the antenna, while higher-frequency resonances are modeled by series-connected tank circuits, with resistors accounting for the radiation resistance. A strong correlation between the S-parameter (S_{11}) obtained from both the EM and circuit simulations is evident, as shown in Figure 5.5(b). Any minor discrepancies between the curves can be attributed to the complex ground plane, which is modeled as a parallel inductor and capacitor in series with the resonance tank circuits. Furthermore, the coupling between the two antennas is represented using a combination of series and parallel RLC circuits. The S_{21} parameter was used as the optimization target, resulting in excellent agreement between the simulated and measured coupling data, as demonstrated in Figure 5.5(c). The component values

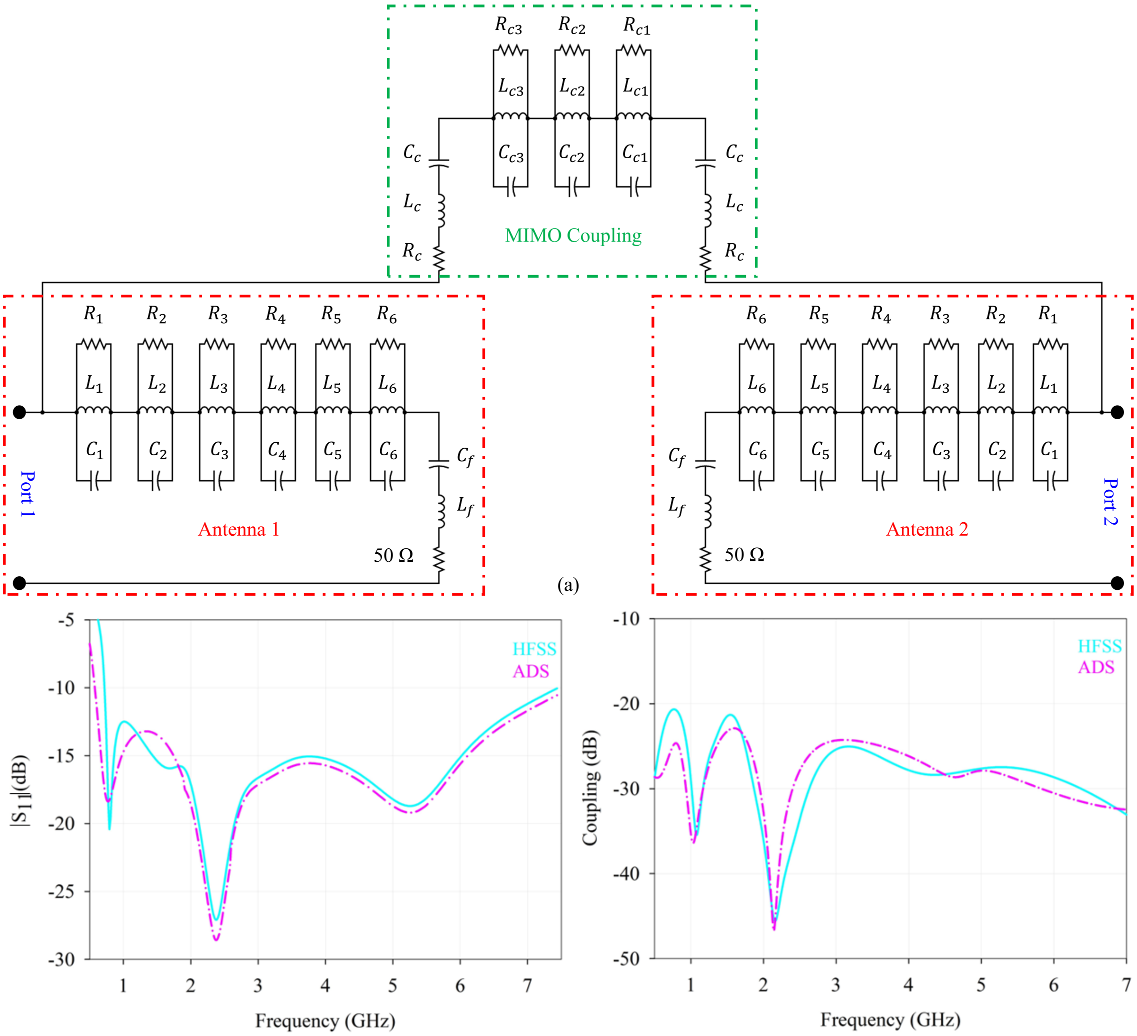

(b) (c)

Figure 5.5: (a) Proposed equivalent circuit model for the 2x1 UWB-MIMO antenna; (b) Comparison of the S_{11} parameter; and (c) comparison of the S_{21} parameter, both simulated in HFSS and ADS.

for the equivalent circuit are listed in Table 5.2.

5.2.4 Fabrication and Measurements Environment

To validate the simulation results, a 2×1 UWB-MIMO antenna was fabricated using the same Rogers substrate and superstrate as in the simulations. The fabricated antenna prototype is shown in Figure 5.6(a). The capsule shell of the leadless pacemaker was manufactured using 3D printing technology, ensuring precision in dimensions and structural integrity. The assembled device was encapsulated in epoxy to evaluate key performance parameters, including return loss (S_{11}), trans-

Table 5.2: Values of electronic components used in the 2x1 UWB-MIMO circuit. (Units: $R = \Omega$, $L = nH$, $C = pF$)

Component	L_f	C_f	R_1	L_1	C_1	R_2	L_2	C_2
Value	1.67	50	6.11	95.5	33.3	22.3	100.8	17.81
Component	R_3	L_3	C_3	R_4	L_4	C_4	R_5	L_5
Value	53.3	2.2	0.55	86.5	47.7	46.6	50.6	9.8
Component	C_5	R_6	L_6	C_6	R_c	L_c	C_c	R_{c1}
Value	2.5	20.6	1.97	5.9	178	13.44	0.6	1860
Component	L_{c1}	C_{c1}	R_{c2}	L_{c2}	C_{c2}	R_{c3}	L_{c3}	C_{c3}
Value	34.33	0.7	205	1	1.14	11.05	0.6	0.5

mission coefficient (S_{21}), radiation patterns, and gain. The parameters S_{11} and S_{21} of the fabricated antenna were measured in a medium based on biological tissue, specifically minced pork meat, at a depth of 50 mm using a Keysight P5004 Vector Network Analyzer (VNA). High-quality cables ensured reliable and accurate connections between the antenna and the VNA ports, as illustrated in Figure 5.6(b). Before measurements, the VNA was calibrated using open, short, and load standards to compensate for systematic errors such as cable losses and connector mismatches. After calibration, the VNA was configured to operate within the desired frequency range. For radiation pattern measurements, a SATIMO anechoic chamber was used, as shown in Figure 5.6(c). The experimental setup included a signal generator connected to a high-gain horn antenna serving as the transmitting antenna (Tx), while the implantable MIMO antenna acted as the receiving antenna (Rx). The horn antenna, measuring 49 cm in width, 40 cm in depth, and 32 cm in height, transmitted the signal. One port of the implantable antenna was connected to a spectrum analyzer, while the second port was terminated with a $50\,\Omega$ load. A distance of 3 m was maintained between the horn antenna and the implantable antenna to ensure accurate power measurements. The implantable antenna was rotated in 10° increments to record the received power, enabling a comprehensive analysis of its

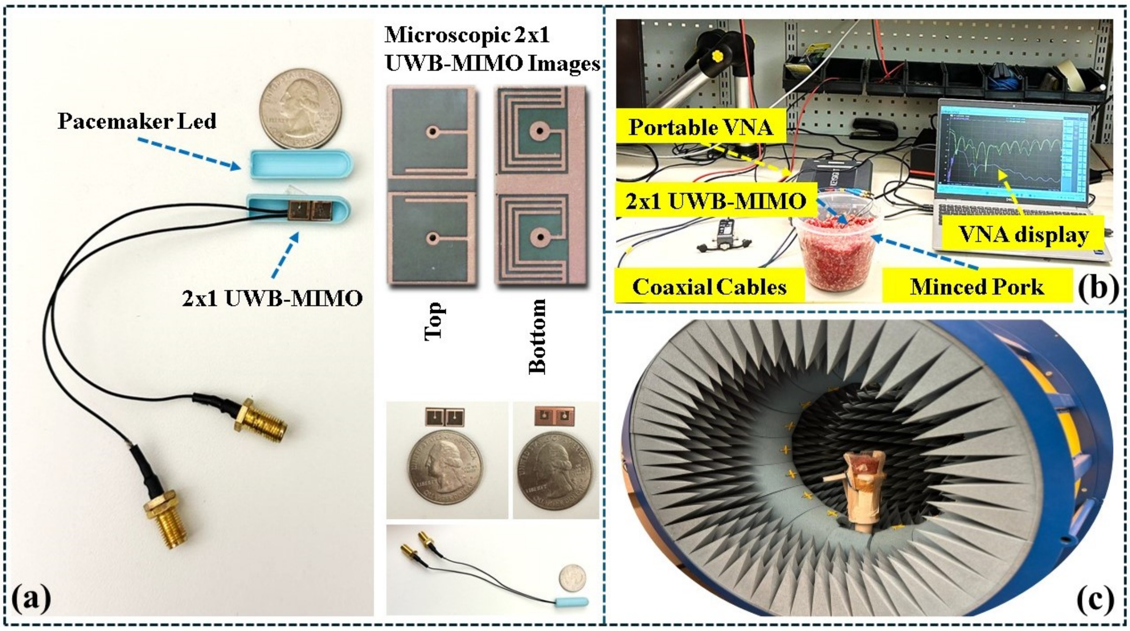

Figure 5.6: The 2×1 UWB-MIMO antenna was fabricated and tested, including (a) the fabricated antenna prototype, (b) the measurement setup for S-parameters, and (c) the measurement setup for radiation patterns.

radiation performance in different orientations.

5.3 Findings and Discussion

5.3.1 S-parameter Characteristics

A comparison between the simulated and measured S-parameters is presented in Figure 5.7. Due to the symmetry of the 2×1 UWB-MIMO antenna design, only the reflection coefficient of one element is shown. Both simulated and measured results exhibit strong agreement, validating the antenna's ultra-wideband performance. Specifically, the simulated S_{11} results indicate an operational frequency range from 710 MHz to 7483 MHz, corresponding to a fractional bandwidth (FBW) of 165.12%. The measured S_{11} results demonstrate a reflection coefficient below $-10\,\text{dB}$ over an even wider bandwidth. Furthermore, the S_{21} parameter quantifies the signal leakage between antenna elements, serving as an indicator of isolation performance. Achieving low S_{21} values is particularly challenging in compact implantable designs due to the close proximity of antenna elements, which inherently increases coupling. The simulated S_{21} results show strong isolation, with a mutual

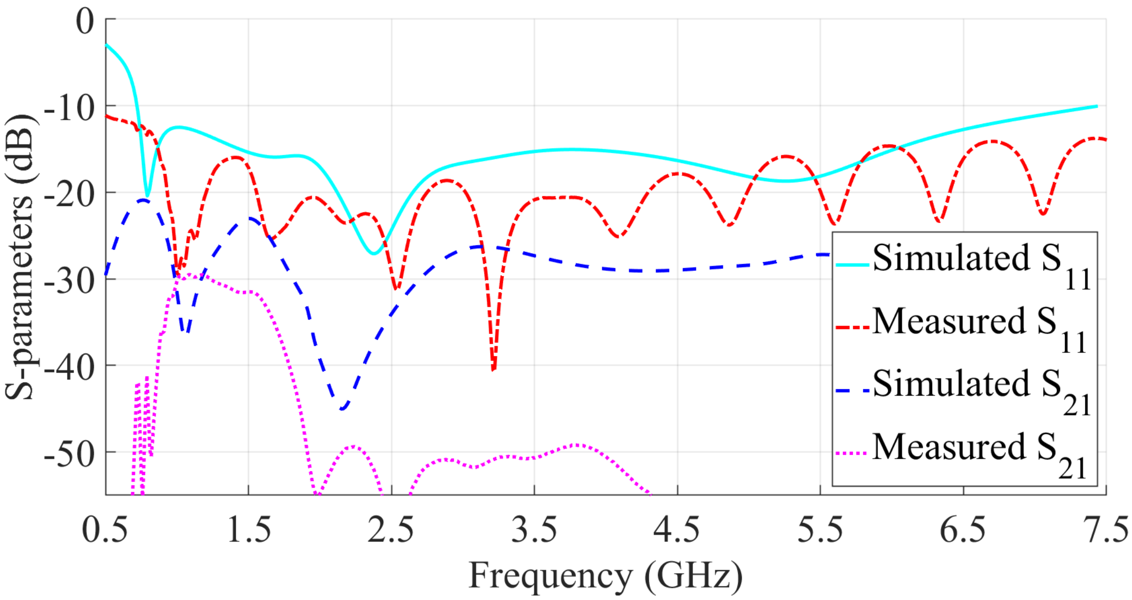

Figure 5.7: Comparison of the S-parameters from simulation and measurement for the 2x1 UWB-MIMO antenna.

coupling value of -21 dB across the entire bandwidth. In contrast, the measured S_{21} values demonstrate even better isolation, with a mutual coupling value of -29 dB. This high isolation ensures that each antenna element operates independently with minimal interference, an essential requirement for reliable MIMO performance. Reduced mutual coupling enhances antenna efficiency in high-data-rate applications by minimizing cross-coupling and signal degradation, ultimately ensuring optimal communication quality for medical telemetry. The improved mutual coupling observed in the measured S_{21} values (-29 dB) compared to the simulated results (-21 dB) can be attributed to slight variations in the fabrication and material properties. These unintentional factors may have contributed to enhanced isolation in the measured prototype, highlighting the robustness of the antenna design. Differences between the simulated and measured results may also arise from factors such as manual assembly and integration issues, potential misalignment of the antennas, and inconsistencies in the soldering of the coaxial cables. Additionally, variations in dielectric properties between the human model used in the simulations and the minced pork used in measurements may contribute to the discrepancies. Nevertheless, the overall performance remains consistent, demonstrating the antenna's ultra-wideband characteristics and confirming its suitability for leadless pacemaker applications.

5.3.2 Radiation Patterns

The performance of any wireless device is heavily dependent on its radiation patterns. For a leadless pacemaker implanted in the heart, an omnidirectional radiation pattern is crucial [135]. The ground plane configuration of our proposed antenna facilitates this omnidirectional radiation pattern, as shown in Figure 5.8. This pattern ensures effective signal reception regardless of the orientation or position of external devices, which is essential for reliable communication between implantable antennas and these devices. Although reducing the ground-plane area may increase back radiation, our analysis indicates that this modification does not significantly compromise the antenna's performance or safety. The individual elements of the MIMO antenna exhibit peak gain values at various frequencies: -34.7 dBi at 0.915 GHz, -28.4 dBi at 1.4 GHz, -23.3 dBi at 2.45 GHz, and -20.1 dBi at 5.8 GHz. Figure 5.8 presents the simulated and measured radiation patterns of the proposed antennas in both the H-plane ($\theta = 90°$) and the E-plane ($\phi = 0°$). A strong correlation exists between the simulations and the measurements at all frequencies; however, the measured gain is slightly higher, with values of -33.2 dBi, -27.6 dBi, -22.4 dBi and -19.4 dBi at 0.915 GHz, 1.4 GHz, 2.45 GHz and 5.8 GHz, respectively. This discrepancy may be attributed to the smaller minced pork container used during the measurements. The radiation pattern remains omnidirectional across all frequencies but begins to show distortion at 2.45 GHz due to a slight increase in gain in the E and H planes between 90° and 180°, leading to a less uniform distribution. This distortion may result from resonance effects and the current distribution over the antenna surface, which cause the geometry to favor certain directions at higher frequencies. At 5.8 GHz, the radiation pattern exhibits variations of up to 5 dB, resulting in a zigzag pattern in the omnidirectional profile. This behavior is likely due to the increased sensitivity of higher frequencies to design imperfections and edge diffraction, especially compared to lower frequencies, which maintain a smooth omnidirectional pattern. Additionally, increased propagation losses and phase shifts may also contribute to these irregularities.

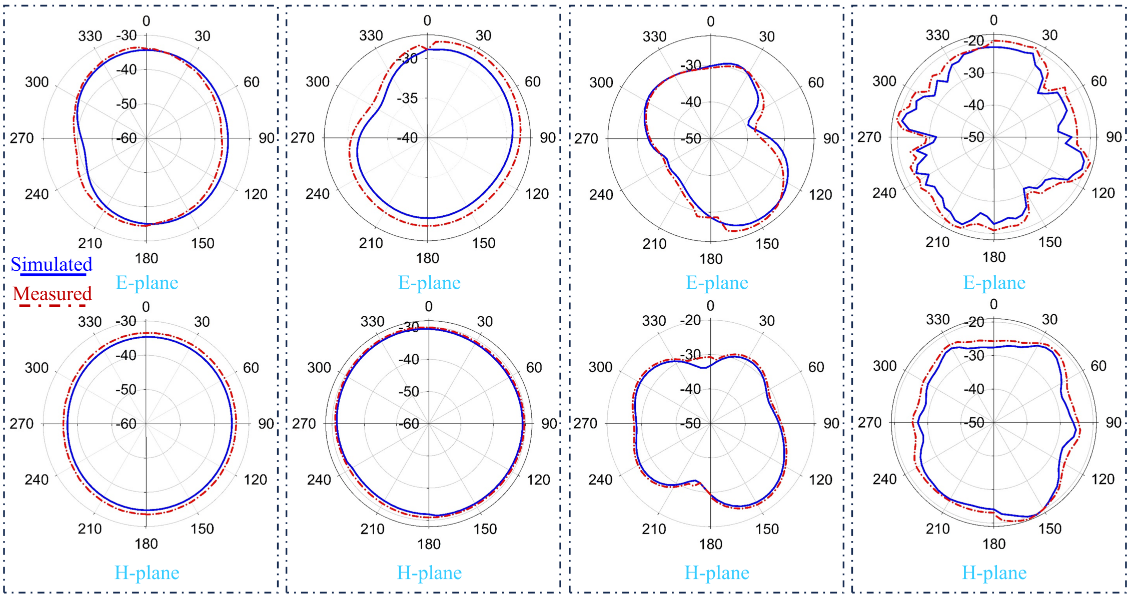

(a) (b) (c) (d)

Figure 5.8: Radiation patterns of the individual elements of the 2x1 UWB-MIMO antenna across different frequencies: (a) 0.915 GHz, (b) 1.4 GHz, (c) 2.45 GHz, and (d) 5.8 GHz.

5.3.3 SAR Distribution Analysis

In leadless pacemaker applications, the antenna system is encapsulated within a small capsule, which is implanted into the right ventricle of the patient to ensure long-term uninterrupted operation. The primary function of this system relies on electromagnetic (EM) radiation to receive and transmit vital data for the pacemaker. As the device continuously interacts with the body, the absorption of electromagnetic energy by human tissue becomes a critical concern. The Specific Absorption Rate (SAR) is the key metric used to quantify this energy absorption. This is particularly important in medical devices like pacemakers, where sustained exposure to EM radiation can lead to an increase in tissue temperature. To protect patient well-being, the IEEE C95.1-2019 standard sets a strict limit on SAR, capping it at 2W/kg when averaged over 10 grams of tissue. This standard ensures that the absorbed energy does not cause harmful tissue heating, maintaining the safety and functionality of the device [136]. To comprehensively evaluate the SAR performance of the proposed antenna, numerical simulations were conducted using a human body model. The capsule, equipped with the integrated antenna, was placed in an approximate location within the heart. To avoid interference with sur-

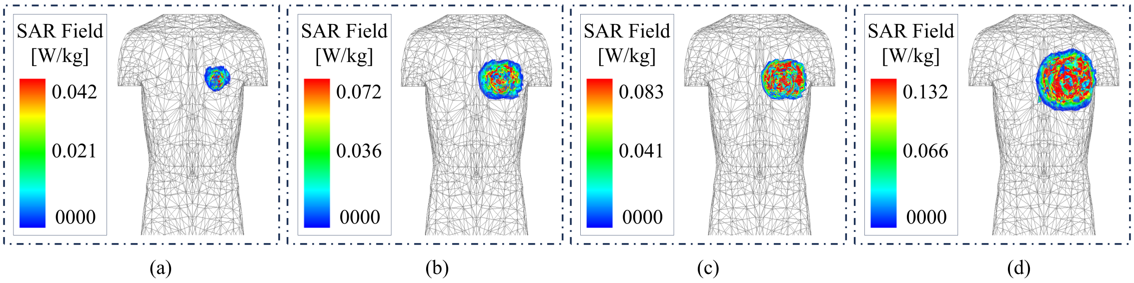

(a) (b) (c) (d)

Figure 5.9: SAR results of a 2x1 UWB-MIMO

rounding wireless devices, ensure compliance with SAR standards, and minimize electromagnetic interference (EMI), an input power of 25 μW was selected. This power level is essential for reducing signal conflicts in environments with multiple wireless systems operating in the same frequency bands. The simulations were carried out at this power level in accordance with the ITU-R RS.1346 guidelines for implantable medical devices [114]. Figure 5.9 shows the SAR analysis performed at several key frequencies relevant to medical telemetry and communication systems. The analysis covered 915 MHz for ISM (Industrial, Scientific and Medical) applications, 1400 MHz for telemetry and communication, and 2450 MHz and 5800 MHz for wireless communications. The simulated 10-gram averaged SAR values for all scenarios remained significantly below the 2 W/kg limit established by the IEEE C95.1-2019 standard. The highest observed SAR value, 0.132 W/kg, occurred at 5800 MHz. These findings consistently indicate that the proposed antenna system results in minimal exposure to electromagnetic radiation, ensuring patient safety while operating within the heart. Consequently, it is considered a viable option for leadless pacemaker applications.

5.3.4 Communication Link Assessment

To evaluate the communication link between the proposed implantable antenna and an external device, a link budget analysis was conducted. The methodology follows the theoretical framework established in chapter 2 Section 2.6.1.4, which includes the definitions and equations for link margin, received power, and receiver sensitivity.

In this analysis, a minimum link margin of 20 dB was adopted to ensure robust and reliable communication. This margin accounts for practical uncertainties such as propagation loss variations, interference, and hardware inefficiencies. A positive link margin is necessary for successful data reception, and the 20 dB buffer provides additional design assurance under real-world conditions.

The evaluation considered four data rates—1 Mbps, 10 Mbps, 25 Mbps, and 50 Mbps—which represent typical operating conditions for wireless medical telemetry systems. These data rates were chosen to reflect application-specific requirements, where higher rates can increase receiver sensitivity demands and reduce the achievable link margin.

The transmit power was fixed at -16 dBm, in accordance with European Research Council regulations [97]. The proposed implantable antenna served as the transmitter, while the receiver was modeled as an ideal half-wavelength dipole antenna with a gain of 2 dBi [137]. The antenna exhibited gains of -34.7 dBi at 0.915 GHz, -28.4 dBi at 1.4 GHz, -23.3 dBi at 2.45 GHz, and -20.1 dBi at 5.8 GHz. Polarization and impedance mismatch losses were not included in the analysis, as the antenna demonstrates excellent impedance matching characteristics. All other parameters relevant to the link budget analysis are detailed in Table 5.3.

Figure 5.10 illustrates the communication ranges achieved at different frequencies for a bit rate of 1 Mbps. The antenna achieved maximum communication distances of 13 m at 0.915 GHz, 14.9 m at 1.4 GHz, 16 m at 2.45 GHz, and 12 m at 5.8 GHz. As expected, increasing the bit rate led to reduced coverage distances across all frequencies due to the higher sensitivity requirements.

Despite the higher propagation loss typically associated with 2.45 GHz, the antenna's gain at this frequency was sufficiently high to enable better coverage compared to the lower-frequency bands. Specifically, the gain of -23.3 dBi at 2.45 GHz contributed to superior range performance compared to the gains of -34.7 dBi and -28.4 dBi at 0.915 GHz and 1.4 GHz, respectively. Conversely, although the gain at 5.8 GHz was relatively higher at -20.1 dBi, the signal experienced more significant attenuation due to high free-space path loss, resulting in the shortest communication range overall.

These findings emphasize the importance of balancing operating frequency, antenna gain, and data rate in the design of reliable wireless links for implantable

Table 5.3: Link Budget Parameters Analysis of a 2x1 UWB-MIMO

Variable	Parameter	Value	Unit
P_t	Transmitted power	25	μW
f	Frequency	915, 1400, 2450, 5800	MHz
G_t	Antenna gain	-34.7, -28.4, -23.3, -20.1	dBi
L_f	Path loss	Variable	dB
G_r	Receiver antenna gain	2	dBi
N_o	Noise power density	-203.93	dBm/Hz
T	Temperature	273	Kelvin
K	Boltzmann constant	1.38×10^{-23}	J/K
B_r	Bit rate	1, 10, 25, 50	Mbps
BER	Bit error rate	1×10^{-5}	-
E_b/N_o	Ideal PSK	9.6	dB
G_c	Coding gain	0	dB
G_d	Fixing deterioration	2.5	dB

medical devices.

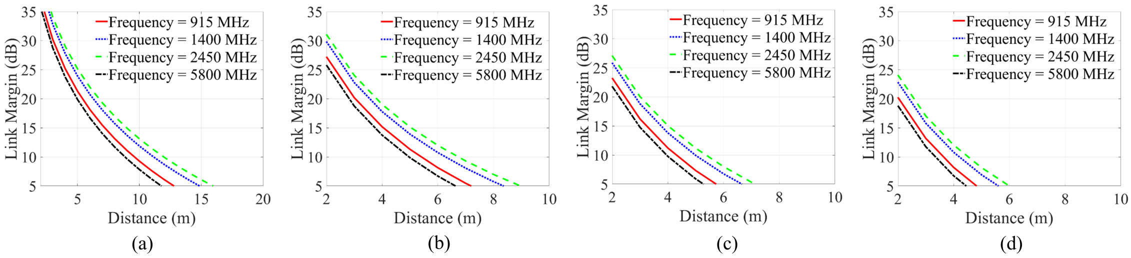

Figure 5.10: Link margins calculated for the 2x1 UWB-MIMO at (a) 1 Mbps, (b) 10 Mbps, (c) 25 Mbps, and (d) 50 Mbps across different frequency bands.

5.3.5 Channel Capacity Analysis

Analyzing the channel capacity (CC) is a crucial step in evaluating the performance of the proposed antenna, particularly when compared to single-input single-output (SISO) systems. Channel capacity, which defines the maximum data throughput that a communication system can handle, is a fundamental metric for assessing the efficiency of an antenna design. It is determined by factors such as the signal-to-noise ratio (SNR), the bandwidth, and the number of transmitting and receiving antennas. The theoretical foundation of channel capacity is rooted in Shannon's Capacity Theorem, which establishes an upper limit to the data rate based on the noise and bandwidth available in a communication channel.

In the case of multiple-input multiple-output (MIMO) systems, they offer a significant advantage over SISO systems by utilizing spatial diversity, enabling the transmission of multiple data streams simultaneously. This spatial diversity improves the data rate and enhances the system's resilience to multipath fading. MIMO systems exploit the independent paths created by multiple antennas, leading to an increase in capacity without the need for additional bandwidth. The channel capacity for a MIMO system is typically expressed by the following Equation 5.3:

$$CC = \log_2 \left(\det \left(I + \frac{\mathrm{SNR}}{N} H H^* \right) \right) \tag{5.3}$$

Where, det stands for the determinant, which quantifies the overall spatial diversity and capacity of the MIMO channel. I represents the identity matrix, corresponding to a case with no signal enhancement. The term SNR refers to the signal-to-noise ratio, N indicates the number of antennas, and H is the channel matrix, with H^* being its Hermitian transpose (the complex conjugate of H). The channel matrix is first obtained from the 2-D radiation patterns of the 2x1 UWB-MIMO antenna and then used to estimate the channel capacity [138]. Three configurations are compared in Figure 5.11: the ideal SISO, the proposed 2x1 UWB-MIMO, and the ideal 2x1 MIMO systems, with their respective channel capacities. In practical use, MIMO systems usually operate within an SNR range of 10 to 30 dB. For the purpose of this analysis, an SNR value of 20 dB is chosen as a representative average to evaluate the

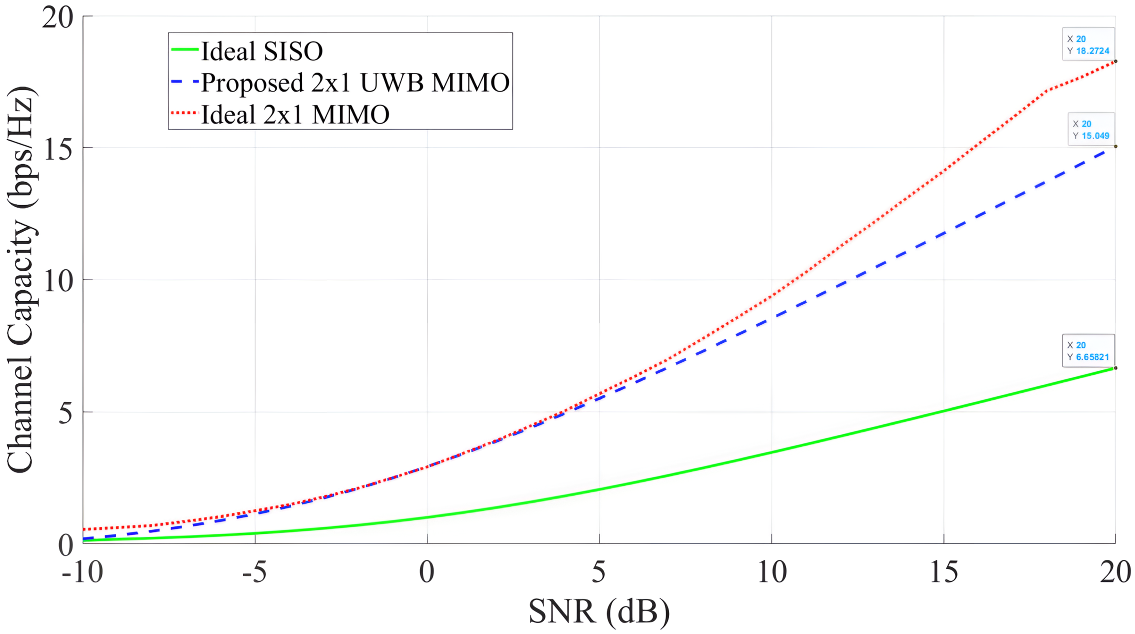

Figure 5.11: Channel capacity variation with SNR for ideal SISO, proposed 2×1 UWB-MIMO, and ideal 2×1 MIMO systems.

system performance [139]. The channel capacities at an SNR level of 20 dB for the various configurations are as follows: 6.65 bps/Hz for the ideal SISO, 15.04 bps/Hz for the proposed 2x1 UWB-MIMO, and 18.27 bps/Hz for the ideal 2x1 MIMO. These results demonstrate that the proposed 2x1 UWB-MIMO configuration significantly improves performance compared to the ideal SISO system. At lower SNR values, noise dominates, leading to similar channel capacities for both the ideal and proposed MIMO configurations. However, at higher SNR levels, the channel capacity of the proposed 2x1 UWB-MIMO system approaches that of the ideal 2x1 MIMO system. The slight difference between these two configurations at high SNR is primarily due to mutual coupling, which results from interference between closely spaced antenna elements. Although this effect may slightly reduce the performance of the proposed MIMO antenna, it still outperforms the SISO system in terms of capacity.

5.3.6 Envelope Correlation Coefficients

The envelope correlation coefficient (ECC) plays a critical role in evaluating the performance of the 2x1 UWB-MIMO antenna design. It measures the correlation between channels in a MIMO system, which is a key to understanding how effectively the system utilizes spatial diversity. In an ideal MIMO setup, the channels would be perfectly uncorrelated, allowing each channel to carry independent data without interference. This results in optimal performance and capacity.

However, in practical systems, channel interference and mutual coupling between closely spaced antennas often lead to some degree of correlation. Higher ECC values indicate a stronger correlation between the channels, which can limit the system's ability to fully exploit spatial diversity, thereby negatively affecting its performance. Consequently, minimizing the ECC is crucial for enhancing data throughput and reducing interference.

The ECC can be computed from either the S parameters of the antenna system or its far-field radiation patterns. The formula for calculating the ECC using the S parameters is provided in Equation 5.4. A lower ECC typically indicates better spatial diversity and overall efficiency of the MIMO system.

$$\mathrm{ECC} = \frac{|S_{11}S_{12}^{*} + S_{21}^{*}S_{22}|^2}{(1 - |S_{11}|^2 - |S_{21}|^2)(1 - |S_{22}|^2 - |S_{12}|^2)} \tag{5.4}$$

In this formulation, the parameters S_{11} correspond to the reflection coefficient of Antenna 1, while S_{22} refers to the reflection coefficient of Antenna 2. Meanwhile, S_{12} and S_{21} describe the mutual coupling between the two antennas. The terms S_{12}^{*} and S_{21}^{*} denote the complex conjugates of the transmission coefficients, which account for both the magnitude and the phase of the signals. A lower ECC value, ideally close to zero, indicates that the antennas are well isolated and operate independently.

Although the S-parameter method is widely used, it assumes lossless antennas operating in an isotropic environment. For antennas that exhibit significant losses, such as printed antennas, this assumption may not hold, potentially leading to inaccurate ECC evaluations [124]. Therefore, in our study, ECC was computed using the radiation pattern-based approach shown in Equation 5.5. This method offers a more realistic and accurate characterization of channel correlation by accounting for the actual far-field behavior of the antenna elements in three-dimensional space. All ECC values reported in this chapter—including those plotted in Figure 5.12—are based on this radiation-pattern method, ensuring consistency and physical relevance in the performance assessment of the proposed MIMO design. All results were

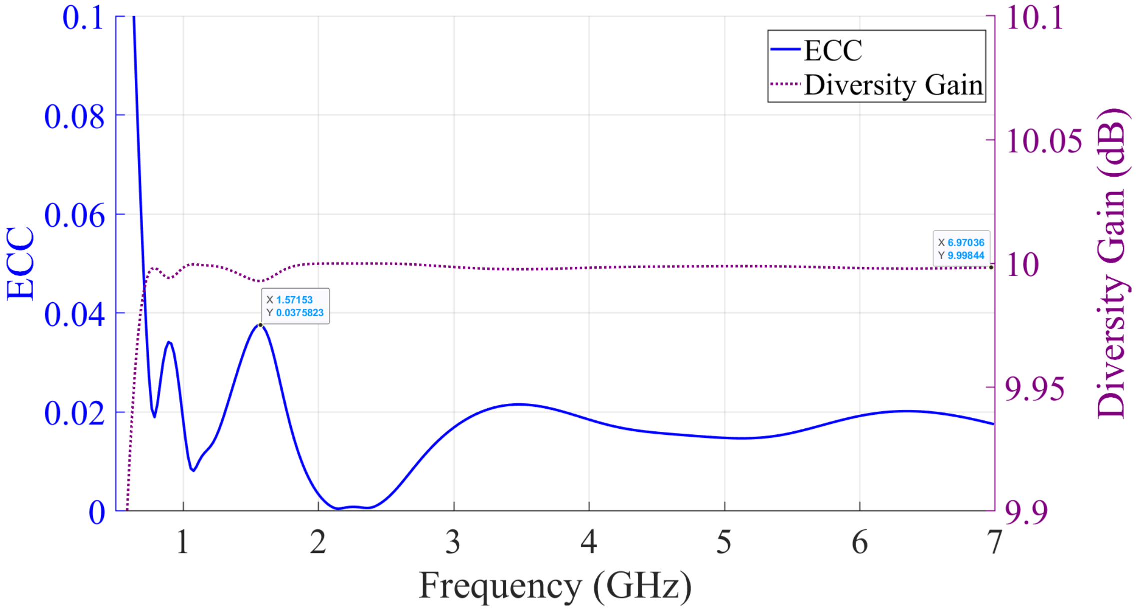

Figure 5.12: The ECC and DG of the 2x1 UWB-MIMO antenna

obtained using full-wave simulations in HFSS, and ECC values were computed by exporting 3D far-field data and post-processing them in MATLAB.

$$\mathrm{ECC} = \frac{\left(\int_{4\pi} \mathbf{A}_{n,i}(\theta,\phi)\cdot\mathbf{A}_{n,j}(\theta,\phi)\,d\Omega\right)^2}{\left(\int_{4\pi} |\mathbf{A}_{n,i}(\theta,\phi)|^2\,d\Omega\right)\cdot\left(\int_{4\pi} |\mathbf{A}_{n,j}(\theta,\phi)|^2\,d\Omega\right)} \tag{5.5}$$

In this equation, $\mathbf{A}_{n,i}(\theta,\phi)$ and $\mathbf{A}_{n,j}(\theta,\phi)$ represent the far-field 3D radiation patterns of Antenna 1 and Antenna 2, respectively. These radiation patterns are functions of the spherical coordinates θ (elevation angle) and ϕ (azimuth angle). The symbol (dΩ) represents the solid angle and the integrals are performed on the entire sphere, encompassing all directions in a three-dimensional space. The numerator, $\left(\int_{4\pi} \mathbf{A}_{n,i}(\theta,\phi)\cdot\mathbf{A}_{n,j}(\theta,\phi)\,d\Omega\right)^2$, quantifies the spatial overlap between the radiation patterns of the two antennas. A higher overlap indicates a greater correlation. The denominator normalizes the expression by considering the total radiated power of each antenna, which is calculated through the integrals $\int_{4\pi} |\mathbf{A}_{n,i}(\theta,\phi)|^2\,d\Omega$ and $\int_{4\pi} |\mathbf{A}_{n,j}(\theta,\phi)|^2\,d\Omega$.

The ECC based on radiation patterns offers a spatial analysis of the correlation between antennas by assessing their radiated fields. For the 2×1 UWB-MIMO configuration, an ECC value lower than 0.037 indicates that the antennas exhibit different radiation characteristics, which are favorable for MIMO applications.

Table 5.4: Comparison Between the Proposed 2×1 UWB-MIMO Antenna and Prior Designs

Parameters / Ref.	[118]	[35]	[119]	[13]	[120]	[115]	**This Work**
Freq. (GHz)	0.915	0.433	2.4	0.915	2.45	2.45	2.45
BW (MHz)	2200	146.49	1240	900	1002	320	6728
FBW (%)	157.1	33.9	62.6	84.9	36.8	13.1	165.1
Gain (dBi)	-33.1	-30	-27.6	-30.4	-21.3	-20.5	-23.3
Size (λ_g^3)	5.24×10^{-5}	1.78×10^{-6}	3.21×10^{-4}	2.67×10^{-6}	3.23×10^{-3}	7.06×10^{-5}	1.52×10^{-6}
Depth (mm)	57	90	6.5	75	4	75	50
Elements	2	2	2	2	2	2	2
Isolation (dB)	>20	>26	>20	20	>20	>28	>21
CC (bps/Hz)	N/A	10	8.8	14	8.37	9.9	15.04
ECC	<0.5	0.1	<0.25	<0.1	<0.1	<0.1	<0.037

Diversity gain (DG) is another crucial performance indicator for MIMO antenna systems, as it measures the improvement in signal quality and system dependability provided by antenna diversity. DG reflects the system's ability to reduce fading and improve overall link performance. The relationship between DG and ECC is given by Equation 5.6.

$$\mathrm{DG} = 10\sqrt{1 - (\mathrm{ECC})^2} \tag{5.6}$$

In this equation, a smaller ECC value denotes a lower correlation between antennas, leading to a higher DG and better system performance. As demonstrated in Figure 5.12, within the antenna's operational frequency range, the ECC remains below 0.037, ensuring that the DG remains above 9.99 dB.

To ensure a comprehensive evaluation, Table 5.4 compares the proposed 2 × 1 UWB-MIMO antenna with several state-of-the-art designs reported in the literature. For fairness, emphasis is placed on comparing antennas operating around the same frequency range (2.4–2.45 GHz), as performance parameters such as bandwidth and gain are inherently frequency-dependent. Among the antennas operating at 2.45 GHz [115,119,120], the proposed design stands out with an ultra-wide bandwidth of 6728 MHz and a corresponding fractional bandwidth (FBW) of 165.12%, significantly exceeding that of all other works. This extended bandwidth is particularly beneficial for implantable systems as it enhances resilience to frequency detuning and supports high-data-rate communication per Shannon's theorem. In terms of gain, although implantable antennas typically exhibit low values due to lossy tissue environments, the proposed antenna's gain of -23.3 dBi is comparable to or better than similar systems such as [119] (-27.6 dBi) and [13] (-30.4 dBi), while still supporting deep-tissue implantation (50 mm depth). From a miniaturization standpoint, the proposed antenna achieves the smallest normalized volume ($1.52 \times 10^{-6}\lambda_g^3$), reflecting its highly compact structure suitable for capsule-type devices. This compactness is achieved without compromising other key metrics, such as isolation ($>$21 dB) and envelope correlation coefficient (ECC < 0.037), which indicate strong MIMO performance. Finally, the channel capacity (CC) at 20 dB SNR is 15.04 bps/Hz—the highest among the reviewed works—confirming the antenna's ability to sustain robust, high-speed telemetry in a multipath-rich, lossy environment. In summary, compared to other implantable MIMO antennas operating in the same band, the proposed design provides a superior trade-off between bandwidth, size, isolation, and communication performance, making it highly suitable for next-generation biomedical telemetry applications.

5.4 Conclusion

This study successfully developed a miniaturized 2x1 UWB-MIMO antenna optimized for next-generation leadless pacemakers. The design, featuring compact rectangular loop antenna elements and a common slotted ground plane, demonstrated good isolation between them, with low mutual coupling values across key frequencies. The antenna achieved a wide operational bandwidth, covering a range from 710 MHz to 7438 MHz, with a fractional bandwidth of 165.12%. Performance evaluations, including Specific Absorption Rate (SAR), channel capacity, and correlation coefficient, confirmed antenna safety and efficiency, with SAR values well within safe limits. The 2x1 UWB-MIMO configuration exhibited a high channel capacity at signal-to-noise ratio (SNR) = 20 dB, making the design suitable for medical applications. The fabricated prototype, which was tested with tissue-equivalent material, validated the simulation results, confirming the practicality of the proposed antenna for the integration of leadless pacemakers.

CHAPTER 6

Conclusion and Future Work

6.1 Conclusion

This thesis presents significant advancements in the design of implantable antennas for leadless pacemaker applications. It provides a comprehensive review of implantable antenna design, highlighting the associated challenges and limitations. The issues addressed in this work include size constraints, frequency detuning, and signal fading. To overcome these challenges, three innovative antenna designs have been developed, each aimed at improving size efficiency, expanding bandwidth, and enhancing reliability, respectively, within the complex biological environment. These designs offer promising solutions for enhancing the performance of implantable antennas in medical applications, as outlined below:

- **First Contribution:** This implantable antenna is designed to achieve an ultra-wide bandwidth, effectively mitigating the issue of frequency detuning. The radiating element is rectangular with a centrally positioned large U-shaped slot. An inductive shorting pin, with a radius of 0.1 mm, is placed at one corner of the patch. Additionally, several rectangular slots are incorporated along the edges of the patch. On the opposite side, the ground plane features multiple expanded slots to further optimize performance. To ensure wideband performance while maintaining a compact form, reactive loading techniques are employed. The antenna is constructed using Rogers RO3003 material, which has a low loss tangent ($\tan\delta$) of 0.0010 and a relative permittivity (ε_r) of 3. Both the substrate and superstrate have a standard thickness of 0.127 mm. The antenna has a compact volume of $9.44\,\mathrm{mm}^3$ and provides a wide bandwidth of 3390 MHz, with a fractional bandwidth of 138%. The frequency range spans from 0.76 to 4.15 GHz, covering several critical bands such as the ISM (0.869, 0.915, and 2.45 GHz), WMTS (1.4 GHz), and midfield (1.6 GHz) bands. Simulations conducted in a homogeneous phantom model of heart tissue reveal antenna gains of $-32.4\,\mathrm{dBi}$ at 0.915 GHz, $-27.94\,\mathrm{dBi}$ at 1.4 GHz, and $-19.8\,\mathrm{dBi}$ at 2.45 GHz. The proposed antenna also demonstrates low Specific Absorption Rate (SAR) levels in a full-body model, with SAR values below 1.6 W/kg for 1 g of tissue and 2.0 W/kg for 10 g of tissue. Furthermore, a link budget analysis was performed to estimate the telemetry range at a 10 Mbps data rate. The antenna prototype was fabricated and subsequently tested on minced pork meat, with the measured results closely matching the simulated predictions.

- **Second Contribution:** This antenna was developed to address both frequency detuning and size constraints. Compared to the first design, it achieves greater compactness and a wider bandwidth. The antenna features a rectangular radiating patch with a central C-shaped slot, which enhances its functional efficiency. To improve inductance, a via with a precisely chosen radius of 0.08 mm is strategically placed at the bottom corner. Additionally, the ground plane is optimized with expanded slots and asymmetrical circular features near its center, further enhancing performance. Constructed using RO3003 material, the antenna benefits from a low loss tangent ($\tan\delta = 0.0013$) and a relative permittivity ($\varepsilon_r = 3$), ensuring efficient and reliable operation. The design achieves a compact volume of only $8.33\,\mathrm{mm}^3$ and provides an ultra-wide -10 dB bandwidth of 4330 MHz, corresponding to a fractional bandwidth of 152.7%. It operates over a frequency range of 0.67 GHz to 5 GHz. Simulation results demonstrate antenna gains of $-31.3\,\mathrm{dBi}$ at 0.915 GHz, $-25.8\,\mathrm{dBi}$ at 1.4 GHz, and $-21.9\,\mathrm{dBi}$ at 2.45 GHz. Furthermore, the antenna exhibits peak Specific Absorption Rate (SAR) values of 320.4 W/kg at 0.915 GHz, 332.8 W/kg at 1.4 GHz, and 464.1 W/kg at 2.45 GHz. To assess the reliability of the wireless communication link, a link budget analysis was conducted to estimate the range between the transmitter and receiver at data rates of 10 Mbps and 25 Mbps. The performance of the antenna was further validated through testing in minced pork tissue, with the measured results closely aligning with the simulated results.

- **Third Contribution:** This antenna was developed to overcome signal fading and multipath interference. The antenna employs a two-port ultra-wideband multiple-input, multiple-output (UWB-MIMO) configuration, with two rectangular loop antenna elements positioned side by side. To enhance performance, the design includes a shared slotted ground plane, substrate, and superstrate. The compact design of the antenna utilizes low-permittivity materials ($\varepsilon_r = 2.2$) for both the substrate and superstrate to enhance bandwidth. Size reduction is achieved through techniques such as optimized rectangular loop elements, via-based inductive loading, and strategically placed U-shaped and open-ended slots in the ground plane. These methods enable effective miniaturization, achieving a compact form factor of $12 \times 5.4 \times 0.254\,\mathrm{mm}^3$ ($16.4\ \mathrm{mm}^3$), along with impedance matching and bandwidth enhancement. Isolation between the antenna elements is significantly improved through the addition of two rectangular slots placed at the center of the ground plane, one for each loop, along with a small 0.8 mm gap between the elements. This design achieves mutual coupling of less than $-21\,\mathrm{dB}$ across the entire operational bandwidth. The UWB-MIMO antenna offers an impressive fractional bandwidth (FBW) of 165.12%, allowing it to function across a broad frequency range from 710 MHz to 7438 MHz. Various performance metrics, including Specific Absorption Rate (SAR), link budget, channel capacity, and correlation coefficient, were thoroughly analyzed. The measured SAR values remained well within safe limits, with readings of 0.042 W/kg at 915 MHz, 0.072 W/kg at 1.4 GHz, 0.083 W/kg at 2.45 GHz, and 0.132 W/kg at 5.8 GHz, all for an input power of 25 µW. When operating at a signal-to-noise ratio (SNR) of 20 dB, the UWB-MIMO antenna achieved a channel capacity of 15.04 bps/Hz. To validate the HFSS simulation results, a prototype was fabricated and subsequently tested using minced pork as a tissue-equivalent medium. The experimental results demonstrated strong agreement with the simulated results, confirming the suitability of the proposed antenna for next-generation leadless pacemakers and other implantable biomedical applications.

6.2 Future Work

This thesis has addressed several challenges related to implantable antennas; however, additional areas remain for future investigation. As outlined in the implantable antenna design roadmap in Chapter 2, further validation is needed before these designs can be applied to real-world leadless pacemaker applications for patients. In particular, future work should prioritize conducting additional tests in living organisms, such as pigs or rats, to assess the designs' practicality and safety.

Furthermore, exploring wireless power transfer for leadless pacemaker devices is another important avenue for future work. Since these devices are designed for long-term implantation, enabling battery recharging without replacement would significantly reduce patient discomfort and associated costs. A promising future development involves creating a comprehensive rectenna system to wirelessly power implantable devices, offering a more efficient and cost-effective solution.

Additionally, future work should investigate the data rate requirements of emerging biomedical telemetry systems. As next-generation pacemakers are expected to support real-time monitoring, secure firmware updates, and synchronization with wearable or external diagnostic devices, antenna systems must meet higher throughput and latency demands. Adapting the antenna designs to reliably support data rates exceeding 50 Mbps may be necessary.

Integration of emerging communication technologies, such as sub-THz bands, 6G-inspired nano-networks, or ultra-low-power backscatter communication, could also be considered for future implantable devices.

Finally, the use of metamaterials or metasurfaces, including electromagnetic bandgap (EBG) structures or artificial magnetic conductors (AMCs), could be explored to improve antenna miniaturization, gain, and isolation without increasing complexity or volume. Such materials could enable smarter electromagnetic control in lossy environments like human tissue.

Bibliography

[1] H. Li, B. Wang, L. Guo, and J. Xiong, "Efficient and wideband implantable antenna based on magnetic structures," *IEEE Transactions on Antennas and Propagation*, vol. 67, no. 12, pp. 7242–7251, 2019.

[2] Z. Xia, H. Li, Z. Lee, S. Xiao, W. Shao, X. Ding, *et al.*, "A wideband circularly polarized implantable patch antenna for ism band biomedical applications," *IEEE Transactions on Antennas and Propagation*, vol. 68, no. 3, pp. 2399–2404, 2019.

[3] W. Cui, R. Liu, L. Wang, M. Wang, H. Zheng, and E. Li, "Design of wideband implantable antenna for wireless capsule endoscope system," *IEEE Antennas and Wireless Propagation Letters*, vol. 18, no. 12, pp. 2706–2710, 2019.

[4] S. Bhattacharjee, S. Maity, S. R. Bhadra Chaudhuri, and M. Mitra, "Metamaterial-inspired wideband biocompatible antenna for implantable applications," *IET Microwaves, Antennas & Propagation*, vol. 12, no. 11, pp. 1799–1805, 2018.

[5] R. Liu, K. Zhang, Z. Li, W. Cui, W. Liang, M. Wang, C. Fan, H. Zheng, and E. Li, "A wideband circular polarization implantable antenna for health monitor microsystem," *IEEE Antennas and Wireless Propagation Letters*, vol. 20, no. 5, pp. 848–852, 2021.

[6] A. Basir, A. Bouazizi, M. Zada, A. Iqbal, S. Ullah, and U. Naeem, "A dual-band implantable antenna with wide-band characteristics at mics and ism bands," *microwave and optical technology letters*, vol. 60, no. 12, pp. 2944–2949, 2018.

[7] S. Hout and J.-Y. Chung, "Design and characterization of a miniaturized implantable antenna in a seven-layer brain phantom," *IEEE Access*, vol. 7, pp. 162062–162069, 2019.

[8] A. Basir and H. Yoo, "A stable impedance-matched ultrawideband antenna system mitigating detuning effects for multiple biotelemetric applications,"

IEEE Transactions on Antennas and Propagation, vol. 67, no. 5, pp. 3416–3421, 2019.

[9] S. A. A. Shah and H. Yoo, "Scalp-implantable antenna systems for intracranial pressure monitoring," *IEEE Transactions on Antennas and Propagation*, vol. 66, no. 4, pp. 2170–2173, 2018.

[10] I. A. Shah, M. Zada, and H. Yoo, "Design and analysis of a compact-sized multiband spiral-shaped implantable antenna for scalp implantable and leadless pacemaker systems," *IEEE Transactions on Antennas and Propagation*, vol. 67, no. 6, pp. 4230–4234, 2019.

[11] A. Lamkaddem, A. El Yousfi, V. González-Posadas, and D. Segovia-Vargas, "Miniaturized dual band implantable antenna for implanted biomedical devices," *IEEE Access*, vol. 12, pp. 15026–15036, 2024.

[12] N. Abbas, S. A. A. Shah, A. Basir, Z. Bashir, A. Akram, and H. Yoo, "Miniaturized antenna for high data rate implantable brain-machine interfaces," *IEEE Access*, vol. 10, pp. 66018–66027, 2022.

[13] L. Chang, A. Iqbal, A. Basir, R. B. Simorangkir, and I. B. Mabrouk, "Conformal mimo ultra-wideband antenna design for high-speed wireless telemetry in capsule endoscopy systems," *IEEE Transactions on Antennas and Propagation*, 2024.

[14] Y. Feng, S.-P. Pan, J.-W. Li, P. Chen, L. Qi, and G.-S. Li, "Design of ultra-wideband conformal capsule antenna for wireless capsule endoscopy system," in *2020 Cross Strait Radio Science & Wireless Technology Conference (CSRSWTC)*, pp. 1–3, IEEE, 2020.

[15] A. Iqbal, P. R. Sura, A. Smida, M. Al-Hasan, I. B. Mabrouk, and T. A. Denidni, "Dual-band 3-d implantable mimo antenna for iot-enabled wireless capsule endoscopy," *IEEE Internet of Things Journal*, 2024.

[16] J. C. Lin and Y.-J. Wang, "An implantable microwave antenna for interstitial hyperthermia," *Proceedings of the IEEE*, vol. 75, no. 8, pp. 1132–1133, 1987.

[17] F. Merli, "Implantable antennas for biomedical applications," tech. rep., EPFL, 2011.

[18] R. Alrawashdeh, *Implantable antennas for biomedical applications.* PhD thesis, University of Liverpool, 2015.

[19] A. Barbuti, M. Baruscotti, and D. Difrancesco, "The pacemaker current: from basics to the clinics," *Journal of cardiovascular electrophysiology*, vol. 18, no. 3, pp. 342–347, 2007.

[20] H. T. McElderry, J. C. Evans, A. Al-Ahmad, K. Ellenbogen, A. Natale, and P. Wang, "Pacemaker systems," *Pacemakers and Implantable Cardioverter Defibrillators. An Expert's Manual. Minneapolis: cardiotext Publishing*, pp. 3–18, 2010.

[21] E. E. Gul and M. Kayrak, “Common pacemaker problems: lead and pocket complications,” *Modern Pacemakers–Present and Future/ed. MR Das. Rijeka, Croatia*, pp. 299–318, 2011.

[22] T. Mela and J. P. Singh, “Leadless pacemakers: leading us into the future?,” 2015.

[23] A. Groner and K. Grippe, “The leadless pacemaker: An innovative design to enhance pacemaking capabilities,” *Jaapa*, vol. 32, no. 6, pp. 48–50, 2019.

[24] H. M. Seriwala, M. S. Khan, M. B. Munir, I. Bin Riaz, H. Riaz, S. Saba, and A. H. Voigt, “Leadless pacemakers: A new era in cardiac pacing,” *Journal of cardiology*, vol. 67, no. 1, pp. 1–5, 2016.

[25] N. Molitor, S. Saleem-Talib, H. Ramanna, D. Hofer, A. Breitenstein, and J. Steffel, “Leadless pacemaker implantation via the internal jugular vein,” *Europace*, vol. 26, no. 8, p. euae199, 2024.

[26] M. Parvez Mahmud, N. Huda, S. H. Farjana, M. Asadnia, and C. Lang, “Recent advances in nanogenerator-driven self-powered implantable biomedical devices,” *Advanced Energy Materials*, vol. 8, no. 2, p. 1701210, 2018.

[27] J. Z. Lee, S. K. Mulpuru, and W. K. Shen, “Leadless pacemaker: performance and complications,” *Trends in Cardiovascular Medicine*, vol. 28, no. 2, pp. 130–141, 2018.

[28] A. Joury, T. Bob-Manuel, A. Sanchez, F. Srinithya, A. Sleem, A. Nasir, A. Noor, D. Penfold, R. Bober, D. P. Morin, *et al.*, “Leadless and wireless cardiac devices: The next frontier in remote patient monitoring,” *Current Problems in Cardiology*, vol. 46, no. 5, p. 100800, 2021.

[29] R. F. Harrington, “Effect of antenna size on gain, bandwidth, and efficiency,” *J. Res. Nat. Bur. Stand*, vol. 64, no. 1, pp. 1–12, 1960.

[30] H. Garn and C. Gabriel, “Present knowledge about specific absorption rates inside a human body exposed to radiofrequency electromagnetic fields,” *Health physics*, vol. 68, no. 2, pp. 147–156, 1995.

[31] R. Chávez-Santiago, K. Øyri, S. Støa, I. Balasingham, and E. Fosse, “Experimental assessment of interference in the 2.4 ghz ism band from wireless medical sensors on the imaging system of an advanced operating room,” in *Proc. Asia-Pacific EMC Symp.(APEMC)*, pp. 16–19, 2011.

[32] R. Pethig, “Dielectric properties of body tissues,” *Clinical Physics and Physiological Measurement*, vol. 8, no. 4A, p. 5, 1987.

[33] M. M. Soliman, M. E. Chowdhury, A. Khandakar, M. T. Islam, Y. Qiblawey, F. Musharavati, and E. Zal Nezhad, “Review on medical implantable antenna technology and imminent research challenges,” *Sensors*, vol. 21, no. 9, p. 3163, 2021.

[34] W. Joseph, G. Vermeeren, L. Verloock, and L. Martens, "Estimation of whole-body sar from electromagnetic fields using personal exposure meters," *Bioelectromagnetics: Journal of the Bioelectromagnetics Society, The Society for Physical Regulation in Biology and Medicine, The European Bioelectromagnetics Association*, vol. 31, no. 4, pp. 286–295, 2010.

[35] A. Iqbal, M. Al-Hasan, I. B. Mabrouk, and M. Nedil, "A compact implantable mimo antenna for high-data-rate biotelemetry applications," *IEEE Transactions on Antennas and Propagation*, vol. 70, no. 1, pp. 631–640, 2021.

[36] X.-y. Hu, W.-l. Yin, F. Du, C. Zhang, P. Xiao, and G. Li, "Biomedical applications and challenges of in-body implantable antenna for implantable medical devices: A review," *AEU-International Journal of Electronics and Communications*, vol. 174, p. 155053, 2024.

[37] Federal Communications Commission, "First report and order: Revision of part 15 of the commission's rules regarding ultra-wideband transmission systems," 2002. FCC 02-48.

[38] A. Kiourti and K. S. Nikita, "A review of implantable patch antennas for biomedical telemetry: Challenges and solutions [wireless corner]," *IEEE Antennas and Propagation Magazine*, vol. 54, no. 3, pp. 210–228, 2012.

[39] M. R. Yuce and J. Y. Khan, *Implementation of Wireless Body Sensor Networks for Healthcare Monitoring.* Springer, 2011.

[40] "IEEE Standard for Safety Levels with Respect to Human Exposure to Radio Frequency Electromagnetic Fields, 3 kHz to 300 GHz," 1999.

[41] "IEEE Standard for Safety Levels with Respect to Human Exposure to Radio Frequency Electromagnetic Fields, 3 kHz to 300 GHz," 2005.

[42] R. E. Fields, "Evaluating compliance with fcc guidelines for human exposure to radiofrequency electromagnetic fields," *Oet Bull*, vol. 65, no. 10, pp. 1–57, 1997.

[43] E. T. E. FIELDS, "Guidelines for limiting human exposure to electromagnetic fields up to 300 ghz," 2009.

[44] C. Liu, Y.-X. Guo, and S. Xiao, "A review of implantable antennas for wireless biomedical devices," in *Forum for electromagnetic research methods and application technologies (FERMAT)*, vol. 14, pp. 1–11, 2016.

[45] D. Williams, *The Williams dictionary of biomaterials*, vol. 173. Liverpool University Press, 1999.

[46] M. A. J. bin Mohd Idrus, M. S. Zulkefli, W. M. I. bin Wan Zahalan, S. P. Jack, and M. H. Mat, "Biocompatibility for in-body biotelemetry devices: A review of antenna design and materials," in *2024 IEEE 1st International Conference on Communication Engineering and Emerging Technologies (ICoCET)*, pp. 1–4, IEEE, 2024.

[47] A. K. Skrivervik and F. Merli, “Design strategies for implantable antennas,” in *2011 Loughborough Antennas & Propagation Conference*, pp. 1–5, IEEE, 2011.

[48] T. Karacolak, R. Cooper, J. Butler, S. Fisher, and E. Topsakal, “In vivo verification of implantable antennas using rats as model animals,” *IEEE Antennas and Wireless Propagation Letters*, vol. 9, pp. 334–337, 2010.

[49] W. contributors, “Titanium biocompatibility,” 2024. Accessed: 2024-12-03.

[50] W. contributors, “Gold,” 2024. Accessed: 2024-12-03.

[51] K. A. Psathas, A. Kiourti, and K. S. Nikita, “Biocompatibility of implantable antennas: Design and performance considerations,” in *The 8th European conference on antennas and propagation (EuCAP 2014)*, pp. 1566–1570, IEEE, 2014.

[52] A. Kiourti and K. S. Nikita, “Implantable antennas: A tutorial on design, fabrication, and in vitro\/in vivo testing,” *IEEE Microwave Magazine*, vol. 15, no. 4, pp. 77–91, 2014.

[53] J. Abadia, F. Merli, J. Zürcher, J. R. Mosig, and A. K. Skrivervik, “3d-spiral small antenna design and realization for biomedical telemetry in the mics band,” *Radioengineering*, vol. 18, no. 4, pp. 359–367, 2009.

[54] F. Curry, A. M. Chrysler, T. Tasnim, J. E. Shea, J. Agarwal, C. M. Furse, and H. Zhang, “Biostable conductive nanocomposite for implantable subdermal antenna,” *APL Materials*, vol. 8, no. 10, 2020.

[55] H. A. Wheeler, “Fundamental limitations of small antennas,” *Proceedings of the IRE*, vol. 35, no. 12, pp. 1479–1484, 1947.

[56] L. J. Chu, “Physical limitations of omni-directional antennas,” *Journal of Applied Physics*, vol. 19, no. 12, pp. 1163–1175, 1948.

[57] S. Gabriel, R. Lau, and C. Gabriel, “The dielectric properties of biological tissues: Ii. measurements in the frequency range 10 hz to 20 ghz,” *Physics in medicine & biology*, vol. 41, no. 11, p. 2251, 1996.

[58] Z. Duan, Y.-X. Guo, M. Je, and D.-L. Kwong, “Design and in vitro test of a differentially fed dual-band implantable antenna operating at mics and ism bands,” *IEEE transactions on antennas and propagation*, vol. 62, no. 5, pp. 2430–2439, 2014.

[59] J. Gemio, J. Parron, and J. Soler, “Human body effects on implantable antennas for ism bands applications: Models comparison and propagation losses study,” *Progress In Electromagnetics Research*, vol. 110, pp. 437–452, 2010.

[60] R. Porath, “Theory of miniaturized shorting-post microstrip antennas,” *IEEE Transactions on Antennas and Propagation*, vol. 48, no. 1, pp. 41–47, 2000.

[61] J. Rashed and C.-T. Tai, “A new class of resonant antennas,” *IEEE Transactions on Antennas and Propagation*, vol. 39, no. 9, pp. 1428–1430, 1991.

[62] D. Guha, M. Biswas, and Y. M. Antar, “Microstrip patch antenna with defected ground structure for cross polarization suppression,” *IEEE antennas and wireless propagation letters*, vol. 4, pp. 455–458, 2005.

[63] Y.-s. Takigawa, S. Kashihara, and F. Kuroki, “Integrated slot spiral antenna etched on heavily-high permittivity piece,” in *2007 Asia-Pacific Microwave Conference*, pp. 1–4, IEEE, 2007.

[64] A. Natarajan, A. Komijani, X. Guan, A. Babakhani, and A. Hajimiri, “A 77-ghz phased-array transceiver with on-chip antennas in silicon: Transmitter and local lo-path phase shifting,” *IEEE Journal of Solid-State Circuits*, vol. 41, no. 12, pp. 2807–2819, 2006.

[65] P. Momenroodaki, Z. Popovic, and R. Scheeler, “A 1.4-ghz radiometer for internal body temperature measurements,” in *2015 European Microwave Conference (EuMC)*, pp. 694–697, IEEE, 2015.

[66] P. Momenroodaki, R. D. Fernandes, and Z. Popović, “Air-substrate compact high gain rectennas for low rf power harvesting,” in *2016 10th European conference on antennas and propagation (EuCAP)*, pp. 1–4, IEEE, 2016.

[67] P. M. Ikonen, K. N. Rozanov, A. V. Osipov, P. Alitalo, and S. A. Tretyakov, “Magnetodielectric substrates in antenna miniaturization: Potential and limitations,” *IEEE Transactions on Antennas and Propagation*, vol. 54, no. 11, pp. 3391–3399, 2006.

[68] L.-J. Xu, Y.-X. Guo, and W. Wu, “Bandwidth enhancement of an implantable antenna,” *IEEE Antennas and Wireless Propagation Letters*, vol. 14, pp. 1510–1513, 2014.

[69] C. Liu, Y.-X. Guo, and S. Xiao, “Capacitively loaded circularly polarized implantable patch antenna for ism band biomedical applications,” *IEEE transactions on antennas and propagation*, vol. 62, no. 5, pp. 2407–2417, 2014.

[70] A. Alghamdi, A. Basir, A. Iqbal, R. B. Simorangkir, M. Al-Hasan, and I. B. Mabrouk, “Compact antenna with broadband wireless biotelemetry for future leadless pacemakers,” *IEEE Transactions on Antennas and Propagation*, 2024.

[71] G. Kumar and K. P. Ray, *Broadband microstrip antennas*. Artech house, 2002.

[72] R. Sahu, H. Pradhan, B. B. Mangaraj, and S. K. Behera, “Defected ground structure based compact uwb dielectric resonator antennas with enhanced bandwidth,” *Frequenz*, vol. 77, no. 11-12, pp. 537–548, 2023.

[73] P. Zakavi, N. C. Karmakar, and I. Griggs, “Wireless orthopedic pin for bone healing and growth: Antenna development,” *IEEE transactions on antennas and propagation*, vol. 58, no. 12, pp. 4069–4074, 2010.

[74] A. Kiourti and K. S. Nikita, “Miniature scalp-implantable antennas for telemetry in the mics and ism bands: Design, safety considerations and link budget analysis,” *IEEE Transactions on antennas and propagation*, vol. 60, no. 8, pp. 3568–3575, 2012.

[75] A. Alomainy and Y. Hao, “Modeling and characterization of biotelemetric radio channel from ingested implants considering organ contents,” *IEEE Transactions on Antennas and Propagation*, vol. 57, no. 4, pp. 999–1005, 2009.

[76] W. contributors, “Free-space path loss,” 2024. Accessed: 2024-12-07.

[77] Y. Huang, *Antennas: from theory to practice*. John Wiley & Sons, 2021.

[78] A. Basir, Y. Cho, I. A. Shah, S. Hayat, S. Ullah, M. Zada, S. A. A. Shah, and H. Yoo, “Implantable and ingestible antenna systems: From imagination to realization [bioelectromagnetics],” *IEEE Antennas and Propagation Magazine*, vol. 65, no. 5, pp. 70–83, 2023.

[79] S. M. Asif, J. W. Hansen, A. Iftikhar, D. L. Ewert, and B. D. Braaten, “Computation of available rf power inside the body and path loss using in vivo experiments,” *IET Microwaves, Antennas & Propagation*, vol. 13, no. 1, pp. 122–126, 2019.

[80] M. Rav Acha, E. Soifer, and T. Hasin, “Cardiac implantable electronic miniaturized and micro devices,” *Micromachines*, vol. 11, no. 10, p. 902, 2020.

[81] N. E. Beurskens, K. T. Breeman, K. J. Dasselaar, A. C. Meijer, A.-F. B. Quast, F. V. Tjong, and R. E. Knops, “Leadless cardiac pacing systems: current status and future prospects,” *Expert review of medical devices*, vol. 16, no. 11, pp. 923–930, 2019.

[82] M. Fallahpour and R. Zoughi, “Antenna miniaturization techniques: A review of topology-and material-based methods,” *IEEE Antennas and Propagation Magazine*, vol. 60, no. 1, pp. 38–50, 2017.

[83] Z. Xia, H. Li, Z. Lee, S. Xiao, W. Shao, X. Ding, *et al.*, “A wideband circularly polarized implantable patch antenna for ism band biomedical applications,” *IEEE Transactions on Antennas and Propagation*, vol. 68, no. 3, pp. 2399–2404, 2020.

[84] M. Zada, I. A. Shah, A. Basir, and H. Yoo, “Ultra-compact implantable antenna with enhanced performance for leadless cardiac pacemaker system,” *IEEE Transactions on antennas and propagation*, vol. 69, no. 2, pp. 1152–1157, 2020.

[85] F. Faisal, M. Zada, H. Yoo, I. B. Mabrouk, M. Chaker, and T. Djerafi, “An ultra-miniaturized antenna with ultra-wide bandwidth for future cardiac leadless pacemaker,” *IEEE Transactions on Antennas and Propagation*, vol. 70, no. 7, pp. 5923–5928, 2022.

[86] K.-L. Wong, *Compact Dual-Frequency and Dual-Polarized Microstrip Antennas*, ch. 4, pp. 115–121. New York, USA: John Wiley & Sons Inc., 2002.

[87] T. Huynh and K.-F. Lee, "Single-layer single-patch wideband microstrip antenna," *Electronics letters*, vol. 31, no. 16, pp. 1310–1312, 1995.

[88] R. B. Simorangkir, Y. Yang, L. Matekovits, and K. P. Esselle, "Dual-band dual-mode textile antenna on pdms substrate for body-centric communications," *IEEE Antennas and Wireless Propagation Letters*, vol. 16, pp. 677–680, 2016.

[89] S.-C. Pan and K.-L. Wong, "Dual-frequency triangular microstrip antenna with a shorting pin," *IEEE Transactions on Antennas and Propagation*, vol. 45, no. 12, pp. 1889–1891, 1997.

[90] K.-L. Wong and W.-H. Hsu, "A broad-band rectangular patch antenna with a pair of wide slits," *IEEE Transactions on Antennas and Propagation*, vol. 49, no. 9, pp. 1345–1347, 2001.

[91] E. Abdo-Sanchez, J. E. Page, T. M. Martin-Guerrero, J. Esteban, and C. Camacho-Penalosa, "Planar broadband slot radiating element based on microstrip-slot coupling for series-fed arrays," *IEEE Transactions on Antennas and Propagation*, vol. 60, no. 12, pp. 6037–6042, 2012.

[92] A. A. Kishk, A. W. Glisson, and G. P. Junker, "Bandwidth enhancement for split ground plane microstrip patch antennas," *IEEE Transactions on Antennas and Propagation*, vol. 51, no. 3, pp. 578–585, 2003.

[93] R. De Silva, I. Kitulwatte, D. Priyanath, M. Gunathilake, T. Senanayake, and M. Kumari, "Study on heart measurements of the people between the age 20-40 years present to the teaching hospital colombo north–post mortem study," 2021.

[94] "Niremf - national interuniversity consortium for telecommunications (cnit)." Accessed on October 26, 2023.

[95] N. K. Mallat and A. Iqbal, "Substrate integrated waveguide-based simultaneous transmit and receive antenna for full-duplex wearable devices," *International Journal of RF and Microwave Computer-Aided Engineering*, vol. 32, no. 7, p. e23188, 2022.

[96] D. Nikolayev, W. Joseph, M. Zhadobov, R. Sauleau, and L. Martens, "Optimal radiation of body-implanted capsules," *Physical review letters*, vol. 122, no. 10, p. 108101, 2019.

[97] F. Rules, "Regulations 47 cfr part 95," *Subparts E (95.601-95.673) and I (95.1201-95.1219) Personal Radio Services*, 2002.

[98] D. Nguyen, Y. Choi, W. Jang, and C. Seo, "An ultra-wide bandwidth with compact size implantable antenna for health monitor microsystem," in *2024*

IEEE Wireless Power Technology Conference and Expo (WPTCE), pp. 497–500, IEEE, 2024.

[99] M. Yousaf, I. B. Mabrouk, F. Faisal, M. Zada, Z. Bashir, A. Akram, M. Nedil, and H. Yoo, “Compacted conformal implantable antenna with multitasking capabilities for ingestible capsule endoscope,” *IEEE Access*, vol. 8, pp. 157617–157627, 2020.

[100] A. Lamkaddem, A. El Yousfi, K. A. Abdalmalak, V. G. Posadas, L. E. G. Muñoz, and D. Segovia-Vargas, “A compact design for dual-band implantable antenna applications,” in *2021 15th European Conference on Antennas and Propagation (EuCAP)*, pp. 1–3, IEEE, 2021.

[101] F. Faisal, A. Moulay, M. Chaker, and T. Djerafi, “Efficient wireless power transfer to an ultra-miniaturized antenna for future cardiac leadless pacemaker,” in *2024 18th European Conference on Antennas and Propagation (EuCAP)*, pp. 1–4, IEEE, 2024.

[102] K. Aliqab, I. Nadeem, and S. R. Khan, “A comprehensive review of in-body biomedical antennas: Design, challenges and applications,” *Micromachines*, vol. 14, no. 7, p. 1472, 2023.

[103] IMARC Group, “Implantable medical devices market: Industry trends, share, size, growth, opportunity and forecast 2023-2032,” 2023. Accessed: 2023-11-12.

[104] O. F. Celik, Y. E. Yamac, and S. C. Basaran, “Compact multi-band implantable antenna designs for versatile in-body applications,” *AEU-International Journal of Electronics and Communications*, vol. 150, p. 154204, 2022.

[105] D. Panescu, “Emerging technologies [wireless communication systems for implantable medical devices],” *IEEE Engineering in Medicine and Biology Magazine*, vol. 27, no. 2, pp. 96–101, 2008.

[106] R. S. Hassan, J. Lee, and S. Kim, “A minimally invasive implantable sensor for continuous wireless glucose monitoring based on a passive resonator,” *IEEE Antennas and Wireless Propagation Letters*, vol. 19, no. 1, pp. 124–128, 2019.

[107] B. Lee, M. K. Koripalli, Y. Jia, J. Acosta, M. Sendi, Y. Choi, and M. Ghovanloo, “An implantable peripheral nerve recording and stimulation system for experiments on freely moving animal subjects,” *Scientific reports*, vol. 8, no. 1, pp. 1–12, 2018.

[108] A. Basir, M. Zada, Y. Cho, and H. Yoo, “A dual-circular-polarized endoscopic antenna with wideband characteristics and wireless biotelemetric link characterization,” *IEEE Transactions on Antennas and Propagation*, vol. 68, no. 10, pp. 6953–6963, 2020.

[109] Z. Qiu, A. T. Nguyen, K. Su, Z. Yang, and J. Xu, “A high precision, wide dynamic range closed-loop neuromodulation ic with rapid stimulation artifact recovery,” *IEEE transactions on biomedical circuits and systems*, 2023.

[110] J. Pemberton, L. Collins, L. Drummond, R. P. Dias, R. Krone, M. Kershaw, and S. Uday, “Enhancing equity in access to automated insulin delivery systems in an ethnically and socioeconomically diverse group of children with type 1 diabetes,” *BMJ Open Diabetes Research and Care*, vol. 12, no. 3, p. e004045, 2024.

[111] D. Cui, Y. Liao, J. Du, and Y. Chen, “A meta-analysis of major complications between traditional pacemakers and leadless pacemakers,” *Cardiovascular Innovations and Applications*, vol. 5, no. 3, pp. 145–153, 2021.

[112] N. Bhatia and M. El-Chami, “Leadless pacemakers: a contemporary review,” *Journal of geriatric cardiology: JGC*, vol. 15, no. 4, p. 249, 2018.

[113] R. Ali, Y. Cho, I. A. Shah, S. Hayat, A. Basir, and H. Yoo, “Compact dual-band mimo implantable antenna system for high-data-rate cortical visual prostheses application,” *IEEE Transactions on Antennas and Propagation*, 2024.

[114] A. Iqbal, M. Al-Hasan, I. B. Mabrouk, and T. A. Denidni, “Capsule endoscopic mimo antenna with radiation pattern and polarization diversity,” *IEEE Transactions on Antennas and Propagation*, vol. 71, no. 4, pp. 3146–3154, 2023.

[115] A. J. Alazemi and A. Iqbal, “A high data rate implantable mimo antenna for deep implanted biomedical devices,” *IEEE Transactions on Antennas and Propagation*, vol. 70, no. 2, pp. 998–1007, 2021.

[116] Y. Fan, J. Huang, T. Chang, and X. Liu, “A miniaturized four-element mimo antenna with ebg for implantable medical devices,” *IEEE Journal of Electromagnetics, RF and Microwaves in Medicine and Biology*, vol. 2, no. 4, pp. 226–233, 2018.

[117] P. L. Poshtgol, L. Jichao, S. Soltani, and R. D. Murch, “Mimo antennas for capsule endoscope systems,” in *2016 IEEE International Symposium on Antennas and Propagation (APSURSI)*, pp. 1175–1176, IEEE, 2016.

[118] L. Harlan, V. Kaim, S. Kumar, M. Susila, S. K. Palaniswamy, and B. K. Kanaujia, “Conformal wideband ingestible capsule mimo antenna system for multi-channel communication in biotelemetry,” *AEU-International Journal of Electronics and Communications*, vol. 178, p. 155305, 2024.

[119] D. Jing, H. Li, Q. Huang, X. Ding, and S. Xiao, “Compact and ultra-wideband implantable mimo antenna for deep tissue wireless applications,” *Journal of Electromagnetic Waves and Applications*, pp. 1–16, 2024.

[120] R. Kangeyan and M. Karthikeyan, “A novel wideband fractal-shaped mimo antenna for brain and skin implantable biomedical applications,” *International Journal of Communication Systems*, vol. 36, no. 11, p. e5509, 2023.

[121] J. Ryckaert, C. Desset, A. Fort, M. Badaroglu, V. De Heyn, P. Wambacq, G. Van der Plas, S. Donnay, B. Van Poucke, and B. Gyselinckx, “Ultra-wide-band transmitter for low-power wireless body area networks: Design and evaluation,” *IEEE transactions on circuits and systems I: Regular papers*, vol. 52, no. 12, pp. 2515–2525, 2005.

[122] M. S. Sharawi, *Printed MIMO antenna engineering.* Artech House, 2014.

[123] “Ieee standard for safety levels with respect to human exposure to electric, magnetic, and electromagnetic fields, 0 hz to 300 ghz,” *IEEE Std C95.1-2019 (Revision of IEEE Std C95.1-2005/ Incorporates IEEE Std C95.1-2019/Cor 1-2019)*, pp. 1–312, 2019.

[124] M. S. Sharawi, “Current misuses and future prospects for printed multiple-input, multiple-output antenna systems [wireless corner],” *IEEE Antennas and Propagation Magazine*, vol. 59, no. 2, pp. 162–170, 2017.

[125] A. J. Weinhaus and K. P. Roberts, “Anatomy of the human heart,” *Handbook of cardiac anatomy, physiology, and devices*, pp. 51–79, 2005.

[126] N. Ayrilmis, “Effect of layer thickness on surface properties of 3d printed materials produced from wood flour/pla filament,” *Polymer testing*, vol. 71, pp. 163–166, 2018.

[127] C. B. Dietrich, K. Dietze, J. R. Nealy, and W. L. Stutzman, “Spatial, polarization, and pattern diversity for wireless handheld terminals,” *IEEE transactions on antennas and propagation*, vol. 49, no. 9, pp. 1271–1281, 2001.

[128] A. Kumar, A. Q. Ansari, B. K. Kanaujia, J. Kishor, and L. Matekovits, “A review on different techniques of mutual coupling reduction between elements of any mimo antenna. part 1: Dgss and parasitic structures,” *Radio Science*, vol. 56, no. 3, pp. 1–25, 2021.

[129] J. J. Borchardt and T. C. Lapointe, “U-slot patch antenna principle and design methodology using characteristic mode analysis and coupled mode theory,” *IEEE Access*, vol. 7, pp. 109375–109385, 2019.

[130] Y. Cheng, Y. Dong, and Y. Pan, “Miniaturized circularly polarized metal antenna with a shorting pin for low cost rfid application,” in *2019 IEEE MTT-S International Wireless Symposium (IWS)*, pp. 1–3, IEEE, 2019.

[131] S. Maheshwari, P. Jain, and A. Agarwal, “Cpw-fed wideband antenna with u-shaped ground plane,” *IJ Wireless and Microwave Technologies (IJWMT). ISSN*, pp. 2076–1449, 2014.

[132] S. Das and D. Mitra, “A compact wideband flexible implantable slot antenna design with enhanced gain,” *IEEE Transactions on Antennas and Propagation*, vol. 66, no. 8, pp. 4309–4314, 2018.

[133] S. Jam and H. Malekpoor, “Analysis on wideband patch arrays using unequal arms with equivalent circuit model in x-band,” *IEEE Antennas and Wireless Propagation Letters*, vol. 15, pp. 1861–1864, 2016.

[134] Y. Lu, Y. Huang, H. T. Chattha, and P. Cao, “Reducing ground-plane effects on uwb monopole antennas,” *IEEE Antennas and Wireless propagation letters*, vol. 10, pp. 147–150, 2011.

[135] J. Malik, A. Patnaik, and M. V. Kartikeyan, “A compact dual-band antenna with omnidirectional radiation pattern,” *IEEE Antennas and Wireless Propagation Letters*, vol. 14, pp. 503–506, 2014.

[136] . IEEE Standards Coordinating Committee *et al.*, “Ieee standard for safety levels with respect to human exposure to radio frequency electromagnetic fields, 3khz to 300ghz,” *IEEE C95. 1-1991*, 1992.

[137] J. B. Andersen and A. Frandsen, “Absorption efficiency of receiving antennas,” *IEEE Transactions on Antennas and Propagation*, vol. 53, no. 9, pp. 2843–289, 2005.

[138] Z. Li, Z. Du, M. Takahashi, K. Saito, and K. Ito, “Reducing mutual coupling of mimo antennas with parasitic elements for mobile terminals,” *IEEE Transactions on Antennas and Propagation*, vol. 60, no. 2, pp. 473–481, 2011.

[139] D. Tse and P. Viswanath, *Fundamentals of wireless communication.* Cambridge university press, 2005.

[140] I. Foundation, “Tissue properties database.” Online.

APPENDIX A

Properties of Human Body Tissues Across Frequency Bands

This Appendix outlines the dielectric properties of human body tissues in various frequency bands relevant to this research. These properties are essential for understanding electromagnetic interactions with the human heart. The tables provided summarize the frequencies utilized in different designs developed during the PhD period.

The data shown below [140] illustrate how the permittivity and conductivity of tissues vary with frequency. As frequency increases, permittivity decreases, and conductivity increases. These trends are important for optimizing antenna designs and ensuring that they align with biological conditions.

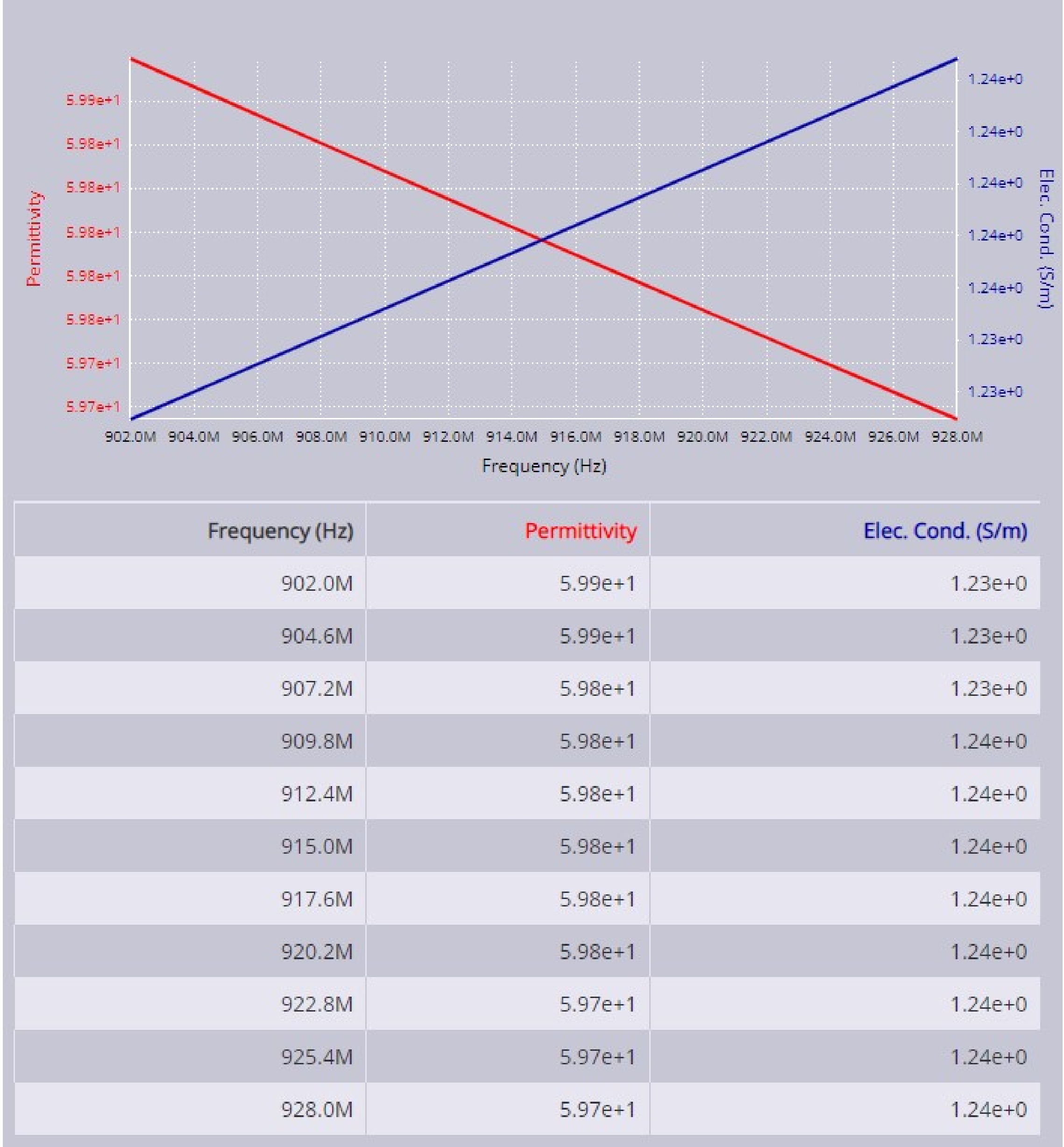

Frequency (Hz)	Permittivity	Elec. Cond. (S/m)
902.0M	5.99e+1	1.23e+0
904.6M	5.99e+1	1.23e+0
907.2M	5.98e+1	1.23e+0
909.8M	5.98e+1	1.24e+0
912.4M	5.98e+1	1.24e+0
915.0M	5.98e+1	1.24e+0
917.6M	5.98e+1	1.24e+0
920.2M	5.98e+1	1.24e+0
922.8M	5.97e+1	1.24e+0
925.4M	5.97e+1	1.24e+0
928.0M	5.97e+1	1.24e+0

Figure A.1: Dielectric properties in the 902-928 MHz ISM Band.

Frequency (Hz)	Permittivity	Elec. Cond. (S/m)
1.395G	5.76e+1	1.51e+0
1.399G	5.75e+1	1.51e+0
1.402G	5.75e+1	1.51e+0
1.406G	5.75e+1	1.52e+0
1.410G	5.75e+1	1.52e+0
1.414G	5.75e+1	1.52e+0
1.417G	5.75e+1	1.52e+0
1.421G	5.75e+1	1.53e+0
1.425G	5.75e+1	1.53e+0
1.428G	5.74e+1	1.53e+0
1.432G	5.74e+1	1.53e+0

Figure A.2: Dielectric properties in the 1.395-1.432 GHz WMTS Band.

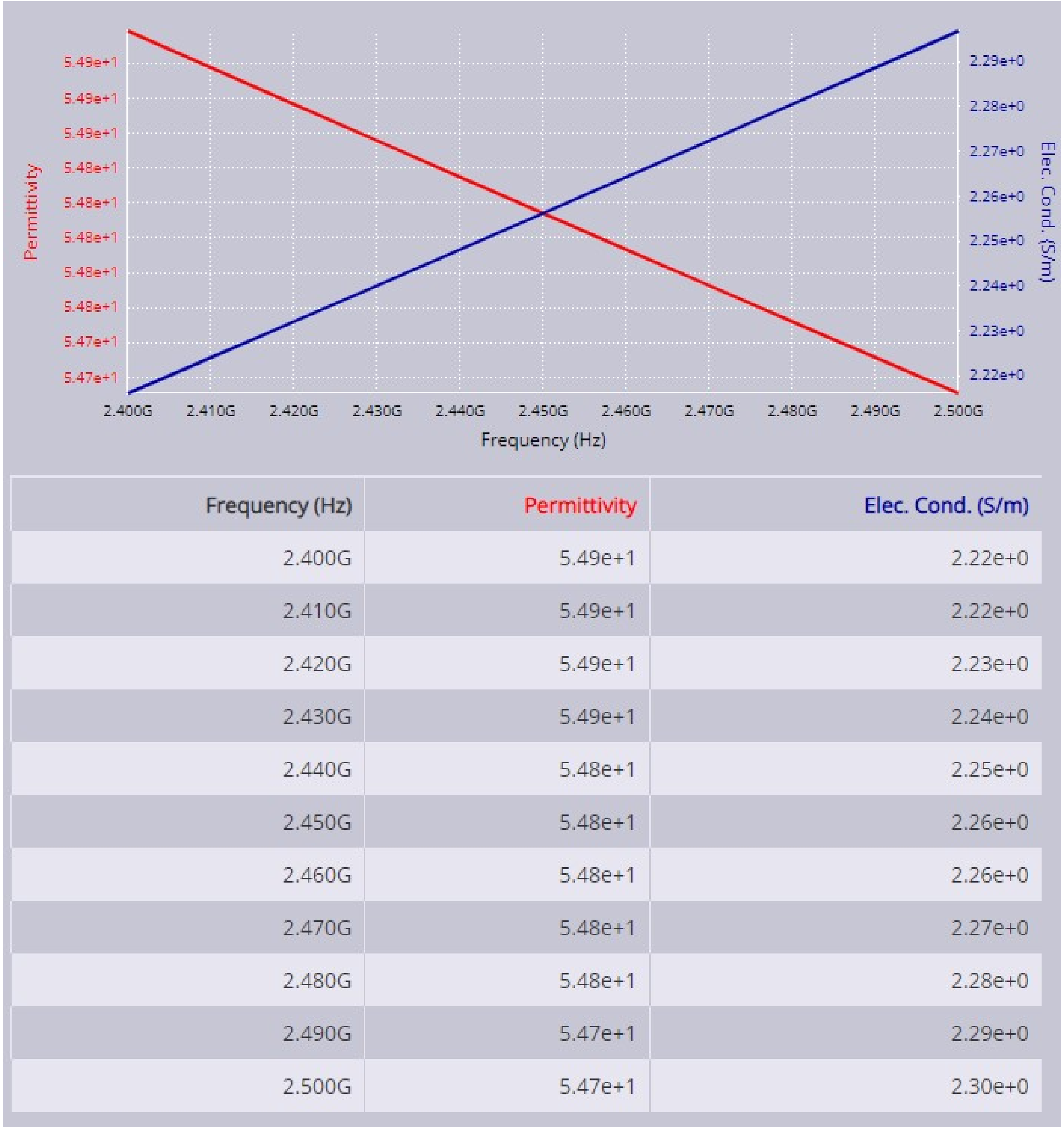

Frequency (Hz)	Permittivity	Elec. Cond. (S/m)
2.400G	5.49e+1	2.22e+0
2.410G	5.49e+1	2.22e+0
2.420G	5.49e+1	2.23e+0
2.430G	5.49e+1	2.24e+0
2.440G	5.48e+1	2.25e+0
2.450G	5.48e+1	2.26e+0
2.460G	5.48e+1	2.26e+0
2.470G	5.48e+1	2.27e+0
2.480G	5.48e+1	2.28e+0
2.490G	5.47e+1	2.29e+0
2.500G	5.47e+1	2.30e+0

Figure A.3: Dielectric properties in the 2.4-2.5 GHz ISM Band.

Frequency (Hz)	Permittivity	Elec. Cond. (S/m)
5.725G	4.91e+1	5.77e+0
5.740G	4.90e+1	5.79e+0
5.755G	4.90e+1	5.80e+0
5.770G	4.90e+1	5.82e+0
5.785G	4.90e+1	5.84e+0
5.800G	4.89e+1	5.86e+0
5.815G	4.89e+1	5.88e+0
5.830G	4.89e+1	5.90e+0
5.845G	4.89e+1	5.92e+0
5.860G	4.89e+1	5.94e+0
5.875G	4.88e+1	5.96e+0

Figure A.4: Dielectric properties in the 5.725-5.875 GHz ISM Band.